



BERGISCHE
UNIVERSITÄT
WUPPERTAL

Mass Spectrometric Investigation of Metal Hydrides relevant to Extreme Ultraviolet Lithography

Dissertation

zur Erlangung des akademischen Grades
Doktor der Naturwissenschaften (Dr. rer. nat.)

Vorgelegt von
Joshua A. D. Rieger
geboren in Bergisch Gladbach, Deutschland

Bergische Universität Wuppertal
Fakultät 4 - Mathematik und Naturwissenschaften
Physikalische und Theoretische Chemie
unter der Anleitung von
Prof. Dr. Thorsten Benter

Wuppertal, November 2023

"The only difference between screwing around and science is writing it down."

Adam Savage

Danksagung

Ich bin zutiefst dankbar für die freundliche, entspannte und inspirierende Arbeitsumgebung, die Thorsten und Hendrik geschaffen haben. Ihre Unterstützung und die Zusammenarbeit auf Augenhöhe haben nicht nur meine Forschung, sondern auch meine persönliche Entwicklung maßgeblich geprägt.

Ein besonderer Dank gilt meinen Freunden und Kollegen Clara, Markus und Robin, die die Zeit des Studiums und der Promotion zu einer unvergesslichen Erfahrung gemacht haben, ebenso der TOF-Express zu den Messkampagnen. Eure Freundschaft hat nicht nur den wissenschaftlichen Alltag bereichert.

Meiner Familie möchte ich für ihren immerwährenden Zuspruch und ihre ermutigenden Worte danken. Ohne ihre Unterstützung wäre dieser Weg sicherlich steiniger gewesen. Meiner Partnerin Josefine danke ich sehr für die Liebe und Unterstützung, die mir in den anspruchsvollen Phasen der Promotion starken Halt gaben und für ihr Interesse meine Forschung zu verstehen.

Abschließend danke ich allen, die einen Beitrag zu dieser Dissertation in vielfältiger Weise geleistet und mich auf meinem Weg unterstützt haben, bevor nun langsam der Ernst des Lebens beginnt.

Abstract

Extreme ultraviolet (EUV) lithography is one of the key technologies for the industrial production of highly integrated semiconductor devices. A core problem is the accumulation of tin in the EUV source during the wafer exposure process, which degrades and damage EUV optical components. To alleviate this situation, a deep understanding of the homogeneous and heterogeneous processes involved in the formation and deposition processes is required. One of the fundamental questions is how and in what chemical state elements (especially metals) can become volatile in the presents of a hydrogen plasma and thereby exhibit the potential for contamination. One of the main tasks of this work is the measurement of the relevant hydrides at the ultra-trace level. This includes modification, optimization, and characterization of mass spectrometric instrumentation to achieve sufficient sensitivity. With well-defined conditions and reactants, the system under study is reduced to the laboratory scale for ease of operation and to allow for ample modifications. The central focus of this research is the interaction of RF hydrogen plasma species with the target elements and the determination of native ions and molecules using mass spectrometry as the primary analytical tool. Experiments are designed to elucidate the mechanisms involved and to understand the processes occurring.

Different hydrogen plasma sources are used in the experiments. Due to their different designs and nature, they are suitable for the coupling to different mass spectrometers. With the use of multiple plasma sources, the influence of the plasma source and its parameters can be determined. In order to gain deeper insight into the processes in and around the plasma, several mass spectrometers are used, each with a different (partly customized) ion source and detection capability. Depending on the instrument and its ion source, neutral molecules can be detected by EI ionization or native ions generated in the hydrogen plasma can be measured directly by guiding them into the analyzer. In this way, both the neutral and ionic products of the reactions can be determined. Reverse Analysis of Superimposed signal Patterns (RASP), a program developed within this work, allows for the reverse calculation of isotope-related superimpositions of metal (hydride) signals. In this way, the distribution of the different metal hydride ions is accessible, providing important information about the formation process of the corresponding species.

Since a high-resolution mass spectrum of stannane, a key component in EUV lithography, is crucial for the in-depth mass spectrometric analysis of tin hydride and its ions, it is synthesized and measured under well-known conditions. To the best of our knowledge, this high-resolution mass spectrum of stannane is the only one published with specification of ionization conditions. These mass spectra serve as a reference standard for the measurement of plasma generated metal hydride species.

To directly monitor and quantify the etching process of deposited tin by hydrogen plasma species, tin-coated sensors for quartz crystal microbalance (QCM) instruments are placed near the hydrogen plasma. The change in mass on the sensor due to etching is directly related to the rate of etching under the prevailing conditions. Simultaneous QCM and mass spectrometry measurements provide a way to relate the mass change to the experimentally obtained mass spectra. The experiments described in this thesis aim to investigate the heterogeneous formation mechanism of metal hydrides and related species and to gain a fundamental understanding of the various chemical and physical processes occurring in the plasma, at plasma-proximal surfaces and in the gas phase in order to benefit from this information for understanding the chemistry and dynamics occurring in EUV lithography.

Contents

| | |
|--|------------|
| Acronyms | ix |
| List of Figures | xii |
| List of Tables | xv |
| 1 Scope of this work | 1 |
| 2 Introduction | 3 |
| 2.1 Photolithography | 3 |
| 2.2 EUV lithography | 5 |
| 2.3 Plasma | 8 |
| 2.3.1 Plasma fundamentals | 8 |
| 2.3.2 Plasma generation | 12 |
| 2.4 Debris | 14 |
| 2.4.1 Tin debris | 14 |
| 2.4.1.1 Decomposition of stannane | 15 |
| 2.4.1.2 Hydrogen etching of tin | 18 |
| 2.4.2 Debris of other elements | 20 |
| 2.4.3 Surface oxidation processes | 22 |
| 2.5 Mass spectrometry | 23 |
| 2.6 Components and structure of mass spectrometers | 24 |
| 2.6.1 Creating ions | 25 |
| 2.6.1.1 Electron ionization | 25 |
| 2.6.1.2 Chemical ionization | 27 |
| 2.6.2 Mass analyzers | 29 |
| 2.6.2.1 Sector field mass spectrometer | 29 |
| 2.6.2.2 Time-of-flight mass spectrometer | 32 |
| 2.7 Quartz crystal microbalance | 34 |

| | | |
|----------|--|-----------|
| 3 | Methods & Instrumentation | 36 |
| 3.1 | Chemicals | 36 |
| 3.2 | Plasma sources | 36 |
| 3.2.1 | Plasma chamber | 36 |
| 3.2.2 | Helical coil resonator | 37 |
| 3.3 | Mass spectrometers | 38 |
| 3.3.1 | Sector field mass spectrometer - MAT95XP | 39 |
| 3.3.2 | Time-of-flight mass spectrometer | 40 |
| 3.3.2.1 | LTOF | 40 |
| 3.3.2.2 | CTOF | 45 |
| 3.4 | Quartz crystal microbalance | 46 |
| 3.4.1 | Electrode coating | 46 |
| 3.5 | Fourier-transform infrared spectrometer | 49 |
| 3.6 | Laser systems | 49 |
| 3.7 | Syntheses | 50 |
| 3.7.1 | Stannane synthesis | 50 |
| 3.7.2 | Tin oxide synthesis | 52 |
| 3.8 | Software | 52 |
| 3.8.1 | RASP | 52 |
| 3.8.2 | DFT calculations | 56 |
| 4 | Results & Discussion | 57 |
| 4.1 | Synthesized stannane | 57 |
| 4.1.1 | Infrared spectrum of stannane | 57 |
| 4.1.2 | Mass spectrum of stannane | 59 |
| 4.1.2.1 | Doubly charged stannane and the stannane dimer | 64 |
| 4.1.2.2 | Influences on stannane mass spectra | 66 |
| 4.2 | Plasma-generated stannane | 68 |
| 4.2.1 | Neutral tin hydrides | 68 |
| 4.2.1.1 | Doubly charged stannane and the stannane dimer | 70 |
| 4.2.1.2 | Oxygenated stannane | 71 |
| 4.2.1.3 | Comparison of the different experimental set-ups | 72 |
| 4.2.2 | Ionic tin hydrides | 73 |
| 4.2.2.1 | Doubly charged stannane and the stannane dimer | 75 |
| 4.2.2.2 | Oxygenated stannane | 77 |
| 4.2.2.3 | Experimental settings affecting mass spectra | 78 |

| | | |
|----------|--|------------|
| 4.2.2.4 | Comparison of the different experimental set-ups | 83 |
| 4.2.3 | Tin deuterides | 84 |
| 4.3 | Transport behavior of neutral and ionic tin hydride molecules in glass tubes | 86 |
| 4.4 | Decomposition process of stannane on glass | 89 |
| 4.5 | Other plasma-generated metal hydrides | 92 |
| 4.5.1 | Lead (Pb) | 93 |
| 4.5.2 | Magnesium (Mg) | 96 |
| 4.5.3 | Copper (Cu) | 97 |
| 4.6 | DFT calculations | 100 |
| 4.6.1 | Cationic tin species | 101 |
| 4.6.2 | Neutral tin hydrides | 103 |
| 4.6.3 | Anionic tin hydrides | 104 |
| 4.6.4 | Conclusion of the simulation results | 105 |
| 4.7 | Initial etching phenomenon | 105 |
| 4.7.1 | Description of the phenomenon | 105 |
| 4.7.2 | Oxygen exposition | 108 |
| 4.7.3 | Addition of oxygen | 112 |
| 4.7.4 | Tin oxide as target | 115 |
| 4.8 | Quartz crystal microbalance measurements | 117 |
| 4.8.1 | Sensor characterization | 117 |
| 4.8.1.1 | Hydrogen etching of electroplated tin | 119 |
| 4.8.1.2 | Etching vs. sputtering | 121 |
| 4.8.1.3 | Influence of potentials on electrodes | 123 |
| 4.8.2 | Additional methods of sensor coating | 124 |
| 4.8.2.1 | Sensor coating via thermal evaporation | 124 |
| 4.8.2.2 | Sensor coating via stannane decomposition | 126 |
| 4.9 | Simultaneous measurement of QCM and LTOF | 127 |
| 4.9.1 | Comparison with literature data | 131 |
| 5 | Conclusion & Outlook | 133 |
| | References | 136 |

Acronyms

| | | | |
|--------------------|--------------------------------------|----------------------|---------------------------------|
| ϵ_0 | vacuum permittivity | DFT | density functional theory |
| κ | electron-neutral collision frequency | DOF | depth-of-focus |
| | | E | electric field strength |
| λ | wave length | E_k | kinetic energy |
| λ_D | Debye-length | EI | electron ionization |
| v | velocity | EIC | extracted ion current |
| ω | plasma frequency | ESA | electrostatic analyzer |
| χ | degree of ionization | EUV | extreme ultraviolet |
| AC | alternating current | EUVL | extreme ultraviolet lithography |
| B | magnetic field induction | eV | electron volt |
| B3LYP | Becke 3-parameter Lee-Yang-Parr | F_c | centrifugal force |
| | | F_e | electrical force |
| CD | critical dimension | F_L | Lorentz force |
| $^{\circ}\text{C}$ | degree Celsius | FT | Fourier-transform |
| CI | chemical ionization | GFRP | glass-fiber reinforced plastic |
| CMB | cosmic microwave background | h | Planck constant |
| cps | counts per second | HC | hydrocarbon |
| CUS | coordinative unsaturated sites | HCR | helical coil resonator |
| DC | direct current | IC | integrated circuit |
| | | IEE | ion-enhanced etching |

| | | | |
|-------------------------|---|--------------|---------------------------------------|
| IP | ionization potential | RF | radio frequency |
| IR | infrared | RIE | reactive ion etching |
| K | kelvin | RRKM | Rice-Ramsberger-Kassel-Marcus |
| k_b | Boltzmann constant | s | second |
| laser | light amplification by stimulated emission of radiation | SCF | self consistent field |
| LTE | local thermal equilibrium | SF | sector field mass spectrometer |
| m | mass | SPI | single-photon ionization |
| MFC | mass flow controller | STP | standard temperature and pressure |
| min | minute | T | temperature |
| MLM | multilayer mirror | TIC | total ion current |
| MPI | multi-photon ionization | TOF | time-of-flight |
| m/z | mass-to-charge | U | electric field potential |
| NA | numerical aperture | u | unified atomic mass unit |
| non-LTE | non-local thermal equilibrium | UV | ultraviolet |
| OPO | optical parametric oscillator | V | volts |
| p | pressure | VSEPR | valence shell electron pair repulsion |
| PC | plasma chamber | VUV | vacuum ultraviolet |
| PVD | physical vapor deposition | XPS | X-ray photoelectron spectroscopy |
| QCM | quartz crystal microbalance | z | charge |
| R | reflectivity | | |
| RASP | reverse analysis of superimposed signal patterns | | |

List of Figures

| | | |
|------|---|----|
| 2.1 | Schematic illustration of the steps in the photolithography process. | 4 |
| 2.2 | Schematic illustration of EUV plasma generation from tin droplets. | 6 |
| 2.3 | Schematic representation of an multilayer mirror. | 7 |
| 2.4 | DFT calculated structure of SnH ₄ | 15 |
| 2.5 | Fundamental structure of mass spectrometer | 25 |
| 2.6 | Schematic illustration of the directional focus of a 180° magnetic sector. . . | 31 |
| 2.7 | Schematic representation of a linear time-of-flight (TOF) mass spectrometer. | 34 |
| | | |
| 3.1 | Schematic diagram of the plasma chamber and peripherals. | 38 |
| 3.2 | Schematic illustration of the HCR system. | 39 |
| 3.3 | CAD drawing of the custom inlet system of the MAT95 XP mass spectrometer. | 40 |
| 3.4 | CAD exploded assembly drawing of the custom EI source of the LTOF. . . | 41 |
| 3.5 | Simion ion trajectory simulations of the custom LTOF ion source. | 42 |
| 3.6 | CAD drawing of the hexapole ion guide transfer. | 44 |
| 3.7 | Schematic of a quartz crystal microbalance sensor. | 46 |
| 3.8 | Images of electroplated sensor surfaces using an optical microscope. | 48 |
| 3.9 | Images of PVD-coated sensor surfaces using an optical microscope. | 48 |
| 3.10 | Schematic of the stannane synthesis apparatus. | 51 |
| 3.11 | Core elements of RASP | 53 |
| 3.12 | Calculated mass spectrum of SnH ₃ via molmass. | 54 |
| 3.13 | Progression of the minimize optimization with the Nelder-Mead algorithm approach. | 55 |
| | | |
| 4.1 | Gas-phase infrared spectrum of synthesized stannane. | 58 |
| 4.2 | Mass spectrum of stannane (SnH ₄); LTOF MS; EI at 70 eV | 59 |
| 4.3 | Individual signals of the stannane mass spectrum; LTOF MS; EI at 70 eV. . | 62 |
| 4.4 | Mass spectrum of double charged stannane (SnH _x ²⁺); LTOF MS; EI at 70 eV. | 64 |
| 4.5 | Mass spectrum of the stannane dimer (Sn ₂ H _x ⁺); LTOF MS; EI at 70 eV. . . | 65 |
| 4.6 | Effect of hydrogen gas pressure on stannane fragment distribution. | 66 |

| | | |
|------|---|----|
| 4.7 | Effect of ion source temperature on stannane fragment distribution. | 68 |
| 4.8 | Mass spectrum of plasma generated stannane (SnH_X^+); LTOF MS; EI at 70 eV. | 70 |
| 4.9 | Mass spectrum of plasma generated double charged stannane (SnH_X^{2+}); LTOF MS; EI at 70 eV | 71 |
| 4.10 | Mass spectrum of plasma generated oxygenated stannane (SnOH_X^+); LTOF MS; EI at 70 eV. | 72 |
| 4.11 | Comparison of fragment distributions recorded with different mass spectrometers and plasma sources. | 73 |
| 4.12 | Mass spectrum of plasma generated stannane (SnH_X^+); LTOF MS; native ions. | 75 |
| 4.13 | Mass spectrum of plasma generated stannane dimer (Sn_2H_X^+); LTOF MS; native ions. | 76 |
| 4.14 | Mass spectrum of plasma generated double charged stannane (SnH_X^{2+}); LTOF MS; native ions. | 76 |
| 4.15 | Mass spectrum of plasma generated oxygenated stannane (SnOH_X^+); LTOF MS; native ions. | 77 |
| 4.16 | Dependence of the signal intensity of tin species on the plasma power. | 79 |
| 4.17 | Effect of hydrogen plasma pressure on stannane fragment distribution and the signal intensity; LTOF MS, native ions. | 80 |
| 4.18 | Effect of the lens potential of the hexapole ion guide on stannane fragment distribution and the signal intensity. | 81 |
| 4.19 | Effect of the ramp gradient of the hexapole ion guide on stannane fragment distribution and the signal intensity. | 82 |
| 4.20 | Comparison of fragment distributions at different mass spectrometers and plasma sources. | 84 |
| 4.21 | Calculated distribution of the deuterium plasma generated stannane hydrides. | 85 |
| 4.22 | Influence of the distance between tin target and analyzer at constant plasma-target distance; CTOF MS. | 87 |
| 4.23 | Influence of the distance between HCR coil and tin target at constant target-analyzer distance; CTOF MS. | 89 |
| 4.24 | Intensity variation over time of the gas phase infrared spectrum of synthesized stannane. | 90 |
| 4.25 | Intensity variation over time of the 1905 cm^{-1} signal from synthesized stannane in the FTIR spectrum and fitting of the data. | 91 |

| | | |
|------|---|-----|
| 4.26 | Mass spectrum of plasma generated plumbane (PbH_X^+); CTOF MS; native ions. | 94 |
| 4.27 | Mass spectrum of plasma generated oxygenated plumbane (PbOH_X^+); CTOF MS; native ions. | 95 |
| 4.28 | Mass spectrum (processed) of plasma generated magnesium hydride (MgH_X^+); SF MS; EI at 70 eV. | 98 |
| 4.29 | Mass spectrum of copper ions by laser ablation (Cu^+); LTOF MS; native ions. | 99 |
| 4.30 | Optimized structures of the DFT calculated tin species. | 106 |
| 4.31 | Ionogram of plasma-generated stannane. | 107 |
| 4.32 | Ionogram of stannane and oxygenated stannane and their ratio. | 109 |
| 4.33 | Ionogram of different plasma species and the ratio of stannane and these. . | 111 |
| 4.34 | Ionogram of stannane and oxygenated stannane and their ratio. | 113 |
| 4.35 | Ionogram of H_3O^+ , N_2H^+ and CO_2H^+ | 114 |
| 4.36 | Detected native ions of SnO_2 in H_2 plasma; LTOF; native ions. | 116 |
| 4.37 | Clean QCM sensor in H_2 plasma at different plasma power. | 118 |
| 4.38 | Comparison of etching of two identical electroplated QCM sensors. | 120 |
| 4.39 | Comparison of different plasmas (H_2 , Ar, He) with identical electroplated QCM sensors. | 122 |
| 4.40 | Comparison of two identical electroplated QCM sensors with different applied potentials. | 123 |
| 4.41 | Tin coated QCM sensor via thermal evaporation in H_2 plasma. | 125 |
| 4.42 | Stannane coating of a clean QCM sensor | 127 |
| 4.43 | Simultaneous measurement of the QCM and the LTOF. | 129 |

List of Tables

| | | |
|------|---|-----|
| 2.1 | Properties and parameters of stannane | 16 |
| 3.1 | Exemplary voltages of the custom ion source in the EI mode. | 43 |
| 3.2 | Specifications of the QCM. | 47 |
| 4.1 | Mass spectrum of stannane (SnH_4); LTOF MS; EI at 70 eV. | 60 |
| 4.2 | Comparison of the determined fractions of Sn^+ and SnH_3^+ | 61 |
| 4.3 | Comparison of the determined proportions from the LTOF with the literature. | 63 |
| 4.4 | Plasma chamber parameter for measurement of neutrals. | 69 |
| 4.5 | Gas flows and pressures within the plasma chamber/ LTOF system and electrical potentials of the hexapole ion guide for ion measurement. | 74 |
| 4.6 | Distribution of plumbane fragments from Saalfeld and Svec and possible species from CTOF measurement. | 96 |
| 4.7 | Results of the calculation of the cationic tin species. | 102 |
| 4.8 | Results of the calculation of the neutral tin species. | 103 |
| 4.9 | Results of the calculation of the anionic tin species | 104 |
| 4.10 | Calculated slopes and errors of the slopes of selected EICs from stannane. | 108 |
| 4.11 | Rates of mass gain due to the hydrogen plasma at different plasma powers. | 119 |
| 4.12 | Measured change in the mass of the QCM sensors (S-1 and S-2) and derived values. | 120 |
| 4.13 | Comparison of LTOF and QCM measurement results. Hydrogen plasma (1.2×10^{-1} mbar). | 130 |

1 Scope of this work

Microchips, also known as integrated circuits (ICs), are the foundation of modern electronic devices and systems. The origins of microchips date back to the 1950s and 60s, when research on semiconductor materials such as silicon (Si) and germanium (Ge) began. The breakthrough was the development of the transistor, an electronic component that made it possible to amplify and switch electrical signals. With the invention of the transistor, it was possible to realize electronic circuits on a significantly smaller scale than was possible with conventional tubes. This pioneered the development of microchips that integrate tens of thousands or even millions of transistors on a single silicon chip. In 1965, Gordon Moore, one of the founders of Intel, predicted the doubling of the number of transistors present on an integrated circuit every 18 to 24 months. This means that the performance of computer chips can typically increase significantly every 1-2 years[1]. Since its formulation, Moore's Law has been enormously important to the computer and semiconductor industries, pushing them to continually improve chip performance. It is also impacting on the broader tech-industry, driving new technologies and applications that benefit from continuing improvements in microchip performance. Since their invention, microchips continue to have a revolutionary effect on the world and the manner in which humans live, work and communicate. They have enabled the development of computers, smartphones, tablets, wearables, cars and many other electronic devices and systems. The importance of microchips, however, goes beyond the consumer and home electronics industries. They are used in medical technology, the automotive industry, aerospace, renewable energy and many other industries. As microchips continue to miniaturize and improve their performance, they will continue to play an important role in solving challenges in many areas[2]. The demand for ever more powerful and smaller chips necessitated the use of ever shorter wavelengths for the pivotal photolithography processes to fulfil the requirements. The use of extreme ultraviolet (EUV) radiation (10 nm to 121 nm; 124 eV to 10.25 eV) is one of the key technologies for the current development of semiconductor devices. The large energy of these photons and the associated chemistry they can drive, as well as the formation of tin debris by the EUV tin plasma during the exposure process, are key problems that detrimentally affect the performance of EUV and particularly of the EUV source components.

1 Scope of this work

The general scope of the present work is the measurement and determination of stannane (SnH_4) and other relevant (metal) hydrides in the gas phase at ultra-trace level. This includes the modification, optimization and characterization of mass spectrometric instruments and corresponding interfaces and transfer stages to achieve sufficient sensitivity, as well as the emulation of the chemical and physical processes leading to the formation of debris on a laboratory scale with clearly defined reaction partners and conditions. Inevitably, the question arises how and in what form the relevant elements (especially metals) become volatile by interacting with excited hydrogen species, which may be a potential source of wide-spread contamination. Synthesis and measurement of authentic stannane is required for establishing a solid mass spectrometric data basis. This will provide reliable high-resolution spectra for direct comparisons with plasma-generated species. The etching process of the elements by reactive hydrogen is of particular importance. This is mainly responsible for the detachment/volatilization process and the subsequent contamination of surfaces by decomposition. In addition to mass spectrometry, the etching and decompositions process will be studied with other analytical systems (quartz crystal microbalance (QCM) and Fourier-transform (FT)-infrared (IR) spectroscopy) that provide additional and independent information about the investigated processes. This requires a deep understanding of the homogeneous and heterogeneous chemical and physical reactions that take place, as well as the fundamental investigation of gas phase processes in mass spectrometers and the analysis of the results.

2 Introduction

2.1 Photolithography

Photolithography (or optical lithography) is one of the essential steps in semiconductor technology for the manufacture of ICs. Photolithography uses light to transfer a highly complex structure from a mask onto a silicon wafer (a thin slice of single crystalline silicon). Figure 2.1 schematically illustrates the individual steps. A conductive layer and then a functional photoresist are applied to the wafer using spin-coating. Photoresists are chemicals that become soft (positive photoresist) or hard (negative photoresist) when exposed to light. The mask contains the structure of the IC as a blueprint, and this information is projected from the mask onto the photoresist. Depending on the process and the type of photoresist, the exposed or unexposed photoresist can be etched away to transfer the pattern from the mask to the wafer. The functional layer thus exposed, which is not covered by the photoresist, is then etched away. Thus, the conductive functional layer forms the desired shape. Remaining photoresist is removed and many steps are repeated until IC is complete. These sequential processes are called multi-patterning[3].

The demand for the production of ever smaller and more compact ICs will at some point reach its physical limits. One limit is the resolution, which is represented by the critical dimension (CD). CD refers to the smallest imageable line width, which significantly influences the resolving power, i.e. the ability of the optical system to image the smallest structure in the photoresist. The CD is determined by the Rayleigh equation:

$$CD = k_1 \frac{\lambda}{NA} \quad (2.1)$$

where λ is the wavelength of the light, NA is the numerical aperture and k_1 is a resolution factor depending on the optical system. The numerical aperture is defined as follows, where n is the index of refraction and Θ is the half angle between the light beam and the wafer surface.

$$NA = n \sin\Theta \quad (2.2)$$

2 Introduction

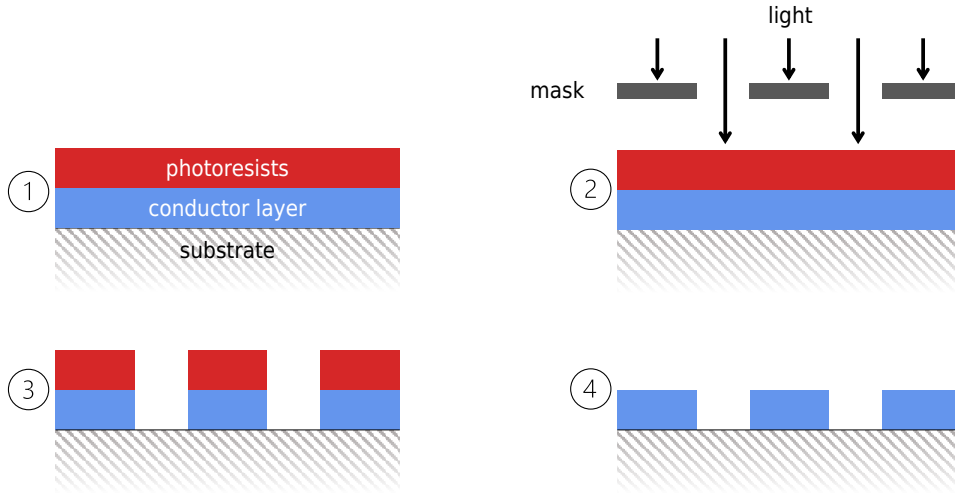


Figure 2.1: Schematic illustration of the steps in the photolithography process: ① Substrate with a conductor layer and a positive photoresist. ② The mask transfers the pattern information to the photoresist via light. The positive photoresist is cured by light. ③ The unexposed photoresist is etched away along with the underlying conductive layer. ④ The desired structure is in the conductive layer after cleaning.

The CD is only a description of the resolution capacity in 2 dimensions, but ICs are 3-dimensional structures with a non-negligible depth. This means that the photons have to penetrate a defined depth of the photoresist and remain in focus for the entire depth. The maximum depth where focus is maintained is depth-of-focus (DOF). In simple terms, DOF is a measure of how much a process can tolerate focus errors and still produce acceptable lithography results. The definition of DOF is below, where k_2 is also a process constant.

$$\text{DOF} = k_2 \frac{\lambda}{\text{NA}^2} \quad (2.3)$$

Considering eqs. (2.1) and (2.3), the resolution can be improved by reducing the wavelength for illumination. The size of the structures that can be achieved is mainly limited by the wavelength of the radiation used. This was already described by Ernst K. Abbe for light microscopes in 1873[4]. The first scanner systems used the g-line of mercury (Hg) arc lamps at 436 nm which provided a resolution of roughly 400 nm. Nowadays the common scanners use the light of an argon-fluoride (ArF) excimer laser radiating at 193 nm. The light in these regions is referred to as deep or far ultraviolet and leads to a resolution of

45 nm. And this is where the further resolution improvement stalled. Experiments with 157 nm (F_2) and 121 nm (H_2) lasers revealed technical problems with the required lenses consisting of calcium-fluoride (CaF) and lithium-fluoride (LiF). Consequently, the common scanner still operates at 193 nm. However, techniques like multi-patterning improve the resolution to fulfil the ever increasing requirements. In this method, the exposure process is divided into several steps, each with its own mask. Thus, several cycles of lithography and etching/deposition are performed in succession. Here, the nomenclature indicates the process: Litho-Etch-Litho-Etch (LELE) contains two cycles, LELELE contains three cycles and so on. This procedure allows to generate smaller and more complex structures on the wafer, but adds complexity and time to the exposure process.

2.2 EUV lithography

Next generation lithography, or extreme ultraviolet lithography (EUVL), is the next major milestone in semiconductor development. These scanners operate with EUV radiation at 13.5 nm. Reducing the wavelength by more than an order of magnitude has great advantages regarding eqs. (2.1) and (2.3), since the short wavelength increases the resolving power and the DOF to a great extent. But there is also a huge increase in photon energy at EUV wavelengths: At 13.5 nm the photon energy is 92 eV. This wavelength cannot be produced by conventional excitation of atoms or molecules (black body radiation), they must be produced by a plasma. To a good approximation, the idealized notion of black-body radiation applies to the emission of hot plasmas. At a target wavelength of 13.5 nm, the plasma has a temperature of roughly 220 000 K.

Besides xenon, tin is the only element that emits enough light as a plasma at this wavelength. The most common tin plasma source consists of a droplet generator that creates tin droplets with a diameter of about 30 μm at high frequency (50 000 s^{-1}). Several cameras track exactly the position, trajectory and velocity of every drop and a first laser pulse (pre-laser) with lower pulse energy hits the droplet and expands it into a disc shape. The following main pulse with high pulse energy converts the disc to the plasma state (cf. fig. 2.2). The resulting dense, hot laser-generated pulsed plasma (LPP) consists of tin in the average charge state +10 [5]. During the relaxation of the highly excited tin atoms, a sharp radiation band around 13.5 nm emerges. The atomic transitions responsible for this emission are grouped together as so-called unresolved-transition arrays (UTAs), as a result of the large number of possible transitions close to each other. These originate from the complex electronic structure of the open 4d-subshell[6]. In addition to tin (Sn) as a plasma

2 Introduction

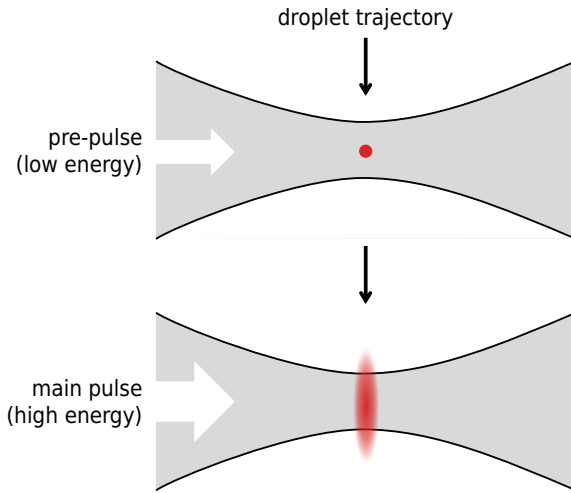


Figure 2.2: Schematic illustration of EUV plasma generation from tin droplets. The pre-pulse inflates the droplet in the disc shape and the subsequent main pulse ionizes it.

material, other elements like xenon (Xe) were also considered, but they had insufficient conversion efficiencies of primary laser energy into EUV radiation[7]. Tin, on the one hand, has excellent plasma qualities with a conversion efficiency of 5.5% to 6.0%, but on the other hand, it is a reason for a problem of the EUVL: contamination of optics with tin debris and the formation of volatile stannane (SnH_4) with excited hydrogen.

Lenses typical for lithography cannot be used because there is no material transparent to EUV light. Therefore, all optical elements are reflective. They are made of multilayer mirrors MLM or Bragg-mirrors[8], which provide a sufficiently large reflection potential for EUV light. Figure 2.3 shows the structure of such a mirror. An MLM has alternating dielectric thin films with low and high refracting index. In 1972, Eberhard Spiller presented a multilayer design that exhibited high reflectance performance in the EUV spectral region[9]. For 13.5 nm, molybdenum (Mo) and silicon (Si) is used as layer stacking material. For this purpose, Mo-Si-bilayers are deposited on a very smooth low thermal expansion material (LTEM). A capping layer of ruthenium (Ru) with a thickness of a few nanometers serves to protect the mirrors. MLMs operate on the principle of Bragg reflection. The

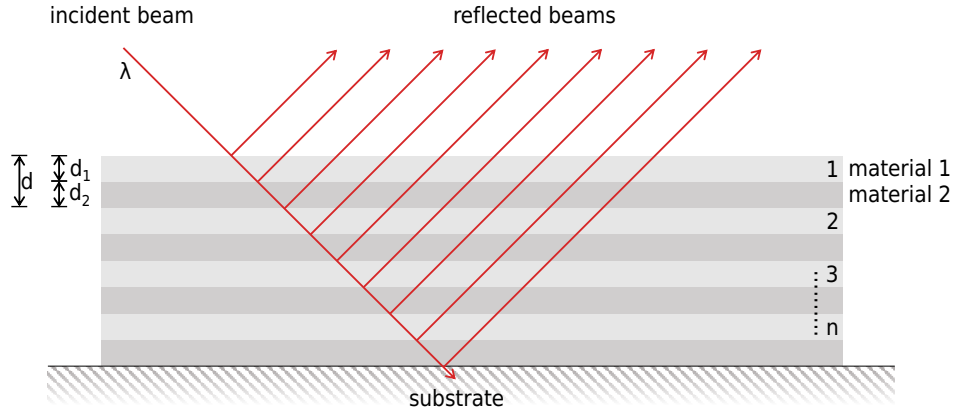


Figure 2.3: Schematic representation of an MLM consisting of n pairs of bilayers of thickness d . Materials 1 and 2 are low and high refractive index materials, respectively. The total reflectivity is the sum of the complex reflection coefficients at each interface.

reflectivity R is approximately given by:

$$R = \left[\frac{n_0 (n_2)^{2N} - n_s (n_1)^{2N}}{n_0 (n_2)^{2N} + n_s (n_1)^{2N}} \right]^2 \quad (2.4)$$

where n_0 , n_1 and n_2 are the respective refracting indices of the ambient medium, the two alternating materials, and the substrate, which terminate the transmission through the mirror. N is the number of repeated pairs of the bilayer materials. According to eq. (2.4), the optimum layer thickness is $\lambda/4$. There is constructive interference of the reflected light waves at many boundary layers in the $\lambda/4$ design leading to a high total reflectivity. Under the assumption that the two materials have a different index of refraction:

$$\lim_{N \rightarrow \infty} R = 1 \quad (2.5)$$

Theoretically, a 100 % reflection is possible. But in reality the MLM have a reflection quality of about 70 % [10]. Due to the relatively large number of mirrors required in the lithographical projection optics, which are installed successively in the scanner, even the slightest loss of reflectivity leads to significant losses in intensity. This, in turn, results in increased exposure times and reduction in productivity and thus profitability of the complex technology.

2 Introduction

And at this point, contamination of the collector mirror, which is located inside the plasma source and focusses the primarily generated EUV light into the following complex optics, with tin debris becomes a major problem. If the reflectivity decreases to the point where the wafer cannot be reasonable exposed anymore, thus the lithography process interrupted and the collector is cleaned or replaced.

In general, ionic and neutral tin debris from the tin plasma can damage a surface in three ways: deposition, sputtering, and implantation. The last two types of damage to the surface are irreversible and are the result of the high kinetic energy fraction (1 keV to 50 keV) of the ion debris[11]. The deposition of tin is a reversible process. The most established method for removing tin from the surface is etching using hydrogen species such as radicals, which converts the tin into the volatile stannane (SnH_4). Tin debris in particular, and debris and contamination mitigation in general, are the main impetus of this work. Therefore, they are discussed in detail in a separate section (cf. section 2.4.1).

The energy of the EUV photons is far above the ionization potential (IP, described in section 2.6.1.1) of all known elements and molecules. This means that every atom and molecule in the beam path absorbing a EUV photon is ionized. Due to the relatively small effective cross-section, hydrogen ($5.56 \times 10^{-24} \text{ m}^2$ for 92 eV photons)[12] is the most important background gas in the EUV scanner environment and the total pressure in the lithography tools is in the regime of a few Pascal, otherwise the energy of the photons would be completely absorbed on the way to the wafer. However, it is reasonable to assume that any gas in or near the path of the beam will be ionized upon EUV photon absorption. Consequently, a number of ion-molecule reactions will inevitably occur after primary excitation.

In the following section, the basis of the plasma theory is briefly discussed and related to the chemistry taking place relevant to this work.

2.3 Plasma

2.3.1 Plasma fundamentals

Plasma is a distinct state of matter characterized by a high degree of ionization in which a significant fraction of the particles are in the form of ions and free electrons. Consisting of charged particles interacting through electromagnetic forces, plasma exhibits a wide range of dynamic behaviours, including the formation of electric and magnetic fields, the generation of radiation, and the production of shock waves and turbulence. These properties render plasma a subject of intense interest in a wide range of scientific fields. The term

plasma was coined by Langmuir and Tonks, who related the apparently unregulated behavior to the blood plasma they were familiar with[13]. At the transition from neutral gas to the plasma state, the bulk properties change dramatically. As a result of the Coulomb forces, the charged particles strongly interact with each other. This results in a completely new behavior of the matter. In its entirety, plasma is an electrically neutral entity, despite the fact that it consists of charged particles, because there are exactly the same number of cations and electrons. This is called *quasi-neutrality*[14]. Within the plasma state, the following equation holds true:

$$n_e \approx n_i \quad (2.6)$$

where n_e is the density of electrons and n_i is the density of ions.

There are a variety of plasmas that are generated in different ways and have different properties. One way to characterize a plasma is the degree of ionization X , which indicates the ratio of ions/ electrons to neutral particles. Here n_0 is the density of neutral particles:

$$X = \frac{n_i}{n_0 + n_i} \quad (2.7)$$

The Eggert-Saha equation (eq. (2.8)) is a fundamental equation in the field of plasma research and describes the ionization state of a plasma in dependency of the temperature and the ionization energy in thermodynamical equilibrium.

$$\frac{n_i}{n_0} = \frac{(2 \pi m k_B T)^{\frac{3}{2}}}{n_0^{\frac{1}{2}} h^{\frac{3}{2}}} \cdot \exp\left(\frac{-E_i}{2 k_B T}\right) \quad (2.8)$$

where m is the atomic mass, k_B the Boltzmann constant, T the temperature, h the Planck constant and E_i the ionization energy. The equation essentially states that as the temperature of the plasma increases, the ionization fraction increases, because the thermal energy of the particles is sufficient to overcome the ionization energy of the atoms or molecules. Additionally, as the density of the plasma increases, the ionization fraction decreases, because the electrons and ions are more likely to recombine due to their closer proximity[14, 15].

Another way to classify a plasma is based on its temperature and temperature distribution. The most important categories include local thermal equilibrium (LTE) plasmas and non-local thermal equilibrium (non-LTE) plasmas. As the term suggests, in LTE plasmas electrons (e), ions (i) and neutral atoms or molecules (n) are in thermal equilibrium.

2 Introduction

This means that the particle densities, temperature, and electromagnetic radiation field are uniform throughout the plasma.

$$T_e \approx T_i \approx T_n \quad (2.9)$$

As a result, LTE plasmas can be described by the laws of thermodynamics, such as the ideal gas law and the Eggert-Saha equation. One important feature of LTE plasmas is their ability to emit and absorb electromagnetic (black body) radiation. Because the particle densities and temperatures are uniform throughout the plasma, the plasma is said to be in local thermodynamic equilibrium with the radiation field[14, 16].

In non-LTE plasmas the particles are not in thermal equilibrium with each other or with the electromagnetic radiation field. In non-LTE plasmas, the particle densities, temperature and radiation field can vary throughout the plasma, and the plasma may not be described by the laws of thermodynamics. The temperature T of ions and neutral particles has a significantly lower temperature than the electrons:

$$T_e \gg T_i \approx T_n \quad (2.10)$$

Due to the variations, the plasma may exhibit a wide range of dynamic behavior and properties, such as non-uniform ionization and excitation rates of atoms and molecules, and the generation of non-thermal plasma waves and instabilities. Since there is no equilibrium with the radiation field, defined spectral lines are emitted instead of black body continua[14, 16].

In summary, the classification of a plasma as either LTE or non-LTE is determined by various factors, such as its chemical composition, the type of collisions occurring, the type of electric field present, the method of ionization, as well as the prevailing temperature and pressure. In high-pressure environments, there are many collisions and thus energy exchange between the particles is efficient. However, in low-pressure environments, the molecular mean free path is much larger, resulting in fewer collisions and less efficient energy distribution[14, 16].

As mentioned before, a plasma is neutral as an entity, the so-called pseudo-neutrality. However, local deviations can occur, because opposite charges attract each other. These areas are called the Debye-sphere, and within this region neutrality is allowed to be compromised. The radius of the sphere is the Debye-length λ_D :

$$\lambda_D = \sqrt{\frac{\epsilon_0 k_B T_e}{n_e e^2}} \quad (2.11)$$

where ϵ_0 is the vacuum permittivity and e the elementary charge. Due to the charge imbalance, bulk systems are created that shield the inner charge from the outside; thus the electrical potential drops within a Debye-length. A denser plasma shields charge more efficiently, so the Debye-length decreases with increasing pressure, and also with decreasing temperature. Only if the spatial extent L is greater than the Debye-length λ_D can a gas be classified as a plasma ($\lambda_D \gg L$). Another criterion for a plasma is the so-called plasma parameter, which must be significantly greater than 1 ($N_D \gg 1$)[14, 16]. N_D is defined as follows:

$$N_D = n \frac{4}{3} \pi \lambda_D^3 \quad (2.12)$$

If an external, temporally changing electric field is applied, it will remain shielded as long as the Debye-sphere can exist in the electric field and can move as an unit. The plasma frequency ω_p describes the fastest possible change in charge density. Since the electrons are the lightest and thus the most mobile particles in the plasma, they determine the limits of effective shielding. ω_p is the angular frequency at which the electron density oscillates around the mean homogeneous density[14, 16]:

$$\omega_p = \sqrt{\frac{n_e e^2}{\epsilon_0 m_e}} \quad (2.13)$$

where m_e is the mass of the electrons.

The plasma frequency increases also with the square root of the particle density n and the quasi-neutrality of the system only exists when the temporal range is much larger than ω_p^{-1} . Furthermore, if the frequency of the external electric field is less than the plasma frequency ($\omega < \omega_p$) the electric field cannot penetrate the plasma and will be reflected[14, 17]. For the sake of completeness, there is also the plasma frequency of the ions ω_{pi} . It describes the ability of ions to respond to an alternating electric field. However, it plays a minor role, since the total plasma frequency is determined by the electrons.

$$\omega_{pi} = \sqrt{\frac{n_i e^2}{\epsilon_0 m_i}} \quad (2.14)$$

where m_i is the mass of the corresponding ion.

The conservation of energy applies without restriction to plasmas. That means that any absorbed energy must be balanced with the dissipative energy loss. The loss is mainly caused by collisions between electrons and neutral particles, which lead to ionization. However, in addition to the emission of energy as radiation, the loss due to the diffusion

2 Introduction

of charge carriers on surfaces is also important. When a plasma comes into contact with a surface, a thinner positively charged layer is formed, since the mobility of the electrons is much larger than that of the ions, and thus the electron loss is greater than ion loss. This layer is called plasma sheath[18]. The resulting net positive charge in the sheath forms a potential profile, which is positive within the plasma and zero near the surface. Electrons which are moving towards the surface are reflected back into the plasma volume, and plasma ions entering the sheath are accelerated towards the surface. This charge separation between the main plasma and the sheath regions is an important model to understand the properties of plasmas near surfaces[19].

The plasmas used in this work (cf. section 3.2) are operated at a pressure of 1×10^{-3} mbar to 1 mbar (low-pressure discharges) and are very unlikely to be anywhere near thermal equilibrium. Thus electrons, rather than the heavier ions or neutral particles, are affected by the energy supplied. However, this additional energy of the electrons can only be transferred to the ions inefficiently by collisions due to the large mass discrepancy. This means that the electron and ion temperatures are independent of each other, with the electron temperature being significantly higher than the ion temperature ($T_e \gg T_i$).

2.3.2 Plasma generation

There are many approaches to create and sustain plasmas. Basically, sufficient energy is added to the system so that the atoms and molecules ionize and thus charge carriers are present in the plasma. Due to loss processes (e.g. recombination, thermal conduction, radiation emission), new charge carriers must be generated in order to maintain the plasma, otherwise it expires. At this point, only a few methods that applied in this work or are thematically related are described in more detail. The range of possibilities is wide and practically every method that leads to ionization and subsequent secondary ionization can be used to generate plasmas[14].

The most commonly applied technique for generating plasmas is the exposure of neutral gas to an electrical radio frequency (RF) field. The majority of these plasmas are operated with a RF frequency of 13.56 MHz. In a neutral gas always a minor quantity of free electrons and ions is present, caused e.g. by the interaction with the cosmic microwave background (CMB). The electric field accelerates these charged particles. Under certain circumstances, electrons with sufficiently large kinetic energy are able to ionize atoms, ions or molecules

and that generate a pair of ion and electron. Under suitable conditions, this process can take place as an avalanche, provided that after the collision one existing electron becomes two. These processes are self-accelerating[14].

In a high frequency electric field, the energy absorption P_{abs} per volume V is given by:

$$\frac{P_{abs}}{V} = \frac{1}{2} n_e \frac{e^2}{m_e \kappa} \frac{\kappa^2}{\kappa^2 \omega^2} E_0^2 \quad (2.15)$$

where κ is the electron-neutral collision frequency, ω the angular frequency of the electromagnetic field and E_0 the energy of the electromagnetic field. When a magnetic field B (perpendicular to the electric field) influences the plasma, the energy absorption changes to:

$$\frac{P_{abs}}{V} = \frac{1}{4} \frac{e^2}{m \kappa} \left(\frac{\kappa^2}{\nu^2 + (\omega - \omega_c)^2} + \frac{\kappa^2}{\kappa^2 + (\omega + \omega_c)^2} \right) E_0^2 \quad (2.16)$$

where ω_c is the electron cyclotron frequency. As already discussed, an electric field with a frequency lower than the plasma frequency (cf. eq. (2.13)) cannot interfere with a plasma. However, due to the skin effect, the electric field can penetrate the plasma to a certain degree. The energy absorption is then reduced and limited to the skin sheath thickness.

In the case of an inductively coupled RF plasma, the energy is supplied via an inductive circuit element. Generally, the plasma is maintained by time-dependent magnetic fields, which were induced by the RF current. According to Faraday's law of induction as part of the Maxwell equations, a magnetic field that changes over time induces a rotating electric field. This field in turn induces an azimuthal electric field. Inductively coupled plasmas operates in two different modes, the E-Mode (electrostatic mode; capacitive coupling) and the H-mode (electromagnetic mode; inductive coupling)[19]. The energy coupling proceeds in the E-mode with low energy losses and is characterized by a low electron density in the plasma. Here, the coupling is essentially maintained by the potential difference between the electrode and the plasma. Due to the low electron density, the conductivity of the plasma is also low. The plasma is therefore transparent to the H-field and is alternating magnetic field does not supply any energy to the plasma. This situation changes as soon as there is a sufficiently high conductivity due to the free charge carriers. At a critical value, energy of the magnetic field can be supplied to the plasma. The additional energy contribution causes the system to change from E-mode to H-mode. This mode transition depends on many factors such as the matrix gas, the geometry, the distance between electrode and plasma and the electric current. In the H-mode, the coupled power corresponds to Faraday's law of induction. In H mode, the electron temperature is usually lower than

2 Introduction

in E mode due to the higher collision rate. Operating only a single mode is practically not feasible, since capacitive coupling always occur during inductively driven discharges. Often a plasma is ignited in the capacitive E-mode and the system then transitions into the inductive H-mode[19, 20].

Plasmas are also generate by intense supply of photons. When lasers are used as the energy source, two processes are particularly important: The first is the direct ionization of atoms and molecules when they interact with photons. When the photon energy is greater than the ionization potential (IP) (described in section 2.6.1.1), the process proceeds via single-photon ionization (SPI). At high photon densities, multi-photon ionization (MPI) may occur, where the sum of the individual energies of the quasi-simultaneously absorbed photons exceeds the IP. The excess energy remains in the electron as kinetic energy. In the second process the free primary electron released by the ionization process oscillates in phase with the alternating electromagnetic field of the laser radiation and thus gains additional kinetic energy. This process is known as inverse bremsstrahlung[21]. In a collision with a neutral atom, the electron is brought out of phase and the vibrational energy is converted into random thermal energy. The electron then has sufficient energy to ionize an atom or molecule in another collision. This secondary electron is also able to promote the process. This leads to a cascade-like increase of the charge carriers[20–22]. As long as the laser light is present, the plasma is sustained by these processes.

2.4 Debris

In extreme ultraviolet lithography (EUVL), debris is any form of particles that contributes to degradation of the mirror surfaces. This can be caused by thin, EUV radiation absorbing layers or by processes on the surface which affect the morphology or the functionality on atomic level. Debris can also be formed at surfaces by absorption of atoms, ions and molecules, which may form surface catalytic or radiation induced chemical bonds.

2.4.1 Tin debris

Tin (Sn) is a greyish (α -tin) or silver shiny (β -tin) metal with the atomic number 50 and belongs to the 14th group (carbon group) of the periodic table of elements. It is soft and malleable and has a comparatively low melting point of 505.08 K[23]. With ten stable isotopes, tin is the element with the most stable isotopes in the periodic table. Sn is mostly

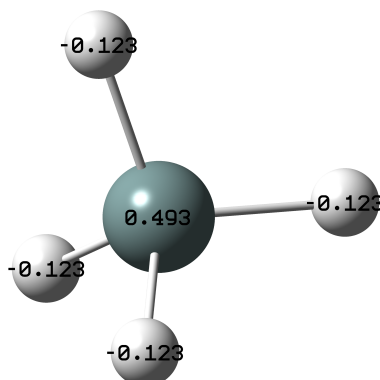


Figure 2.4: DFT calculated structure of SnH₄, labelled with the Mulliken charges.

present in the oxidation states +2 and +4; Sn(IV) is more stable because the inert pair effect is not that pronounced.

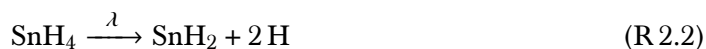
In LPP generated EUV radiation, a tin droplet is hit by a laser, which vaporizes the tin and creates a plasma (cf. section 2.2) which subsequently emits EUV radiation. However, the high-energy laser can also cause some energetic tin debris to be released, which can have charge states up to +15 or even more. These tin particles can react with the H₂ matrix gas in the scanner chamber to form the energetically most favourable electrically neutral product stannane (SnH₄). The calculated molecular structure of SnH₄ is shown in fig. 2.4 and the thermodynamic properties are listed in table 2.1.

2.4.1.1 Decomposition of stannane

At standard temperature and pressure (STP), stannane is a volatile thermodynamically unstable gas that has a tendency to spontaneous, slow decomposition into the elements[24]. The rate of decomposition is proportional to the temperature[25].



In addition to the spontaneous decomposition, photodissociation occurs upon high-energetic radiation exposure. In the presence of such a radiation source, the spontaneous decomposition is negligible. The initial step of the photodegradation can be separated in two reaction channels:

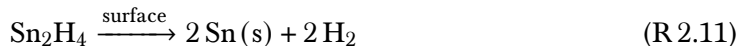
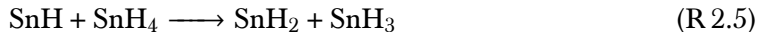


2 Introduction

Table 2.1: Properties and parameters of stannane[26, 27]

| | |
|----------------------|-------------|
| structure (VSEPR) | tetrahedral |
| bond length | 1.7 Å |
| melting point | 127 K |
| boiling point | 348 K |
| ionization potential | 10.75 eV |

Both reactions (eqs. (R 2.2) and (R 2.3)) have comparable standard enthalpies of reaction[28]. However, due to the high photon energies, these are not significant. Accordingly, both reaction paths are possible. The photolysis initiates a cascade of chemical reactions involving hydrogen and tin hydride species. The following chemical reactions including eqs. (R 2.2) and (R 2.3) correspond to the experimental observation of Aaserud et al.[28], where $[\]^*$ denotes a metastable state and M is another molecule or atom that is capable of receiving energy:



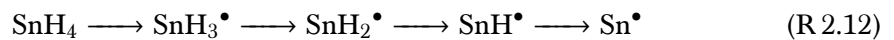
The dissociation reaction eq. (R 2.8) competes with the deactivation reaction eq. (R 2.9). The ratio between the two reactions depends on the partial pressure of M. The higher the partial pressure, the more the ratio shifts in the direction of the deactivation reaction. Equation (R 2.7) is probably a four-center reaction which is compatible with the RRKM theory[28].

The non-radiative dissociation reaction of stannane (cf. eq. (R 2.1)) accelerates in the presence of (reactive) surfaces (cf. eq. (R 2.10)). Pure metals act as catalysts in these

reactions. In contrast, metal oxides (M_xO_y) inhibit or suppress the dissociation process[24]. Decomposition on surfaces results in the formation of adsorbed Sn(s) and $2H_2(g)$ and follows a 1st order kinetics. Hydrogen desorbs from the surface as H_2 molecules, while the tin atoms remain on the surface and accumulate to form metallic tin.

The surface morphology of metals has a significant impact on surface-driven reactions. Molecules adsorb and dissociate most prominently on molecular steps and grain boundaries. At these sites on the surface, the reactions are sometimes several orders of magnitude faster than on plateaus[29, 30]. There are at least two effects that cause this behavior: The first is called coordinative unsaturated sites (CUS)[31]. The d-band model of Hammer and Nørskov offers a comparative theory[32]. The more steps and grain boundaries the adsorbate binds, the more pronounced the effect is. The second effect relates to the steric freedom of the adsorbed molecule. This allows the molecule to adopt a more energetically favorable conformation[33].

Increased dissociation rates at these sites is also observed for stannane. It is assumed that the dissociation process of SnH_4 is similar to that of SiH_4 on Si surfaces[34]:



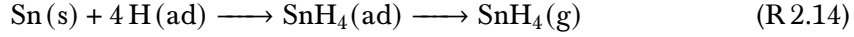
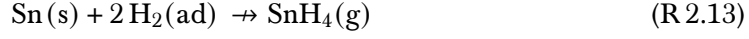
Processes such as the deposition and accumulation of particles on surfaces are described as layer growth in surface science. The layer growth can be separated into three principal cases. In reality, layer growth is distributed mostly between these simplified idealized models: The Volmer-Weber growth[35], the Stranski-Krastanow growth[36], and the Frank-van-der-Merwe growth[37–39].

Tin deposits on metal surfaces by forming tin islands according to the Volmer-Weber model at room temperature. This model is applied when the adhesion on the new layer is much higher than the adhesion on the clean surface. Three-dimensional structures (islands) with an average height of 40 nm are formed. [35]. The result of this mode is a very large surface area of adsorption material. At higher temperatures (≥ 330 K), to the Stranski-Krastanow model is more applicable. In this growth model, the adhesion on the clean surface is higher than the adhesion on the new layer. Therefore, a monolayer (wetting layer) is initially formed on the surface, and then the growth of the islands begins[36]. The third model is the Frank-van-der-Merwe growth, in which the adhesion on the new layer is comparable to the clean surface. As a result, the layers grow layer by layer without forming islands[37–39].

2 Introduction

2.4.1.2 Hydrogen etching of tin

At standard temperature, elementary tin does not react with molecular hydrogen (cf. eq. (R 2.13)). Atomic hydrogen (H), on the other hand, can react with tin to form stannane (cf. eq. (R 2.14))[40].



The reaction rate depends on the flux of atomic hydrogen onto the tin surface. At low fluxes, a passivation of the surface with atomic hydrogen is observed. Thus, further H atoms react back to the molecule $\text{H}_2(\text{g})$ without undergoing a chemical reaction with tin. At higher fluxes, the adsorbed H atoms are detached and removed from the surface by interaction with impacting hydrogen atoms. This creates new vacancies on the surface for chemical reactions[40].

At the surface Sn–H bonds begin to form. However, there is always the possibility of bond cleavage. When the adsorbed SnH_4 is finally formed, there may be partial desorption into the gas phase. The so-called etching rate depends strongly on the surface on which the tin is located. On catalytic active metals (e.g., Ru) the etching rate decreases over several orders of magnitude compared to non-catalytic surfaces. Van Herpen et al. observed a reduction of tin removal with atomic hydrogen of 28 nm min^{-1} to 0.3 nm min^{-1} when the tin was deposited on ruthenium.

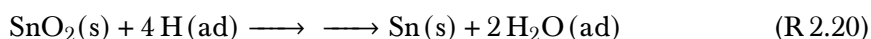
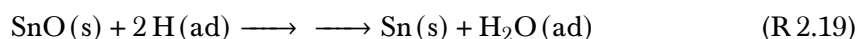
In reality, however, larger amounts of H atoms are required than stoichiometrically required. The Eley-Rideal mechanism describes the recombination of adsorbed H atoms with incoming H atoms from the gas phase. The resulting hydrogen molecule cannot react to form stannane[41]. The simplified reactions of the Eley-Rideal mechanism is shown in eqs. (R 2.15) to (R 2.18).



Where Ch–s and Ph–s are chemical and physical adsorption sites, H_{Ch} and H_{Ph} are chemically and physically adsorbed hydrogen atoms, k_1 and k_2 are the rate constants for chemical and physical adsorption and k_3 and k_4 are the rate constants for Eley-Rideal recombination with k_v as the desorption frequency.

The density of free adsorption sites mainly determines the probability of surface-induced recombination. Pure metal surfaces exhibit the highest density of these sites and therefore the highest loss rate of atomic hydrogen. Dielectric surfaces have the lowest density of adsorption sites; accordingly, these surfaces have the lowest loss rate. Semiconductors are somewhere in between these two extremes. By activating the surface, plasmas can strongly increase the surface loss rate. This activation occurs by an increase of adsorption sites due to surface cleaning cycles and the associated creation of new excited states by ion bombardment[41].

In the presence of even small amounts of oxygen, the dissociation of stannane on ruthenium is inhibited. A layer of tin oxide (SnO) is formed. Atomic hydrogen can reduce the tin oxide back to the pure metal and water as well as the SnO₂ that may have been formed in some other way[25, 42]:



The tin recovered in this way can react with the adsorbed H atoms to form stannane.

Although the reaction of H species with Sn to form SnH₄ has been described in several studies[43–45], there are only a few articles dealing with the quantification of the etching mechanism for the tin removal using reactive hydrogen.

In their studies, Elg et al. made several important observations regarding tin removal. Contrary to the commonly postulates, the limiting factor for the etch rate of tin using hydrogen plasma is not the radical density[45]. The experiments showed that the etch rate is not a function of the radical density. An increase in hydrogen pressure and the associated (non-linear) increase in radical density results in a small decrease of the etch rate. Further experiments have shown that the decomposition of stannane and possible redeposition of tin is not a major factor in limiting the removal rate. The deposition rate is significantly lower than expected, although it depends on the material and the behavior of the surface[25, 46]. According to Elg et al., the etching of tin is highly dependent on the ion energy flux. In fact, it is much more of an enabling factor than a limiting factor. Etching processes which are driven by ion bombardment are known as ion-enhanced etching (IEE) or reactive ion etching (RIE) and have often been used in lithography applications. For IEE and RIE, the etch rate increases as the impacting ions cleave the bonds of the surface

2 Introduction

atoms and molecules. Here, the plasma sheath directs the ions into the surface, causing Sn–Sn bonds to cleave. Consequently, the incoming radicals have a higher probability of forming Sn–H bonds and thus etching tin from the surface. The ion energy flux is the product of the amount of ions and their average ion kinetic energy, as it depends on the ion energy whether one (or more) bonds cleave. The ion flux is the amount of ions hitting the surface per unit of time[47]. A potential hypotheses for the lack of correlation between ion energy flux and etching rate in previous studies[43, 44] is that either the hydrogen plasma was remote and the ion energies were too low, or instead of a plasma, a neutral radical source was used, where only the radicals interact with the surface[47].

In summary, in the presence of high energy ions, the etching rate is increased due to the activated surface caused by ion bombardment. The actual formation of stannane is still based on the heterogeneous surface reaction between H radicals and Sn.

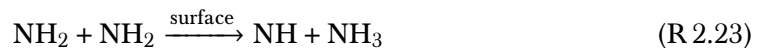
2.4.2 Debris of other elements

In addition to tin or tin hydride, there are other elements and molecules that can act as debris. Besides tin, this work focuses on the following elements: nitrogen (N_2), phosphorus (P), zinc (Zn), silicon (Si), magnesium (Mg) and copper (Cu). In terms of physical properties, only the corresponding metal hydrides are volatile. Molecules containing nitrogen are e.g., nitrides and amides, which remain adsorbed on the surface in a rather stable manner and can decompose back to the elements. The formation of these compounds is much less expected than the formation of hydrides. Therefore, the focus has been on the latter.

Ammonia (NH_3) is the most important nitrogen compound generated in a hydrogen plasma. At STP, ammonia is a colorless gas formed by heterogeneous surface chemistry. Initially, one nitrogen molecule (N_2) and three hydrogen molecules (H_2) adsorb and dissociate on the surface. The following steps lead to a successive bond formation between the nitrogen atom and three hydrogen atoms. NH_3 then desorbs from the surface. The dissociation of N_2 is the rate determining step, because of the stable $N\equiv N$ triple bond; the subsequent reaction steps are in equilibrium[33, 48]. The formation of ammonia is clearly favorable formed as compared to hydrazine (N_2H_4), which decomposes directly into the more stable NH_3 on surfaces[49]. In the presence of sufficiently energetic light, the nitrogen molecule can photodissociate and thus atomic nitrogen becomes available as a reaction participant in the plasma chemistry.

At temperatures below 500 K ammonia dissociates on surfaces via a Temkin-Pyzhev mechanism[30, 50]. The primary decomposition products of NH_3 are NH_2 and H (cf.

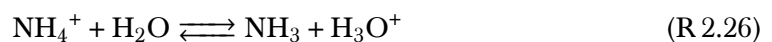
eq. (R 2.21)). NH originates through secondary processes on surfaces(cf. eqs. (R 2.22) and (R 2.23)). The dissociation products then form H₂ and N₂[51].



When the surface coverage of H atoms is close to zero, the formation of NH₃ stops, because all sites and steps of the surface for H₂ are occupied by N and NH_X. Small quantities of other atoms also deposit preferentially on steps and have an potential influence on the surface chemistry by inhibiting dissociation or undergoing reactions with themselves[29]. The reactive nitrogen species of the gas phase are mainly N₂H⁺ and NH₄⁺. Both species are generated by gas phase reaction with reactive hydrogen atoms:



The surface dissociation of N₂H⁺ and NH₄⁺ is not well known in the literature, but the chemical structure of the ions suggests decomposition to N₂ and adsorbed H on surfaces[52]. Ammonia subsequently desorbs as a gas or decomposes further on the surface. NH₄⁺ is in dissociation equilibrium with water:



In summary, in the presence of nitrogen and hydrogen, ammonia is inevitably formed on surfaces and affects both the surface chemistry and the gas phase chemistry. Due to the decomposition processes, adsorbed H atoms, N and NH_X are always present on the surface.

Based on the typical composition of the EUV plasma, phosphorus (P) is most likely present as phosphane (PH₃). At room temperature, phosphane dissociates on metal surfaces upon adsorption into elemental phosphorus and hydrogen. Although recombination is observed, it plays only a minor role. The intermediates PH and PH₂ are short-lived radicals that also result from photodissociation. PH₃ is therefore able to act as a debris[53].

2 Introduction

Reactive hydrogen can interact with copper to form the volatile but unstable copper hydride (CuH). At 330 K, CuH decomposes into the elements[49]. The rate of decomposition depends on the temperature, with higher temperatures accelerating the process[54]. The hydride is unstable in the presence of oxygen due to the energetically favorable oxidation to copper oxide (CuO). At room temperature, nitrogen cannot adsorb and dissociate on copper surfaces and there is no evidence in the literature that atomic nitrogen reacts with copper to form copper nitride or copper nitrogen compounds[55].

Magnesium hydride (MgH₂) is a white crystalline solid formed by direct catalyzed hydrogenation under high hydrogen pressure and decomposes back into magnesium (Mg) and hydrogen gas (H₂) at 560 K[56]. MgH₂ reacts with water to hydrogen gas and magnesium hydroxide (Mg(OH)₂). The physical properties do not indicate gas phase mobility. However, experiments, which are described later, demonstrate the existence of such volatile species.

2.4.3 Surface oxidation processes

In addition to oxygen, water is a major contributor to surface oxidation. A distinction is made between thermal and non-thermal (radiation-induced) processes[57]. When ionizing radiation interacts with surfaces, the dominant effect is a cascade of low-energy secondary electrons that can cause dissociations and chemical reactions both at the surface and in the gas phase. This is due to the excitation of the potential reactive particles. The threshold of the electron induced dissociation of H₂O into H + HO⁻ is 2 eV (cf. eq. (R 2.27)) and into 2H + O⁻ is 7 eV (cf. eq. (R 2.28)). Thus it is in the energetic range of the EUV radiation and of many other laboratory plasmas as well.

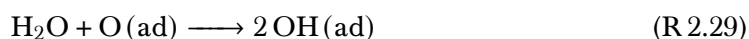


Water vapor adsorbs and desorbs reversibly on surfaces. Typically, the water molecule binds on metal surfaces with the O atom[58]. Thus, 2- and 3-dimensional structures are formed on the surface, which can be described with the bilayer model. The coverage of water of one bilayer is roughly 1.0×10^{15} molecules cm⁻². Under typical EUV conditions, however, there is no complete monolayer of water[57]. At room temperature and EUV conditions, the lifetime of an adsorbed water molecule is at less than 1 ms and in steady state equilibrium the surface coverage is roughly 1 %. The assumption is that only a small fraction

of the dissociated water fragments remain on the surface, mainly the oxygen atoms. The adsorbed O atoms lead to an increased adsorption of water caused the strong interactions with H₂O.

Adsorbed water dissociates on non-noble metal surfaces (e.g. Fe, V, W, Cr), but not on noble metal surfaces (e.g. Pd, Pt, Au, Ag). In this case, adsorption is fully reversible. The thermodynamic driving force is metal oxidation or formation of the corresponding metal oxides. There are some metals that represent a borderline case (e.g. Ru, Pt, Au). On these metals, molecular water adsorbs and desorbs reversibly, but depending on the surface temperature and crystallographic conditions, dissociation can occur[59].

Other species such as C–R, O and OH affect the binding strength of the adsorbed water molecules. Carbon compounds weaken the water-metal bond, while oxygen compounds can in some cases strengthen the bond. A low surface coverage of O atoms (<0.1 monolayer) favors the dissociation of H₂O by hydrogen abstraction[59, 60]:



The OH recombines and desorbs again as H₂O.



As the coverage of O(ad) approaches one monolayer, the adsorption probability of water decreases because the vacant adsorption sites are occupied by O[61].

Generally, the binding energy of water adsorbed on a metal oxide is less than that on a clean metal surface[59, 60]. A fraction of the adsorbed water also dissociates on metal oxides and OH remains on the surface. It can not be ruled out that the oxygen from the metal oxide reacts with the hydrogen atoms to form water. At steady state the surface coverage of H₂O is admittedly <1 %, but there is evidence that the OH coverage is nearly 1 monolayer[57].

2.5 Mass spectrometry

Mass spectrometry has its roots in the hypothesis of the English chemist William Prout, published in the early 19th century[62]. In the Prout hypothesis, named after him, he describes the observations that every atom has a defined mass and further that the atomic masses of the elements known at that time were whole multiples of the atomic mass of

2 Introduction

hydrogen. Prout postulated that hydrogen atoms, which he called protyles, are the intrinsic fundamental particles. The other elements are formed by the ensemble of different amounts of protyles[63]. However, the hypothesis proved to be incorrect when more accurate measurements of atomic masses were made by Jöns Berzelius in 1828 and Edward Turner in 1832. Chlorine's atomic mass (Cl) was 35.45 times that of hydrogen.

In 1886 Eugen Goldstein and Wilhelm Wien published the observation of anode rays or as Goldstein called them *Canalstrahlen* (standard translation of this term into English is canal rays) and their deflection by electromagnetic fields without realizing their importance to science[64, 65]. Beginning in 1897, J.J. Thomson studied the canal rays of various cathode materials, which he deflected with electromagnetic fields. On the basis of these observations, he established the correct equations for the relationship between mass, velocity, and orbital radius. In 1913 Thomson described a method of exposing photographic plates using a mass spectroscope. When ionized neon (Ne) was examined, two areas appeared on the photographic plate, from which he concluded that they must be neon atoms with two different masses (^{20}Ne and ^{22}Ne). Thomson's experiments laid the groundwork for the research and development of mass spectrometers, as they would later be called because of the changed detection scheme. In 1918 Arthur Jeffrey Dempster, a Canadian-American physicist, developed the first modern mass spectrometer. His instrument featuring a magnetic field analyzer was 100 times more accurate than previous instruments. He revolutionized mass spectrometry and laid the foundation for the design of mass spectrometers that is still valid today [66]. In 1919, Francis William Aston, a student of Thomson, developed also a mass spectrometer with a magnetic sector analyzer based on Thomson's and Dempster's results[67]. The new mass spectrometer could distinguish the isotopes of chlorine (^{35}Cl and ^{37}Cl), bromine (^{79}Br and ^{81}Br), and krypton (^{78}Kr , ^{80}Kr , ^{82}Kr , ^{83}Kr , ^{84}Kr and ^{86}Kr). All subsequent mass spectrometers are based on it.

2.6 Components and structure of mass spectrometers

New systems with dramatically improved performance have evolved since the first mass spectrometers were developed over 100 years ago. Today, there is an endless variety of ionization techniques and ion sources, analyzers and detectors, and even any combination of them, but the basic scheme for all types of mass spectrometers has remained unchanged. Figure 2.5 shows the fundamental structure of mass spectrometers. A mass spectrometer consists of a sample inlet, an ion source, a mass analyzer, and a detector, which are operated under various vacuum conditions. In principle, the neutral sample to be analyzed

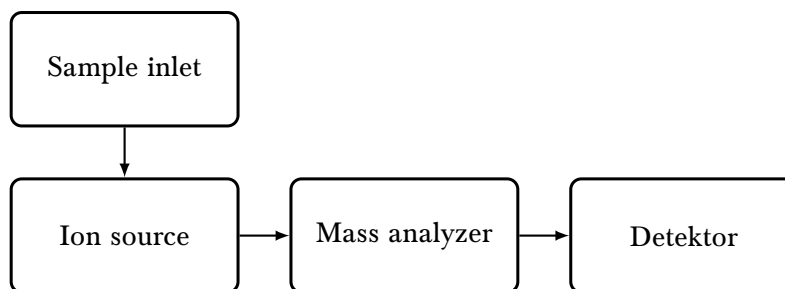


Figure 2.5: Fundamental structure of mass spectrometer

is transported to the ion source, is partly ionized and the generated ions are partly transferred to the mass analyzer. In the mass analyzer the ions are separated according to their m/z ratio and finally registered by the detector. m is the mass of the particle as a multiple of u and z is the charge state of the ion. The systems used in this study are described in detail later in this chapter.

2.6.1 Creating ions

In mass spectrometry, the analyte (one component in the sample being analyzed) must have a positive or negative charge. The types of samples that can be analyzed by mass spectrometry have been greatly dictated by ionization techniques and their development. The most common methods are direct or indirect ionization of the analyte. Depending on the method, the ionization occurs with subsequent fragmentation of the sample molecule so that charged fragments leave the ion source. In the following, the ion sources used in this work and the (chemical) processes taking place are explained in more detail.

2.6.1.1 Electron ionization

In 1902, Philip Lenard published the phenomenon of electron ionization (EI) by bombardment of atoms with low-energy electrons and its dependence on the electron energy[68]. Since these early days, there have been countless experimental and theoretical works that have significantly advanced the understanding of the interaction of energetic electrons with atoms and molecules[69]. Even today EI is the most common method for ionizing gaseous atoms or molecules; the principle of operation has practically not changed over the decades.

In the ion source, electrons emitted from a heated filament (thermionic emission [70]) are accelerated by electrical potentials and passed through the sample to be ionized inside

2 Introduction

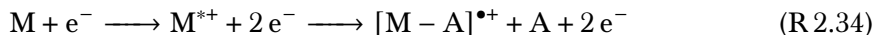
the ion source. When the energy of the electrons interacting with the atoms/molecules in the gas phase is at least equal to or greater than their ionization potential (IP) and there is adequate energy transfer (ionization cross section), some atoms/ molecules will be ionized with the loss of one or more electrons. Depending on the ion source used, the accelerating voltage varies from about 1 to 200 eV. Typically 70 eV electrons are used, because most atoms and molecules have their largest cross section for EI at or around this value.

For the simple system M (atom or molecule) there are different ionization cases depending on the energy of the interacting electrons and the nature of M[71].



Note that in the case of single ionization (cf. R 2.31) a positively charged radical cation $M^{\bullet+}$ is formed, while in the case of the doubly charged ion M^{2+} (cf. R 2.32) it is an even-electron ion or closed-shell ion. The triply charged ion $M^{\bullet3+}$ (cf. R 2.33) is again an odd-electron ion or open-shell ion and thus also a radical cation[71].

Due to the high excess energy deposited during the interaction of the 70 eV electron with the molecule, characteristic fragmentations occur. Therefore, EI is regarded as hard ionization method. In most cases, the molecular ion $M^{\bullet+}$ peak is not the base peak (i.e., the largest signal in a mass spectrum) and may not be detected at all[72]. The fragmentation process is based on the formation of a metastable radical cation $M^{\bullet+}$, which dissociates unimolecularly into a radical fragment cation and a neutral fragment A:



The rate of ionization R_i [s^{-1}] depends on the electron current I_e [A], the density of neutral analyte in the gas phase N_A [cm^{-3}], the ionization cross section for a given electron energy $\sigma_i(\text{KE})$ [cm^2], and the length of the ionization volume Δx [cm]:

$$R_i = I_e \cdot N_A \cdot \sigma_i(\text{KE}) \cdot \Delta x \quad (2.17)$$

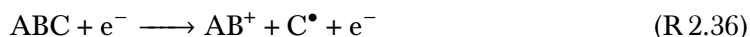
However, since the fragment pattern is almost specific to the molecule, a database can be used to compare the fragment pattern and thus identify the molecule.

In addition, the ionization process, the interaction between electrons and neutral particles, can also lead to different reaction paths, such as excitation without ionization, dissociative ionization, electron attachment, dissociative electron attachment, or ion pair formation[69]. For this purpose, the molecule ABC is considered.

Excitation:



Dissociative ionization (examples):



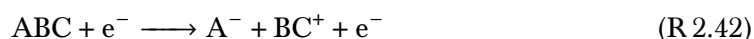
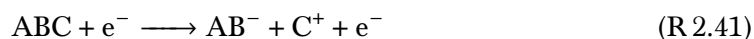
Electron attachment:



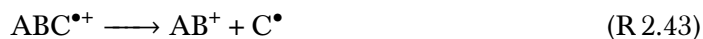
Dissociative electron attachment (examples):



Ion pair formation (examples):



Due to the high energy transferred from the electrons to the neutral particles, the resulting ions cannot be assumed to reside in their energetic ground state. Thus, there are possible further fragmentation reactions, which lead to the formation of a fragment ion AB^{+} and a neutral particle.



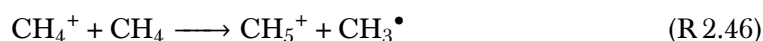
Equation (R 2.43) shows the formation of a neutral radical, while R 2.44 shows the generation of a neutral molecule. This preserves the radical cationic character in the molecule [71].

2.6.1.2 Chemical ionization

Chemical ionization (CI) is an ionization technique that is much softer than EI and thus less fragmentation of the analyte occurs after ionization. In CI, the ionized analyte species are formed by interaction of the corresponding molecules with ions in the gas phase. These are ion-molecule reactions, in which an electron, a proton or other ions are transferred to or abstracted from the analyte.

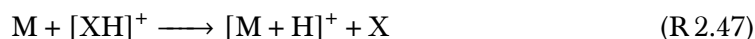
2 Introduction

The principles for this method originate from Tal'roze et. al.[73] observation that secondary processes occur at increased pressure within the EI source of his mass spectrometer. Tal'roze recognized a correlation between the pressure inside the EI source and the formation of H_3O^+ and CH_5^+ ions from water (H_2O) and methane (CH_4). The ratio of protonated vs. unprotonated analytes increases linearly with pressure. The following reactions of the formation of the protonated ions have been proposed[73]:



On this basis, M. Munson and F. Field showed in 1966 that CI is a versatile ionization method for mass spectrometry to determine analytes with minimal fragmentation[74]. Since CI is driven by bimolecular processes, a sufficiently high number of ion-molecule interactions within the ion source is mandatory, which is the reason why the method needs the increased source pressure. In general, there are five ways of transforming the neutral analyte molecule M into the corresponding positively charged ion. Here M is the analyte, H is hydrogen, X is the reactant gas and Y is a fragment[71].

Proton transfer:



Electrophilic additon:



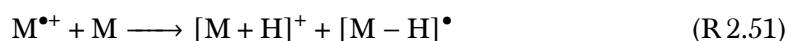
Anion abstraction:



Charge exchange:



Self-protonation:



Depending on the analytes to be ionized, suitable molecules are used as reactants. The typical examples are hydrogen (H_2), methane (CH_4) and ammonia (NH_3).

In this work, classical CI was not used. However, the work of Tal'roze et al. clearly demonstrated the presence of secondary processes in EI sources and the direct dependence on the operating pressure and the matrix gas. Even at regular operating pressures within the ion source, CI processes that affect the resulting mass spectrum can not be ruled

out. The most commonly used matrix gas in this work was H_2 . Thus, through secondary processes a proton source was always present within the ion source. The ratio of, for example, $\text{H}_3\text{O}^+/\text{H}_2\text{O}^+$ or $\text{N}_2\text{H}^+/\text{N}_2^+$ may indicate the influence of the secondary CI processes under prevailing conditions.

2.6.2 Mass analyzers

Mass analyzers separate different ions according to their mass-to-charge ratio. There is a broad spectrum of different analyzers, which are based on different physical principles, each with its own advantages and limitations. This section covers the mass analyzers used in this work, which are described in detail below.

2.6.2.1 Sector field mass spectrometer

A sector field mass spectrometer uses a static magnetic (B) or electric (E) sector, or a combination of both, where both fields act on the ions in turn. Two-sector mass spectrometers are the most common due to their many advantages, with the order of the sectors depending on the sector geometry and the purpose of the unit (e.g. EB and BE). However, there are also devices with three, four or more sectors, which were rarely commercially available. Modern sector field mass spectrometers are double-focusing. This means that they focus the ion beams from the ion source in both direction and velocity[75].

There is a linguistic distinction between a mass spectrometer and a mass spectrograph. In the former, the ions are focused on a point where the detector is located. By varying the field of the sectors, a scan is progressing through the m/z values. In the latter case, the ions are directed onto a planar surface separated by their mass. In the simplest case, this is a photosensitive plate or a flat detector array.

The principle of operation of a sector field analyzer is based on the deflection of accelerated charged particles in a magnetic or electric field. The radius of the circular path depends on the ion energy in the electric field and the ion momentum in the magnetic field. By knowing the charge, the energy and the momentum, the mass of the ion is directly deduced. Ions entering the sectors have a kinetic energy equal to the acceleration energy of the ion source, up to several thousands of electron volt (eV), gained upon leaving the source. The magnetic field is directed perpendicular to the angle of entry of the ions into the magnetic field, so that the Lorentz force is forcing the ions to follow a circular path[71].

2 Introduction

Figure 2.6 shows schematically the paths of ions through the magnetic field depending on their m/z .

The Lorentz force F_L is given in the simplest form by:

$$F_L = qvB \quad (2.18)$$

where q is the electric charge, v the velocity of the ion and B the magnetic field induction. An ion with the mass m , the charge z and velocity v moving perpendicular to a magnetic field follows a circular path with radius r_m . The Lorentz force F_L and the centripetal force F_c are equal along this path.

$$F_L = qvB = \frac{mv^2}{r_m} = F_c \quad (2.19)$$

By rearranging, the radius can be calculated:

$$r_m = \frac{mv}{qB} = \frac{mv}{zeB} \quad (2.20)$$

where z is the charge number and e the elementary-charge constant. Equation (2.20) shows the direct dependence of the radius on the momentum mv and thus on m/z . This kind of analyzer is basically an ion momentum analyzer. In addition, however, there is a directional focusing effect caused by the magnetic field. In this way, even ions that have a slightly different trajectory from the source are focused by the magnetic field to one point for each m/z [71].

The electrostatic analyzer (ESA) consists of two counter-charged plates that generate a radial electric field. The E-field extends over the ESA angle Φ . When an ion passes through the centre of the ESA, the following relationship holds:

$$F_e = qE = \frac{mv^2}{r_e} = F_c \quad (2.21)$$

where F_e is the electrical Force, E the electric field strength and r_e the radius of the ESA. Rearranging shows the dependence of radius r_e on ion energy E and m/z ratio.

$$r_e = \frac{mv^2}{qE} = \frac{mv^2}{zeE} \quad (2.22)$$

Thus, the ESA is only energy dispersive. The ESA is also directional, as is the magnetic sector. Ions entering the ESA centrally and at right angles with respect to the field lines

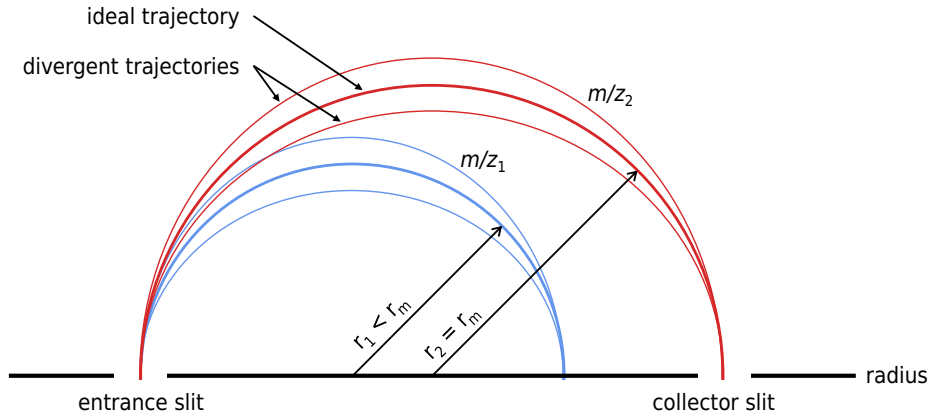


Figure 2.6: Schematic illustration of the directional focus of a 180° magnetic sector. A diverging beam of monoenergetic ions of the same m/z is shown as red curves (m/z_2) and the trajectory of the same kinetic energy but different m/z as blue curves (m/z_1). In this scheme the B field direction is out of plane for positive ions.

pass through it on an equipotential line. Divergent ions pass through the sector near one of the two plates and are focused on the exit slit. As an ion moves towards the outer plate, which is charged in the same way as the ion itself, it is slowed down by the electric field and eventually reflected inwards. Ions moving towards the inner plate are accelerated by the attractive potential. The centripetal force, which corrects the trajectory, is increased by the higher velocity. This keeps the ions on a stable trajectory[71].

By combining of the magnetic sector with the ESA, the energy dispersion of the magnetic field can be compensated by the electric field. The combination of the two sectors allows to construct an ionic optical system that focuses all the ions at a single point, regardless of small differences in energy and direction. This is called double focusing and increases the resolution by a multiple. From eq. (2.20) and eq. (2.22), it is clear that a mass spectrum is produced by varying of B and E . The variation of B it is a magnetic field scan and the variation of E is an energy field scan.

The modularization of double-focusing sector field mass spectrometers has resulted in a number of different geometries, each with its own advantages and limitations. However,

2 Introduction

most of current mass spectrometers do not fit neatly into one of these categories as designs have evolved, but they do provide a good explanatory basis. The classic geometries are EB configurations. The electric sector is placed in front of the magnetic sector. For technical and technological reasons, in the past photosensitive plates were often used as detectors at that time and a scanning sector was not used or was less accurate. By means of the spatial distance of the signals on the photographic plate, the mass-to-charge ratio of the ions was determined.

The Mattauch-Herzog geometry combines a 31.82° ($\pi/4\sqrt{2}$) electric sector with a 90° magnetic sector of opposite trajectory bending direction. This configuration provides high transmission efficiency of the ions and an energy focusing effect. These characteristics are useful in applications where the ions have a highly dispersed energy range and still require high sensitivity. The ions are focused on a flat plane. Therefore, photosensitive plates or flat detector arrays are used[71, 75, 76]. The Bainbridge-Jordan geometry consists of a 127.30° ($\pi/\sqrt{2}$) electric sector with a 60° magnetic sector following with the same bending direction. This configuration is often used for determining isotopic mass ratios. The ions are detected via a photosensitive plate[76]. In the Nier-Johnson configuration a 90° electric sector is combined with a subsequent 60° magnetic sector with the same bending direction. This geometry is designed to use a scanning magnet to successively focus ions of different m/z values onto a point detector[71, 75, 77].

In addition to these three most popular geometries, there are a variety of configurations that are tailored specific applications. Examples are the Hinterberger-König geometry (42.43° electric sector, 130° magnetic sector)[75, 78], the Takeshita geometry (two sequential 54.43° electric sector, 180° magnetic sector)[75] and the Matsuda geometry (85° electric sector, 72.5° magnetic sector)[75, 79].

In contrast to the EB configuration, many modern mass spectrometers have a BE configuration. In these instruments, the geometries were often the opposite of the ones already in use. For example, the double-focusing sector field mass spectrometer used in this work (section 3.3.1) operates with an inverted Nier-Johnson geometry. This allows both magnetic and electrical scanning, depending on resolution, mass range and scanning speed[71].

2.6.2.2 Time-of-flight mass spectrometer

The first time-of-flight (TOF) analyzer was invented by W.E. Stephens in 1946[80]. Nowadays, TOF mass spectrometers are one of the most widely used analyzers in mass spectrometry. The great advantages are, for example, the basically unlimited m/z range, acquisition of complete mass spectra, even for extremely short ionization events, and the compara-

2.6 Components and structure of mass spectrometers

tively simple design of these devices. The principle of TOF mass spectrometry is based on the time of flight of ions in a collision-free space. At the same kinetic energy, a spatial separation of ions of different mass occurs (cf. fig. 2.7).

The potential energy E_{pot} of ions in an electric field depends on the charge of the ion q and the potential of the electric field U :

$$E_{pot} = qU = ezU \quad (2.23)$$

When the ion is accelerated through the electric field by the voltage U , the potential energy of the ion is converted to kinetic energy. Where m is the mass and v is the velocity, the kinetic energy E_{kin} is given by:

$$E_{kin} = \frac{1}{2}mv^2 \quad (2.24)$$

Since the potential energy is converted into kinetic energy, eq. (2.23) is equal to eq. (2.24):

$$E_{pot} = E_{kin} \quad (2.25)$$

$$qU = \frac{1}{2}mv^2 \quad (2.26)$$

Because there are no collisions and no electric or magnetic fields in the drift tube, the velocity of the ions inside the tube does not change. Velocity is the quotient of the distance d and the time t it takes the ions to travel through the drift tube.

$$v = \frac{d}{t} \quad (2.27)$$

By substituting the velocity of eq. (2.27) into eq. (2.26), the following holds:

$$qU = \frac{1}{2}m \left(\frac{d}{t} \right)^2 \quad (2.28)$$

By rearranging to t , the following relationship is obtained:

$$t = \frac{d}{\sqrt{2U}} \sqrt{\frac{m}{q}} = k \sqrt{\frac{m}{q}} \quad (2.29)$$

k contains constants (d , U) related to instrument settings and dimensions that do not change during an analysis. Equation (2.29) shows the relation between the time and the square root of its m/q and thus m/z [71].

2 Introduction

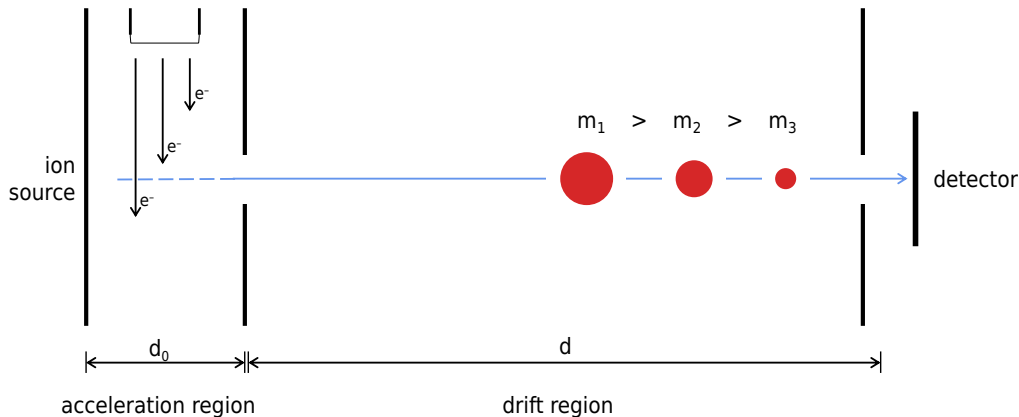


Figure 2.7: Schematic representation of a linear time-of-flight (TOF) mass spectrometer.

Ions generated in the ion source (exemplarily with an EI source) are accelerated by electric potentials (acceleration region, d_0). During their flight through the field-free drift region d , the ions are separated in time due to their different velocities. Lighter ions reach the detector earlier than the heavy ions ($m_1 > m_2 > m_3$).

In general, a distinction is made between a linear TOF analyzer and a reflectron TOF analyzer. In linear TOF geometry, the entrance and the exit regions of the field-free space are on-axis. The reflectron acts as an ion-mirror, which is increasing the drift distance and is temporally focusing ions with different kinetic energies. The reflector consists of a series of electrodes with increasing electrode potentials, which are located at the end of the drift tube. This provides a retarding electric field which decelerates the penetrating ions and accelerates them in the opposite direction. Ions with higher kinetic energy penetrate the electric field deeper and thus spend more time in the field. This causes a correction of the time of flight and thus a higher resolution[71].

2.7 Quartz crystal microbalance

The quartz crystal microbalance (QCM) is an instrument for the measurement of the change in mass per unit area on the surface of a quartz crystal resonator by recording the change in oscillating frequency. Applying alternating voltage to a specially cut quartz

crystal (e.g. AT-cut) induces a standing shear wave oscillation due to the piezoelectric effect. A QCM sensor consists of a thin disk of quartz crystal, on which metal (usually Au) is vapor-deposited as an electrode on both sides. These electrodes are used to apply AC. The frequency of crystal oscillation depends on the thickness of the crystal, among other factors. At unchanged conditions, a resonance frequency (mostly 5 GHz or 10 GHz) is established. Changes in mass on the crystal surface, such as deposition or etching, cause a change in frequency. An increase in mass causes a decrease in frequency and vice versa. With simplified assumptions, the Sauerbrey equation[81] allows a quantifiable correlation between the frequency change Δf and the mass change Δm on the quartz sensor:

$$\Delta f = -\frac{2f_0^2}{A\sqrt{\rho_q\mu_q}}\Delta m \quad (2.30)$$

Where f_0 [Hz] is the resonance frequency of the fundamental mode, Δf [Hz] the frequency difference, Δm [g] the mass difference, A [cm²] the piezoelectrically active crystal area between the electrodes, ρ_q the density of quartz ($\rho_q = 2.648 \text{ g cm}^{-3}$) and μ_q the shear modulus of quartz for AT-cut crystal ($\mu_q = 2.947 \times 10^{11} \text{ g cm}^{-1} \text{ s}^{-1}$). Sauerbrey's equation is only valid for systems in which the following three conditions are fulfilled, since an increase in mass on the electrode surface is treated as an increase in the thickness of the quartz disc: (i) the deposited mass must be rigid, (ii) it must be uniformly distributed and (iii) the frequency change must be $\Delta f/f > 0.05$ [82].

During a series of measurements with the QCM, it is necessary to maintain the same external conditions. For example, temperature variations, air humidity variations and deformations such as external forces or residual stresses affect the resonance frequency of the sensors. Due to the design, such conditions inside at plasma chamber are very stable. To ensure that the QCM measurement always takes place at the same temperature, a period of time is waited after the sensor has been exposed to the plasma to allow the sensor, which may have been heated by the plasma, to cool down.

3 Methods & Instrumentation

3.1 Chemicals

Nitrogen (N_2 , 5.0 purity, Messer Industriegase GmbH, Germany) or boil-off nitrogen (Linde Gases Division, Pullach, Germany) was used to operate the various instruments, such as venting, as sealing gas or as an admixture in plasmas. Hydrogen (H_2 , 5.0 purity, Messer Industriegase GmbH, Germany) or hydrogen from a hydrogen generator (7.0 purity, NM Plus 1000 Hydrogen Generator, VICI AG International, Switzerland), deuterium (D_2 , 5.0 purity, Messer Industriegase GmbH, Germany), oxygen (O_2 , 2.0 purity, Messer Industriegase GmbH, Germany), and argon (Ar, 5.0 purity, Messer Industriegase GmbH, Germany) were used as matrix gases for plasmas or as additions to hydrogen plasmas.

For the synthesis of stannane the following chemicals were used in analytical purity: Lithium aluminium hydride (LiAlH_4 , Sigma Aldrich GmbH, Munich, Germany), 1,2-dimethoxyethane (DME, $\text{CH}_3\text{OCH}_2\text{CH}_2\text{OCH}_3$, Sigma Aldrich GmbH, Munich, Germany), dibutyl ether ($[\text{CH}_3(\text{CH}_2)_3]_2\text{O}$, Sigma Aldrich GmbH, Munich, Germany), and tin(IV)-chloride (SnCl_4 , Sigma Aldrich GmbH, Munich, Germany). Liquid nitrogen (N_2 , Linde Gases Division, Pullach, Germany), dry ice (CO_2 , Linde Gases Division, Pullach, Germany) and toluene (C_7H_8) slush was used for cooling.

3.2 Plasma sources

In this work, two different plasma sources have been used to accommodate the different interfaces for the coupling to the different mass spectrometers (cf. section 3.3). Both sources generate hydrogen plasmas, and are powered by RF-generators at 13.46 MHz.

3.2.1 Plasma chamber

In a dedicated plasma chamber (custom CF-100 T-piece with 3 additional CF-40 flanges; Pfeiffer Vacuum, Asslar, Germany), a low-pressure (5×10^{-4} mbar to 1 mbar) hydrogen (H_2) RF plasma is used to generate the corresponding metal hydride products. The RF plasma

is sustained by an RFG-13-100 RF-generator (Barthel HF-Technik, Aachen, Germany) with 13.56 MHz at 100 W, which is electrically connected to a disc-shaped electrode at the bottom of the chamber. The matching network MatchingCube i-300 with 40.68 MHz at 300 W (Barthel HF-Technik, Aachen, Germany) is connected between generator and electrode (load) and is crucial for a correct impedance matching by transforming the impedance relationship between source and load. A scheme of plasma chamber is shown in fig. 3.1.

Several pressure gauges (PKR 261; Pfeiffer Vacuum, Asslar, Germany) are used to measure and monitor the pressure in the chamber. A turbomolecular pump (Turbovac 350i; Leybold GmbH, Cologne, Germany) is connected to the chamber via a large-diameter butterfly valve (VAT 61540-CECK; VAT Vakuumventile AG, Haag, Switzerland) to evacuate the chamber ($<1.0 \times 10^{-8}$ mbar) and achieve a high level of cleanliness. Using a mixing apparatus with a series of mass flow controller (MF-1; MKS Instruments Deutschland GmbH, Munich, Germany) of different sizes, the pressure in the plasma region can be varied over a wide range and different gas mixtures can be added to the plasma. In addition, the pressure can be precisely adjusted during plasma operation by controlling the valve, in order to allow gas to flow through at a constant pressure. A quartz window allows visual inspection and spectroscopic measurements of the plasma.

There are several ways to bring one or more optional samples (usually metals for which the corresponding hydrides are to be formed) into the plasma region. The sample can be positioned within the chamber using fine wires. Since there is no contact with the chamber surface, an additional electrical potential can be applied to the sample via an electrical feed-through.

3.2.2 Helical coil resonator

As a second option, a custom electrode-less, HCR C210 OEM power supply (Heraeus GmbH, Hanau, Germany) provides the RF energy to sustain the gas discharge. The plasma in a helical resonator belongs to the class of inductively coupled plasmas and is therefore classified as a high-density plasma[19]. The source operates around 13 MHz with a power input of approximately 0.5 W and does not require an external matching network. Instead, a potentiometer allows the oscillating circuit to be tuned to the prevailing conditions.

For regular applications an 0.5 inch diameter, cylindrical VUV lamp body is inserted into the coil of the resonator. Depending on the desired wavelength, lamps with different gases are available. For this work, the source was modified by replacing the lamp body with an open glass tube. This was done by drilling a hole in the PCB of the RF power supply to match the outer diameter of the glass tube. The resonator coil was centered with PVC

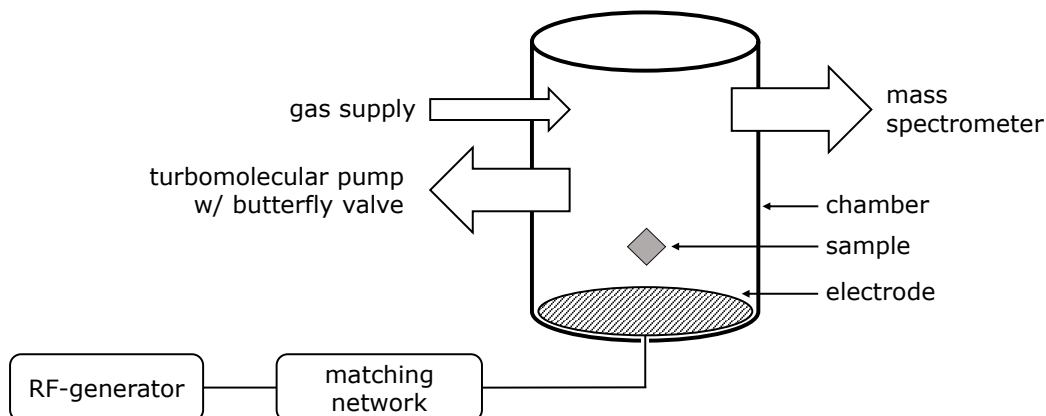


Figure 3.1: Schematic diagram of the plasma chamber and peripherals.

supports for axial alignment. The glass tube used is made of borosilicate glass (DURAN[®], Schott AG, Mitterteich, Germany) and has the same outer diameter as the original VUV lamp body ((12.09 ± 0.15) mm). The wall thickness is (0.94 ± 0.07) mm and the length of the tube is customized to the respective experimental set-up. In addition, one transistor of the circuit board was replaced with a BD 139 transistor (STMicroelectronics, Geneva, Switzerland). This change increases the power distribution to the coil and thus increases the plasma density and volume.

The hydrogen plasma is fed by an adjustable continuous gas flow (1×10^{-4} mbar to 10 mbar) via MFCs. A sample can be placed inside the glass tube between plasma and mass spectrometer. The species formed in the plasma are transported by the gas flow and are brought into contact with the (solid metal) sample. A scheme of the system is shown in fig. 3.2.

3.3 Mass spectrometers

Mass spectrometry is the fundamental analytical method in this work. Several different mass spectrometers have been used, depending on the scientific question and the hardware capabilities of the instruments. The systems described below are the majority of those used.

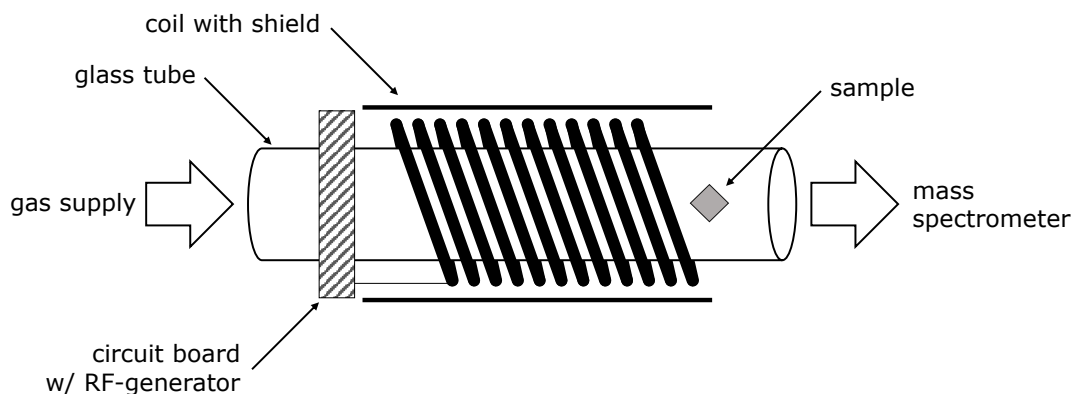


Figure 3.2: Schematic illustration of the HCR system.

3.3.1 Sector field mass spectrometer - MAT95XP

The MAT95 XP is a high-resolution double-focusing sector field mass spectrometer with an inverted Nier-Johnson geometry (Thermo Fisher Scientific, Waltham, MA, USA). For the detection of neutral plasma-generated molecules, the plasma chamber is directly coupled to the mass spectrometer and neutral particles are flushed from the plasma region into the ion source via the gas flow and ionized in the mass spectrometer via EI at 70 eV. As the ion source in these instruments operates at +5 kV (positive ion mode), no plasma generated positively charged particles can reach the mass analyzer. Accordingly, only the ions generated by means of EI are detected. A dedicated ion source turbo pump ensures minimum background pressure. As a result, only minor amounts of air etc. are recorded in the mass spectra.

This mass spectrometer offers many ways to introduce samples. There are flanges on both sides and on the front, allowing for easy and adjustable mounting. The ion source is designed to be accessible from the sides, front and top (CI gas addition and liquid analyte addition via an evaporation unit), providing maximum flexibility for experimental set-ups. The plasma chamber (cf. section 3.2.1) is coupled to the source head of the mass spectrometer via a borosilicate glass tube (DURAN[®], Schott AG, Mitterteich, Germany) with an outer diameter of (12.09 ± 0.15) mm, a wall thickness of (0.94 ± 0.07) mm and a

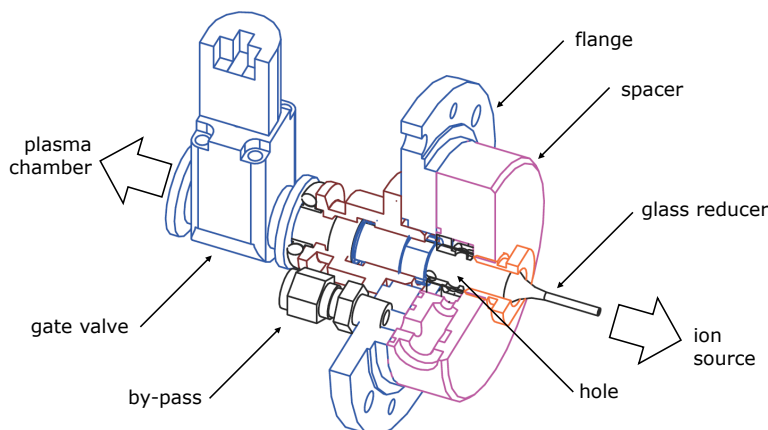


Figure 3.3: CAD drawing of the custom inlet system of the MAT95 XP mass spectrometer.

length of roughly 35 cm through a side flange. Figure 3.3 displays an illustration of the custom inlet system. A glass reducer with an inner diameter of approximately 1.5 mm acted as a gas flow restrictor to provide a sufficiently low gas load for the sector field mass spectrometer. The reducer is held by the flange and a spacer (cf. fig. 3.3) and is sealed with Viton rings. This component is made of glass because of the lower decomposition rate of metal hydrides and simultaneously acts as an insulator, since the ion source is on a high electric potential. The latter is also the reason that the spacer is manufactured from the PEEK polymer. If necessary, the reducer can be pumped as a bypass through an orthogonal hole. This reduce the gas load for the mass spectrometer and provides an overall higher flow velocity in the glass tube. A gate valve, which has the same internal diameter as the tube when in open position, is located between the glass tube and the reducer to separate the chamber from the mass spectrometer. It is also possible to add hydrogen directly into the instrument EI source via the CI gas port.

3.3.2 Time-of-flight mass spectrometer

3.3.2.1 LTOF

The LTOF is an orthogonal time-of-flight (TOF) mass spectrometer (TOFWERK AG, Thun, Switzerland) with a mass resolution of 10 000, a mass accuracy (RMS-error) of <5 mDa and a selected mass range from m/z 1 - 500. This allows highly selective identification of ion species by accurate mass and isotopic pattern analysis. In theory, the mass range of a TOF is infinite, however, the m/z of the ions of interest in this work is <500, so

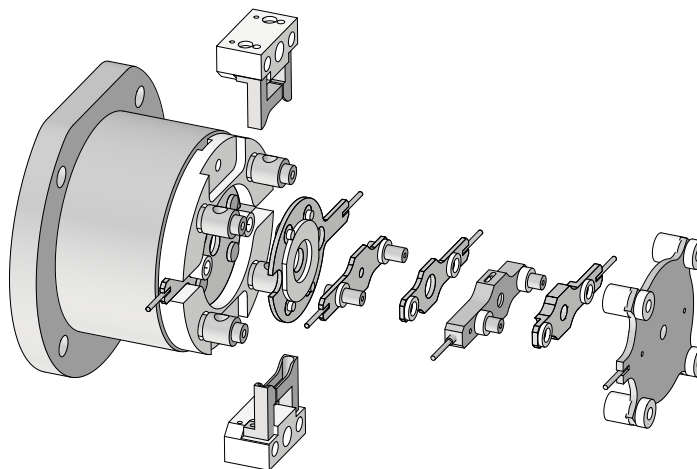


Figure 3.4: CAD exploded assembly drawing of the custom EI source of the LTOF.

the selected mass range is low in favor of a higher TOF repetition frequency. The LTOF contains a transfer quadrupole that transfers the ions from the ion source to the analyzer and additionally acts as a high-pass and/or notch filter. As a high-pass filter, the quadrupole only transmits ions with an m/z above the low-mass cut-off, which is proportional to the amplitude of the applied RF voltage. This can be used to filter out light matrix gases, such as hydrogen, to reduce the ion load on the detector. This allows the detector to operate at higher voltages, which in turn improves detection of the small target species signals. The notch filter works in a similar way, but filters out selected narrow m/z . However, depending on the width of the filter, the intensity of the adjacent signals will be discriminated as well.

Ion source

A custom ion source (cf. fig. 3.4) allows the measurement of neutral molecules via electron ionization (EI) at 70 eV as well as the sampling and measurement of native ions directly from the plasma region by adjusting the respective source electrode potentials. This switching between EI mode and transmission mode is made possible by the custom source design, which is tailored for these purposes. The source is on-axis with the plasma chamber and the transfer quadrupole of the TOF.

The EI source consists of several stainless steel electrodes, which are stacked on four guiding rods. In order to apply electrical potentials to the individual electrodes, they are electrical isolated from each other by ceramic spacers (MARCOR[®]). They are held in

3 Methods & Instrumentation

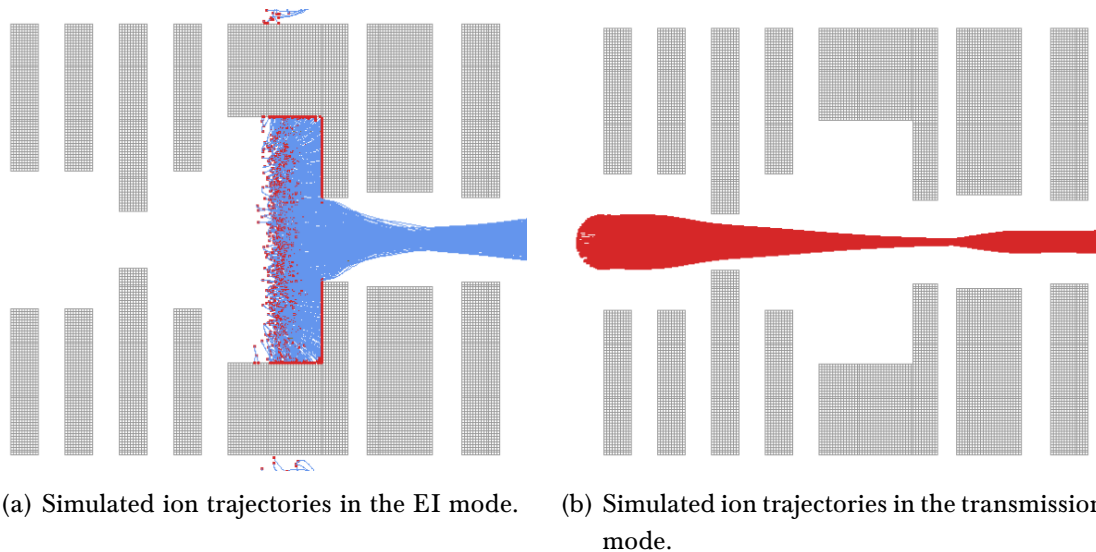


Figure 3.5: Simion ion trajectory simulations of the custom LTOF ion source.

place by springs, which gently push the stack into position and compensate for thermal expansion of the material. This reduces the force on the fragile ceramic spacers. The wiring is made of enameled copper cables which are suitable for use in high vacuum. By adapting the control software by the manufacturer, the source can be operated and controlled in both modes from the LTOF's control software.

The source is designed for additional upstream coupling to a hexapole ion guide transfer stage which is intended to ensure a almost loss-free transport of ions from the hexapole ion guide inlet port through the source into the analyzer of the LTOF, as well as efficient ionisation of the neutral gas by EI. Figure 3.4 shows the schematic of the custom EI source. There are electrodes (entrance, focus 1) at the source entrance which focus the ion beam leaving the hexapole ion guide transfer stage into the 3rd electrode (focus 2) which acts as a gas flow restrictor to ensure the required low pressure within the LTOF. By using electrodes with different diameters, the source can be modified for different experiments and pressure conditions. An additional electrode (repeller) focuses the ions into the ion source electrode (chamber), which is a cylinder acting as the ionization volume. Two tungsten (W) filaments are positioned opposite of each other outside the cylinder. A corresponding Wehnelt electrode directs the electrons through slits into the ionization volume. The ion extractor (extractor) pulls the ions towards the source exit, where they are transferred and focused via the last lens (quad lens) into the quadrupole.

Table 3.1: Exemplary voltages of the custom ion source in the EI mode.

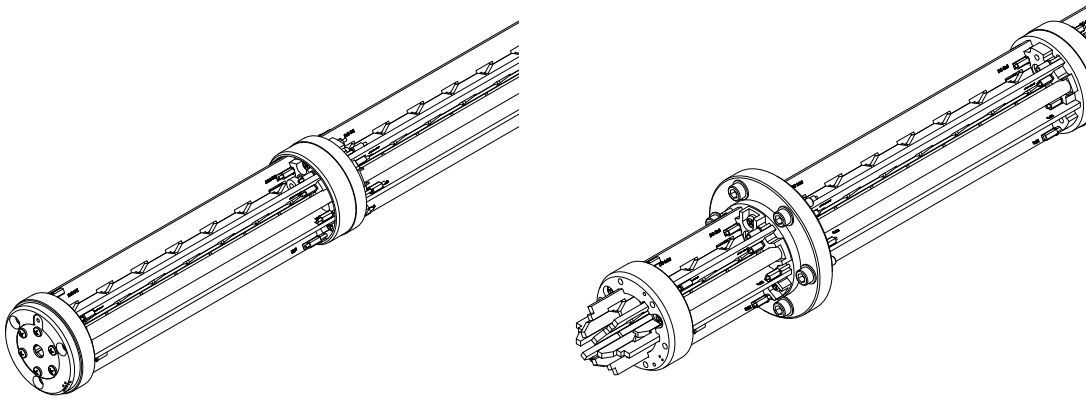
| | EI mode / V | transmission mode / V |
|-----------|-------------|-----------------------|
| filament | -70.000 | 0.000 |
| entrance | 0.000 | -100.000 |
| focus 1 | 0.000 | 0.000 |
| focus 2 | 0.000 | -165.000 |
| repeller | 3.400 | -100.000 |
| chamber | 0.000 | -165.000 |
| extractor | -7.768 | -18.005 |
| quad lens | -135.000 | -54.000 |

Figure 3.5 shows simulated ion trajectories in EI mode (fig. 3.5a) and transmission mode (fig. 3.5b) of the ion source. In EI mode, the ions formed by EI are actively extracted from the ionization volume. In this mode, the first three electrodes (entrance, focus 1, focus 2) are without function, apart from the gas flow restriction of the focus 2 electrode. A low positive voltage is applied to the repeller electrode to act as a pusher. This voltage is also sufficient to keep out plasma-generated ions so that only the ions of the neutral particles are detected. In transmission mode, an Einzel lens is formed by applying corresponding voltages to the first three electrodes (entrance, focus 1, focus 2). The Einzel lens is an electrostatic lens that has the advantage of focusing the ion beam from the hexapole transfer exit without changing the ion energy. The applied voltages depend on the DC potential ramp of the hexapole ion guide. Table 3.1 lists the respective electrode potentials for the EI mode and the transmission mode as examples.

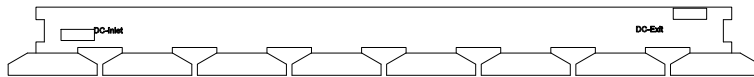
Hexapole ion guide transfer

The LTOF can be coupled to the plasma chamber in different ways, depending on the measurement method. For the measurement of native (i.e. plasma generated) ions, a custom hexapole ion guide transfer stage (Fasmatech Science and Technology, Athens, Greece) connects the plasma chamber to the LTOF. Figure 3.6 shows a CAD drawing of the hexapole ion guide transfer stage, which consists of four segmented hexapole modules, each equipped with eight electrodes, an exit hexapole module with five electrodes (cf. fig. 3.6b) and an entrance electrode (cf. fig. 3.6a). The total hexapole ion guide length

3 Methods & Instrumentation



(a) Hexapole ion guide transfer: entrance lens. (b) Hexapole ion guide transfer: exit geometry.



(c) Hexapole segment.

Figure 3.6: CAD drawing of the hexapole ion guide transfer.

is 628 mm and 630 mm with entrance lens. The hexapole ion guide is made of glass-fiber reinforced plastic (GFRP). The surfaces of the electrodes facing the center are coated with gold (cf. fig. 3.6c). The circuits are modularized and are located directly on the GFRP of each segment. PEEK components with wire feedthroughs between the segments connect and support the modules. The dimensions are designed to fit the ion guide into a CF40 tube system, which connects the LTOF to the plasma chamber. The exit module extends into the LTOF and is terminated by the ion source. The RF-generator for driving the hexapole ion guide electrodes is attached to the CF40 tube system and connected to the hexapole rods via wire feedthroughs. The RF amplitude, potential of the entrance lens and DC ramp voltages can be controlled by the manufacturer's software. The DC ramp of the on guide is linear and defined by the first and last segment's DC potentials. The ramp determines the kinetic energy of the ions and must be matched to the potentials in the ion source and the TOF optics.

3.3.2.2 CTOF

A CTOF time-of-flight mass spectrometer (TOFWERK AG, Thun, Switzerland) with a mass resolution of 1000 and a selected mass range from m/z 1 to 500 was used for similar tasks. It contains a cross-beam EI ion source (Pfeiffer GmbH & Co. KG, Ablar, Germany), which can again be switched between EI mode and transmission mode by modification. The control of the lens potentials and the two tungsten filaments is handled by a power supply box (QMS 700, Inficon, Bad Ragaz, Switzerland) and appropriate software. Due to the design of the custom ionization chamber with an additional fore pump and larger pump cross sections, the CTOF tolerates much larger gas loads than the LTOF. This allows plasma experiments to be performed at higher pressures.

The CTOF is coupled to the HCR plasma source (cf. section 3.2.2), which is mounted on a borosilicate glass tube (DURAN[®], Schott AG, Mitterteich, Germany) with an outer diameter of (12.09 ± 0.15) mm, a wall thickness of (0.94 ± 0.07) mm and a variable length. The glass tube extends into the mass spectrometer and ends approximately 5 mm in front of the ion source and is sealed with Viton rings. An orifice acts as a flow restrictor to create a pressure gradient between the plasma region in the glass tube and the ion source. By applying a potential to the orifice, ions are actively drawn into the ion source and from there further into the analyzer. The HCR can be positioned on the glass tube to change the distance between the plasma and the ion source.

3.4 Quartz crystal microbalance

openQCM (Novaetech S.r.l., Pompeii, Italy) is an open source project (hardware and software), in which the QCM system consists of an Arduino Micro as microcontroller board and a QCM Arduino shield. The QCM Arduino shield is a custom designed circuit board for QCM applications that contains a crystal oscillator driver in Pierce oscillator configuration which is optimized for quartz sensors operated at 10 MHz as well as 1 MHz to 6 MHz with a jitter up to 0.1 Hz. The oscillator driver is designed to operate with 3.3 V at 24 mA and can thus be directly supplied by the Arduino Micro. In addition, the Arduino Micro handles the communication with the data acquisition software running on a personal computer and reads the oscillation frequency from the QCM Arduino shield. The oscillator is connected to the sensor located near the plasma inside the plasma chamber via vacuum feedthroughs. The sensors are piezoelectric quartz crystal discs with gold electrodes on both sides (cf. fig. 3.7). A contact pad on each edge is connected to an electrode on one side. Their characteristics are shown in table 3.2.

For etching experiments, the gold electrodes are coated with a tin layer. Quantitative measurements can be made by directly recording the change in mass on the sensor causing a change in the oscillation frequency.

3.4.1 Electrode coating

In this work, the sensors were coated in two different ways: (1) electroplating and (2) physical vapor deposition (PVD).

For the electroplating process, the sensor was immersed in an aqueous solution of tin(II) sulfate (SnSO_4), diluted sulfuric acid (H_2SO_4) and ethanol ($\text{C}_2\text{H}_6\text{O}$). As a contact at the

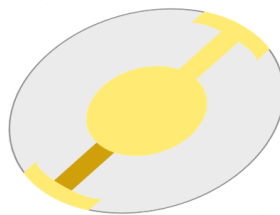


Figure 3.7: Schematic of a quartz crystal microbalance sensor.

Table 3.2: Specifications of the QCM.

| | |
|---------------------|---|
| quartz frequency | 10 MHz |
| nominal sensitivity | $4.42 \times 10^{-9} \text{ g Hz}^{-1} \text{ cm}^{-1}$ |
| cut | AT-fundamental |
| cut angle | $35^{\circ}15' \pm 3'$ |
| quartz thickness | 160 μm |
| blank diameter | 13.9 mm |
| electrode diameter | 6 mm |
| electrode material | Au |
| electrode coating | Au-Ti substrate |
| electrode thickness | 200 nm Au on 10 nm Ti substrate |

edge of the sensor is only connected to one electrode at a time, only one side is coated. The plating current is controlled by a galvanostat (Autolab PGSTAT204; Metrohm AG, Herisau, Switzerland), which keeps the current constant and adjust the voltage to maintain the current. As long as the pure gold surface of the sensor is present, the required voltage is increased by the potential difference of Sn and Au (see galvanic series[23]). Once tin is deposited on the gold surface, the voltage drops sharply. The deposition time and current determine the amount of tin atoms on the sensor respectively the thickness of the tin layer. After the deposition the sensor was rinsed with purified water and dried overnight.

Figure 3.8 shows images of an electroplated sensor surface. The images are taken using an optical microscope. At 40x magnification, a homogeneous surface morphology can be seen, which has a certain roughness. In the lower left corner of the first image there is an uncoated area. This can occur in case the corresponding surface was not sufficiently degreased and cleaned during electrode preparation. There is also a non-systematic distribution of micron sized grains across the surface. At higher magnifications (100x and 400x) it becomes visible that these are indeed not elevations but individual objects. Such structures have a significantly larger surface area than the rest of the planar surface, which means that an increased etching rate is to be assumed at these spots. Since the exact surface size cannot be determined with the available equipment and because these grains occur rarely, a homogeneous and uniform surface is still assumed.

3 Methods & Instrumentation

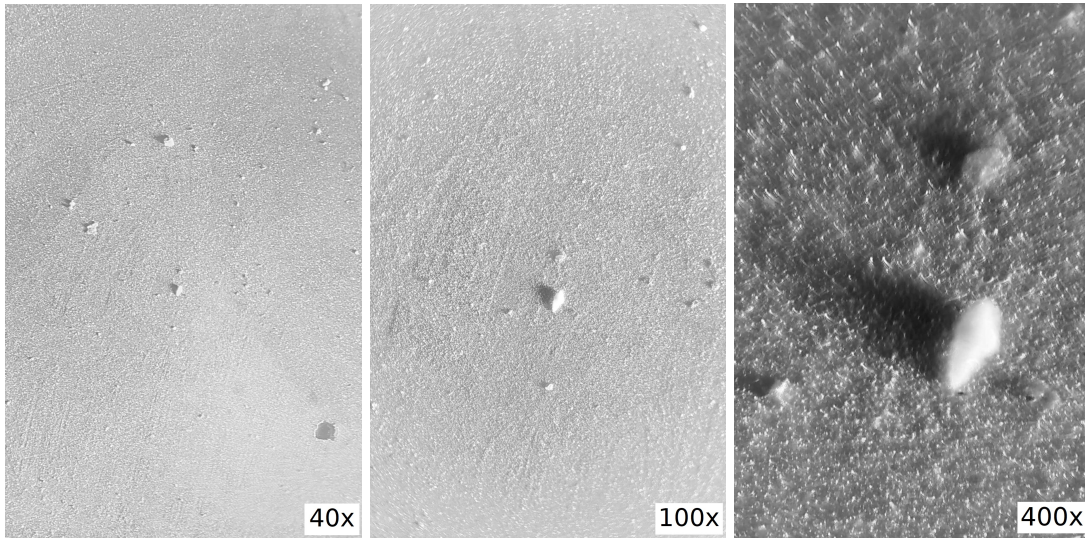


Figure 3.8: Images of electroplated sensor surfaces using an optical microscope.

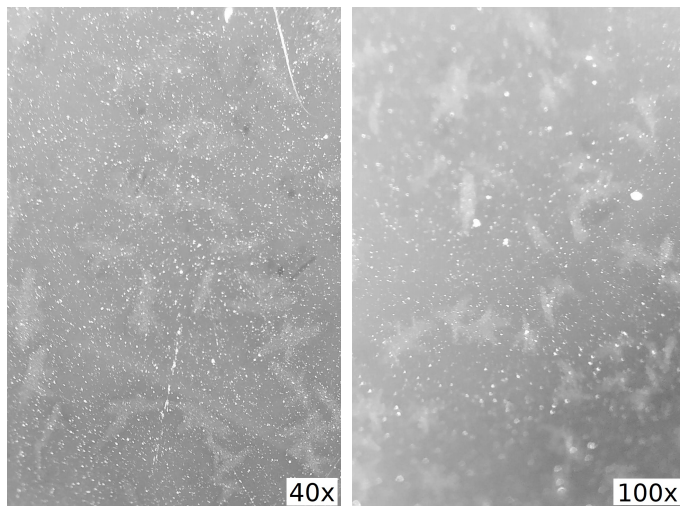


Figure 3.9: Images of PVD-coated sensor surfaces using an optical microscope.

For the PVD process, the sensor was placed in a custom holder with a mask. The mask covers the quartz surface so that only the gold electrode is exposed. The holder with the sensor was mounted in a PVD chamber, which was evacuated (approximately 1×10^{-7} mbar) before the evaporation of the tin. Once the calculated and weighed amount of tin has completely evaporated, the coating process is complete. The amount of deposited

3.5 Fourier-transform infrared spectrometer

tin is calculated from the amount of evaporated tin, the distance between the holder and the tin source and the target angle. With 21 mg of evaporated tin, this results in a calculated layer thickness of 10 nm.

The surface of the sensors coated in this manner (cf. fig. 3.9) shows a smooth and homogeneous tin film interspersed with micro-grains. At 100x magnification, some size distribution of the grains is observed, although the larger ones appeared infrequently. These grains are most likely formed by layer growth during the deposition process (cf. section 2.4.1.1). For tin growth on tin surfaces, the Volmer-Weber model[35] or rather the Stranski-Krastanow model[36] predominate, which predicts the formation of islands once a layer of tin has deposited. The grains on the sensor surface probably represent such islands.

3.5 Fourier-transform infrared spectrometer

A Nicolet iS5 FT-IR spectrometer (FTIR) (Thermo Fisher, Waltham, MA, USA) with an iD1 transmission attachment for gas phase analysis was used to identify the synthesized stannane and characterize the purity of the sample. The measuring chamber was evacuated several times and purged with dry nitrogen. The temperature-dependent vapor pressure of stannane was used to estimate a gas phase concentration that would allow the best possible measurement. By opening the valve between the measuring chamber and the cold trap filled with stannane, volatile stannane was transferred.

3.6 Laser systems

An NT340 optical parametric oscillator laser system (Ekspla, Vilnius, Lithuania) was selected for experimental studies using laser irradiation. In order to obtain the highest possible photon density, the fundamental wavelength of Nd:YAG Q-switched nanosecond pump laser was coupled out and guided by a mirror through quartz windows onto a corresponding target. The laser energy of the pump laser is 500 mJ at 1064 nm, the pulse repetition rate 10 Hz and the pulse duration 5 ns. The beam was not focused and had a beam divergence of <0.6 mrad and a irradiation area of approximately 0.7 cm².

3.7 Syntheses

3.7.1 Stannane synthesis

This section describes the synthesis of stannane (SnH_4) and initial analysis of the product. To our knowledge, there are only two peer reviewed publications [28, 83] with mass spectra of stannane, one of which shows only data of isotopically pure tin and the other the natural isotopic distribution[84]. After stannane synthesis a high-resolution 70 eV electron ionization mass spectrum was recorded and used as a reference for comparison studies. The main advantage of this approach is that the reference mass spectrum is acquired under identical conditions as the plasma-generated species, as the ion source of the mass spectrometer with all its operational parameters is expected to have a certain influence on the fragment distribution.

The synthesis recipe follows the prescription from Norman et al.[85] and is based on the reduction of tin(IV)-chloride (SnCl_4) using lithium aluminium hydride (LiAlH_4) under cryogenic conditions. However, partial steps of the synthesis process were modified. Particularly, solvents were used (as adapted from Elg et al.[46, 86]), which have more favorable properties for the synthesis due to their lower vapor pressure and thus less contamination of the product by solvents is expected.

The entire synthesis set-up is made of borosilicate glass and sealed via ground joints and halocarbon wax. A 250 ml three-necked round bottom flask was equipped with a magnetic stirring bar and connected via its glass joints to a dry ice condenser, and a rubber septum. The temperature in the reaction flask is measured with a thermometer. The apparatus is connected through two cold traps in series to a vacuum pump (1×10^{-2} mbar). The last cold trap was fitted with Teflon valves on both sides for the storage of the product. The entire system is evacuated and filled several times with dry nitrogen (N_2). The round bottom flask was loaded with lithium aluminium hydride (LiAlH_4 , 0.270 g, 7.115 mmol), 1,2-dimethoxyethan (DME, $\text{CH}_3\text{OCH}_2\text{CH}_2\text{OCH}_3$, 5 ml) and dibutyl ether ($[\text{CH}_3(\text{CH}_2)_3]_2\text{O}$, 5 ml). According to Elg et al.[86] this solvent mixture is more suitable than pure ether. The mixture was cooled to -196°C with liquid nitrogen, the condenser was filled with dry ice (-78.5°C), the first cold trap was cooled to -95°C with a toluene (C_7H_8) dry ice slush and the remaining last cold trap was cooled to -196°C with liquid nitrogen. Tin(IV)-chloride (SnCl_4 , 0.70 ml, 5.99 mmol) was added slowly to the bottom flask via a syringe through the septum of the flask. After the addition, the system was evacuated and then isolated from the vacuum pump via the Teflon valve and the reaction mixture in the flask was slowly warmed to about -20°C to allow the solvent to melt. Every 5 min to 10 min the Teflon

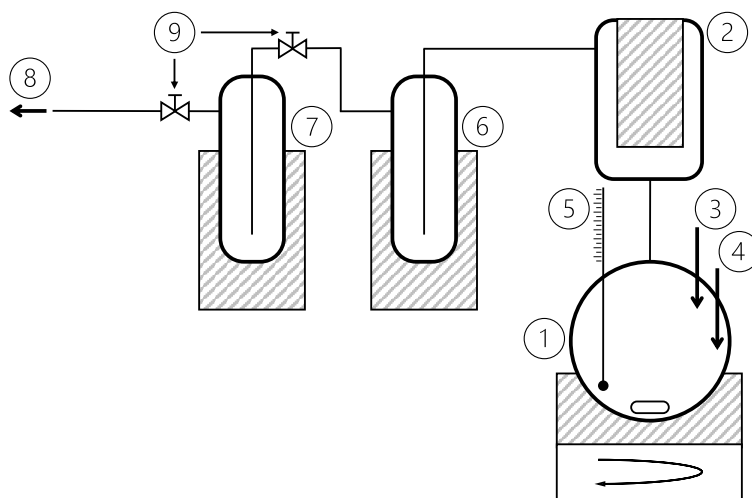


Figure 3.10: Schematic of the stannane synthesis apparatus. Components: ① 250 ml three-necked round bottom flask with a magnetic stir bar, ② dry ice condenser (-78.5°C), ③ rubber septum, ④ nitrogen (N_2) port, ⑤ thermometer, ⑥ cold trap #1 (-95°C), ⑦ cold trap #2 (-196°C), ⑧ vacuum pump with upstream cold trap (1×10^{-2} mbar), ⑨ Teflon valves.

valve to the vacuum pump was opened to remove the generated hydrogen gas (H_2). After 2 h the reaction was considered complete. The substance in the -95°C cold trap, mostly solvent, was discarded. The cold trap at -196°C containing the product was closed with both Teflon valves and stored in liquid nitrogen until used to avoid decomposition.

This synthesis route has the advantage that only the desired product (SnH_4) remains volatile and passes through the first two cold traps. Thus, in the last cold trap held at -196°C only the product is almost quantitatively collected.

As initial evidence of the presence of stannane, a trap presumably containing the product was heated with a heat gun until SnH_4 began to decompose into metallic tin on the glass surface inside the trap. The tin appears as a shiny silver reflective coating on the heated glass surface. When the stannane had completely decomposed, the trap was weighed. The tin was removed with diluted hydrochloric acid (HCl) and the trap again reweighed. Based on the mass difference and assuming that one SnH_4 molecule decomposes into one Sn atom, it is concluded that 0.286 mmol SnH_4 were synthesized (4.77 % yield). However, the

3 Methods & Instrumentation

yield varies considerably under the same synthesis conditions.

A direct chemical evidence of tin is provided by the *Leuchtprobe* test [87] (engl. luminous test) as an extremely sensitive and selective detection reaction for tin and qualitative verification of the successful synthesis. The test is based on the reduction reaction of tin (Sn) using nascent hydrogen. The dilute hydrochloric acid (HCl) with the dissolved tin was mixed with some grains of zinc (Zn) in an Erlenmeyer flask. The reaction of Zn with HCl produces hydrogen in *statu nascendi*, which is potent enough to completely reduce and hydrogenate the tin to stannane. A cold test glass was covered with the reaction solution and placed in the upper part of a non-luminous flame of a Bunsen burner. A bright blue fluorescent light is almost specific evidence for the presence of tin resulting from the decomposition of stannane, even at low concentrations.

3.7.2 Tin oxide synthesis

The synthesis of tin(IV)-oxide (SnO_2) is based on the approach of Yamazoe et al.[88]. Pre-cleaned metallic tin was treated with nitric acid (HNO_3) at approximately 70°C for 10 min. The product was then dried at 110°C for 24 h and calcined at 200°C to 300°C for several minutes. The dried powder was pressed to thin discs and stored under dry conditions.

3.8 Software

This chapter gives a brief overview of the data evaluation programs used in this thesis.

The general data analysis was done with Python 3[89]. NumPy[90], pandas[91] and Scipy[92] were used for data processing, and Matplotlib[93] for plotting. The analysis of the Tofwerk mass spectrometer data is carried out with the in-house custom software MassSpectre (written in Python 3), because it offers more and more adapted analysis possibilities than the control and analysis software of the manufacturer. In addition, the custom RASP (see section 3.8.1) developed in the work script is implemented in MassSpectre. This allows the analysis of superimposed signals directly in the software. The principles of RASP are explained in more detail in section 3.8.1.

3.8.1 RASP

RASP (**R**everse **A**nalysis of superimposed **S**ignal **P**atterns in mass spectra) is a custom Python 3 based script and is used to calculate the relative ratio of the presence of corresponding molecular species of the experimentally acquired mass signals. The operation

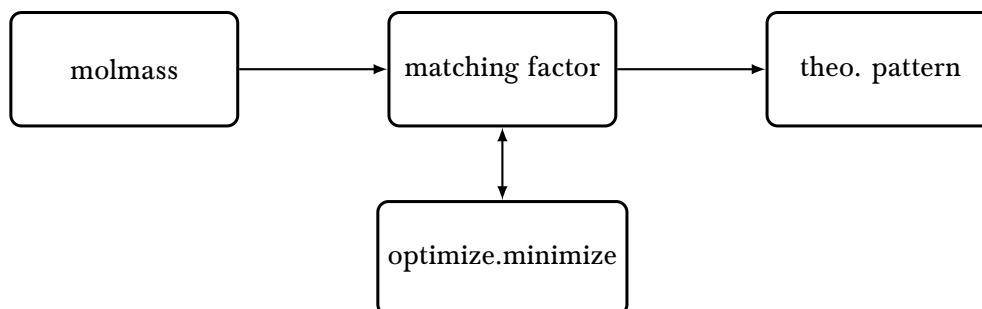


Figure 3.11: Core elements of RASP

of RASP is based on an algorithm that generates a theoretical mass spectrum of expected ions using the Python 3 library `molmass`[94] and adapting the ratios of these ions using the `scipy` library `optimize.minimize` with a Nelder-Mead algorithm[95] to achieve the highest congruence with experimental data, assuming natural isotope ratios[84]. Figure 3.11 depicts the inter-relation of the core modules of RASP. The `molmass` module is used to calculate the atomic or molecular mass (average, nominal and isotopic pure), elemental composition and a theoretical mass spectrum. The calculations are based on natural isotope ratios of the elements (unless explicitly stated) and do not take into account the mass deficit due to chemical bonding. In the case where superimposed molecule signals are considered, the individual mass spectra can be merged and the sum of all intensities per mass can be taken as the total signal. For better visualisation, the generated data can be plotted as a bar chart or, for better comparability with experimental mass spectra, a profile mass spectrum can also be generated from the data assuming a Gaussian shape. Both approaches are demonstrated for SnH_3 in fig. 3.12.

In order to obtain a numerical comparison value between the theoretical and the experimental mass spectrum, the method described in Moorthy et al.[96] is applied, where the so-called matching factor ξ is introduced. It takes values from 0 to 999, for historical reasons, and is rounded to the nearest integer. The higher the matching factor, the better the agreement between both mass spectra, whereby 999 is an perfect match. The underlying formula is as follows:

$$\xi = C \frac{\left(\sum_{i=1}^n (x[i])^{\frac{1}{2}} (y[i])^{\frac{1}{2}}\right)^2}{\sum_{i=1}^n x[i] \sum_{i=1}^n y[i]} \quad (3.1)$$

Where x is the value of one signal and y is the corresponding value of the other signal. In this case, the values of the theoretical and the experimental spectrum are applied. C is set

3 Methods & Instrumentation

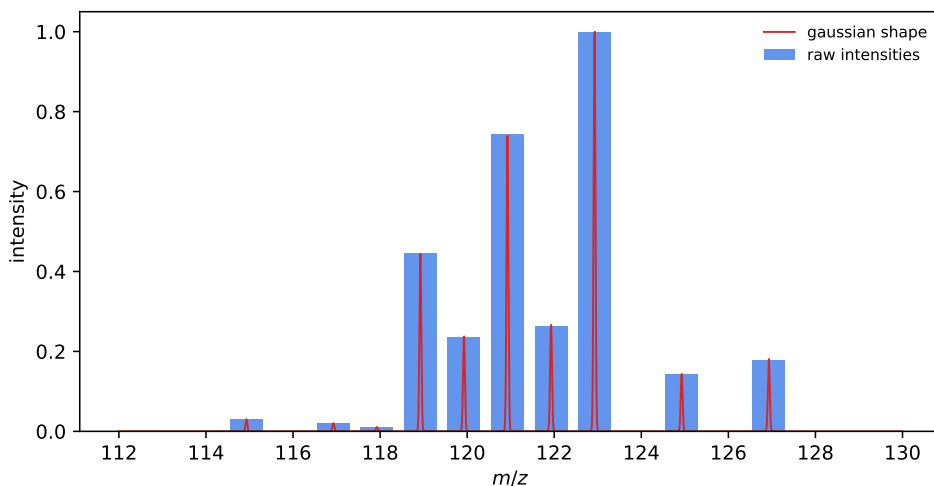


Figure 3.12: Calculated mass spectrum of SnH_3 via molmass.

equal to 999 and is only used for comparability. Differences of smaller signals are weighted stronger than differences in large signals. This is helpful with regard to mass spectra, since a lack of signals is an indication that it might not be the same analyte. Variations in abundant signals are mainly dependent on the conditions at which the ionization took place.

The entire mass spectrum is composed of superimposed individual theoretical mass spectra of the corresponding assumed species. Here the fractions of the individual mass spectra in the overall spectrum are the variables to be optimized. In the optimization process using the `optimize.minimize` library these variables are then varied using the Nelder-Mead approach until the mass spectrum generated with the weighting variables has the highest matching factor with the experimental mass spectrum. However, this results in a very flat maximum of ξ . However, this is problematic for the optimization, because near the maximum there is no sufficient numerical improvement and the algorithm does not find a concrete optimum. Therefore, a different formula for the matching factor was used for optimization. The sum of the squared differences of the values to be matched per m/z was used as the value to be optimized:

$$\xi_2 = \sum |x - y|^2 \quad (3.2)$$

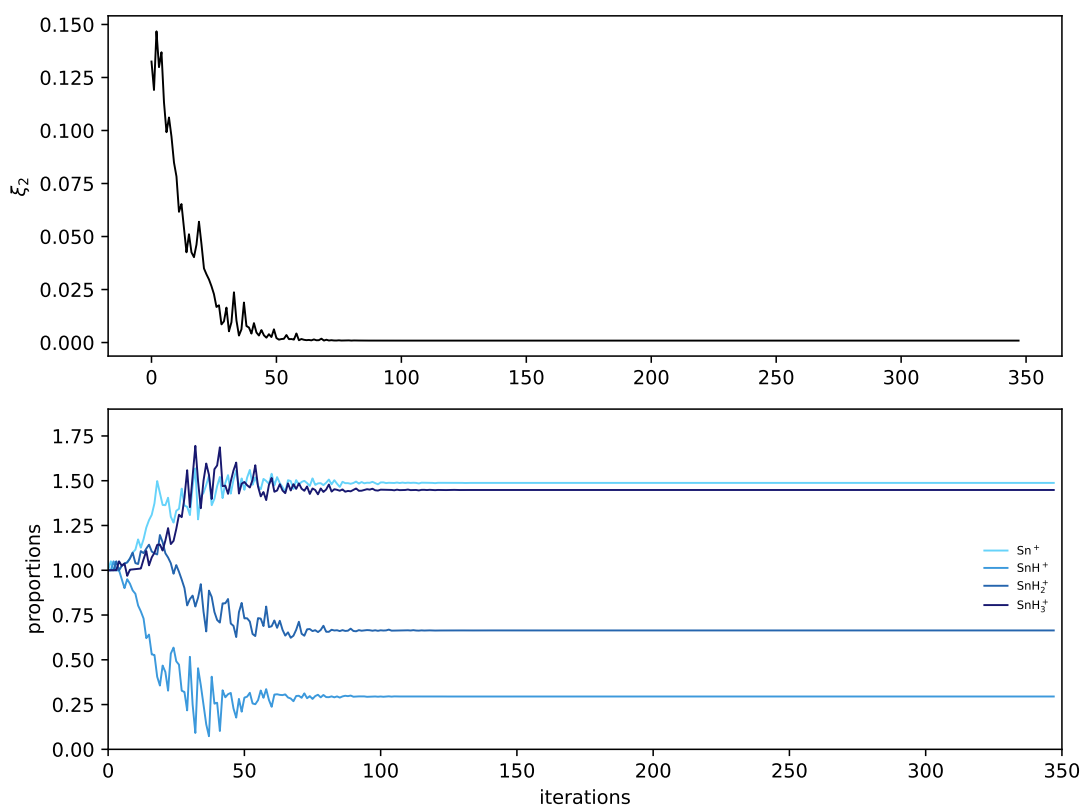


Figure 3.13: Progression of the minimize optimization with the Nelder-Mead algorithm approach. Top: calculated inconsistency per iteration. Bottom: calculated relative fractions of four variables per iteration.

Figure 3.13 shows the progress of the minimize optimization. ξ_2 is the factor at each iteration according to section 3.8.1, which becomes smaller the better the calculated mass spectrum matches the experimental mass spectrum. In addition, this figure illustrates the relative fractions of the (in this case) four variables that represent the four species (Sn^+ , SnH^+ , SnH_2^+ , SnH_3^+). According to the plot, the optimization is finished after about 100 iterations with minimum ξ_2 and constant fractions.

The matching factor of the optimized theoretical mass spectrum thus obtained with the experimental mass spectrum is then determined via the original formula (cf. eq. (3.1)) to preserve comparability. The process with the two different formulas is much more stable and yield results, which are much closer to the experimental spectrum. The optimized

3 Methods & Instrumentation

variables describe the fractions of the species to be optimized, which are then visualized as pie or donut charts. It should be noted that there is probably more than the one generated theoretical mass spectrum to describe the experimental mass spectrum equally well. Therefore, the distributions presented here should only be considered as one possible composition, which nevertheless provides conclusive results. Test runs of over 1000 repetitions, each with randomly generated initial values, always converged to identical results. This again underlines the stability of the evaluation method. Furthermore, for spectra of known composition, RASP provides exactly the correct composition.

3.8.2 DFT calculations

Density functional theory DFT calculations were carried out in close collaboration with colleagues in the relevant fields.

The calculations were done with the Gaussian16 software[97] package and the input was generated with GaussView6[98]. For this, self consistent field (SCF) calculations using the B3LYP functional [99, 100] provide an indication of the relative stability of various metal hydrides. This functional offers comparative results due to its high distribution and is also a reliable method when working with transition metal compounds [101]. On the basis of previous calculations and as a result of dissonance between calculation results and experimental results, two different basis sets were implemented: 3-21G (part of the Pople series of basis functions)[102] and DEF2-TZVPP (part of the Karlsruhe basis functions set)[103].

4 Results & Discussion

The aim of the present studies is to gain a fundamental understanding of the homogeneous and heterogeneous tin chemistry to enable and/or support model predictions about the processes occurring in complex systems in extreme ultraviolet lithography. This work is focused on the primary contaminant tin (Sn) and the corresponding hydride (SnH_4), respectively (cf. section 2.4.1). As a result, most of the studies are related to tin, but many observations and results can be transferred to other elements such as lead (Pb) or magnesium (Mg), which are described later in this chapter.

4.1 Synthesized stannane

A high-resolution reference mass spectrum of stannane is crucial for the investigation of the mechanisms leading to the formation of stannane and its subsequent decomposition into the elements using mass spectrometry. There are very little literature mass spectrometric data available, such as a mass spectrum of SnH_4 as reported by Saalfeld et al.[83]. However, it is limited to the isotopically pure $^{120}\text{SnH}_4$. This complicates comparative studies of plasma generated or synthesized SnH_4 and possible other Sn_xH_y species with natural isotopic distributions because of the number of stable tin isotopes. The mass spectrum published by Aaserud et al.[28] provides an important indication of comparability, but it is crucial to know the exact experimental conditions of the experiment as well as the instrument used in order to be able to make a meaningful comparison.

In order to obtain a high-resolution mass spectrum of stannane under known experimental conditions, stannane was synthesized and then investigated under identical conditions as the plasma-generated species. The synthesis was described in section 3.7.1.

4.1.1 Infrared spectrum of stannane

As an independent analytical method, gas phase infrared spectroscopy (instrument description in section 3.5) is useful to identify the synthesized product in the stannane synthesis and its purity from the resulting infrared (IR) spectrum. Figure 4.1 shows the recorded

4 Results & Discussion

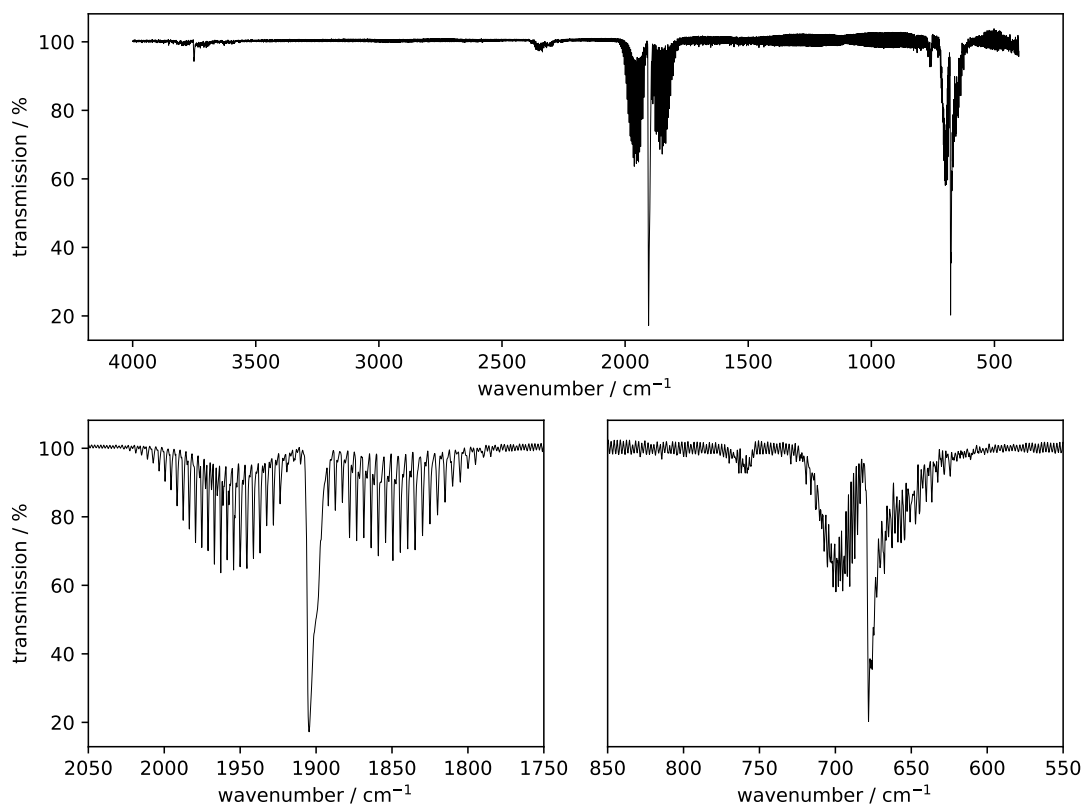


Figure 4.1: Gas-phase infrared spectrum of synthesized stannane.

infrared spectrum of the synthesized stannane and additionally the two characteristic regions. The characteristic P-, Q- and R-branches are clearly visible, as expected for this type of molecule. Due to the high resolution of the experimental spectra, the rovibronic transitions are well discernible and the individual signals are almost baseline separated. A direct comparison between the experimental IR spectrum and a literature IR spectrum from Levin et al.[26] reveals a high level of agreement. In general, the recorded IR spectrum is clean and nearly free of interfering signals. Because of the remarkably good agreement with the literature spectrum together with the luminous test (cf. section 3.7.1), it is highly likely that the product of the synthesis is indeed SnH_4 in high purity.

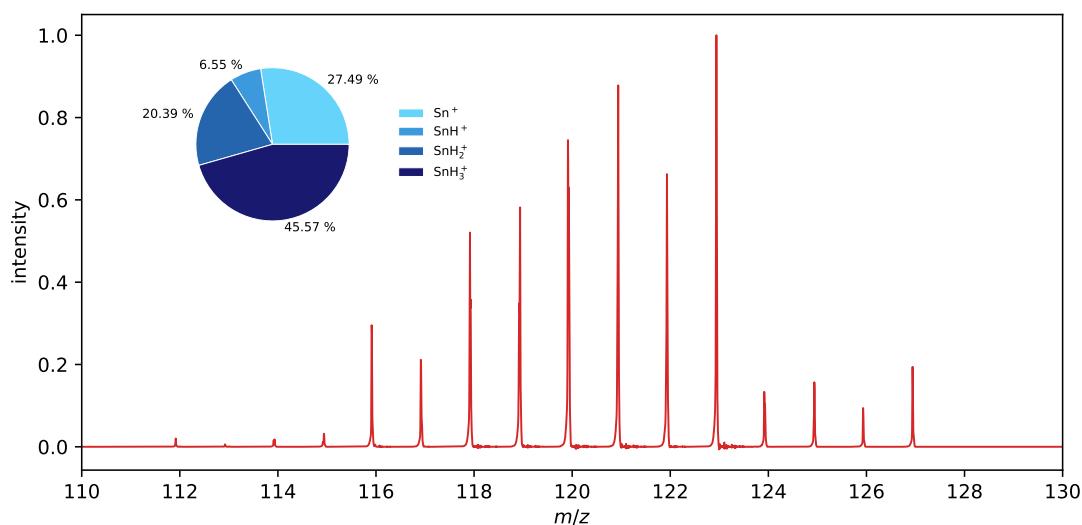


Figure 4.2: Mass spectrum of stannane (SnH₄); LTOF MS; EI at 70 eV; $\xi = 999$.

4.1.2 Mass spectrum of stannane

For the acquisition of a high-resolution reference mass spectrum of stannane, the LTOF instrument (section 3.3.2.1) is well suited due to its high mass resolution and the custom EI source, which has been characterized in detail. For this purpose, the cold trap containing synthesized stannane was connected to the plasma chamber (cf. section 3.2.1), which is in turn directly coupled to the LTOF. The cold trap was still held at 77 K with liquid nitrogen. At this temperature, the vapor pressure of stannane is very low, so that upon opening the valve only residual gas from the synthesis or sample transfer is pumped away. By removing the Dewar jar filled with liquid nitrogen, the trap is allowed to warm up slowly. The vapor pressure increases and stannane diffuses through the plasma chamber into the EI source of the LTOF. To minimize tin contamination as much as possible, the trap was immediately cooled down again with liquid nitrogen when the first tin hydride signals were detected in the mass spectrum. This prevents the partial pressure from becoming too high. Figure 4.2 shows the recorded 70 eV EI mass spectrum of the synthesized stannane. The signals of the mass spectrum are listed in table 4.1. The superimposed signal pattern ranges from m/z 112 to 127 and results from the SnH_x($x=0-3$) fragments (Sn⁺, SnH⁺, SnH₂⁺, SnH₃⁺) of the natural isotopic distribution of tin. Most likely, the fragments in the mass spectrum originate from initially ionized SnH₄ and subsequent fragmentation of the parent ion.

4 Results & Discussion

Table 4.1: Mass spectrum of stannane (SnH_4); LTOF MS; EI at 70 eV.

| m/z (nominal) | m/z (exact) | abundance / % |
|-----------------|---------------|---------------|
| 112 | 111.916 | 2.13 |
| 113 | 112.919 | 0.60 |
| 114 | 113.914 | 1.85 |
| 115 | 114.940 | 3.39 |
| 116 | 115.913 | 31.89 |
| 117 | 116.916 | 22.32 |
| 118 | 117.914 | 54.70 |
| 119 | 118.937 | 60.79 |
| 120 | 119.916 | 77.44 |
| 121 | 120.938 | 89.02 |
| 122 | 121.940 | 65.85 |
| 123 | 122.940 | 100.00 |
| 124 | 123.918 | 14.02 |
| 125 | 124.939 | 16.16 |
| 126 | 125.934 | 9.88 |
| 127 | 126.938 | 19.76 |

The mass difference between the ionic fragments with the same nominal mass is in most cases too small to separate them. In this way, the sum of the individual signals on the same mass is recorded. The composition of the experimental mass spectrum is determined from the given fragments using the RASP script (cf. section 3.8.1). RASP generates a theoretical mass spectrum and optimizes it until it matches the experimental mass spectrum. In the case of fig. 4.2 the agreement factor between the theoretical mass spectrum and the experimental mass spectrum is $\xi = 999$ and the distribution of the fragments is $\text{Sn}^+ / \text{SnH}^+ / \text{SnH}_2^+ / \text{SnH}_3^+ = 27.49 / 6.55 / 20.39 / 45.58$ %. The distribution determined by RASP is shown in the following graphs as a donut chart next to the corresponding mass spectra.

The measured mass spectrum of stannane using EI mainly consists of SnH_3^+ and smaller fractions of Sn^+ , SnH^+ and SnH_2^+ . Assuming that the measured ions result from fragmentation of SnH_4 during the EI processes, the fragment distribution is an indicator of the relative thermodynamic stability of the individual fragments under the prevailing conditions during ionization. However, the same analyte can result in a slightly different mass

Table 4.2: Comparison of the determined fractions of Sn^+ and SnH_3^+ .

| species | RASP / % | manual / % | Δ / % |
|------------------|----------|------------|--------------|
| Sn^+ | 27.49 | 26.12 | 5.2 |
| SnH_3^+ | 45.58 | 47.08 | 3.3 |

spectrum in different mass spectrometers or different ionization sources.

Caused by the high resolution of LTOF, some signals in the stannane mass spectrum consist of several partially superimposed signals. However, the resolution is not sufficiently high to distinguish the individual species in all these signals and even if individual signals are discernible, they are not baseline separated. Nevertheless, there are mass signals that can only originate from a single ionic species such as m/z 112, which can only originate from $^{112}\text{Sn}^+$ or m/z 127, which can only originate from $^{124}\text{SnH}_3^+$. However, the exact mass of the signals can be used to identify some of these species. Figure 4.3 shows all signals of the stannane mass spectrum with the assigned species. The presence of multiple signals per mass is most probably the reason why the exact mass of the detected peaks in table 4.1 alternates between the masses 0.916 ± 0.003 and 0.938 ± 0.004 whichever fragment is most prominent.

These data can now be used to validate the results of RASP. Since Sn^+ and SnH_3^+ are the dominant species in the signals, the calculation of the relative intensities of both species is a robust test case. Considering the signals that can only originate from one species, the resulting fractions of Sn^+ and SnH_3^+ are as listed in cf. table 4.2. The comparison between RASP and the manual calculation reveals an almost identical distribution with only small differences of 5.2% for Sn^+ and 3.3% for SnH_3^+ . As this reverse calculation approach is based on only partially visible signals and does not take all signals into account, minor errors are to be expected. However, the results clearly show that RASP results are a good representation of the actual distribution.

As already mentioned, according to an extensive literature survey, there are two publications in which stannane was investigated by mass spectrometry. The mass spectrum of stannane published by Aaserud et al.[28] is solely presented as a plot. Therefore, the

4 Results & Discussion

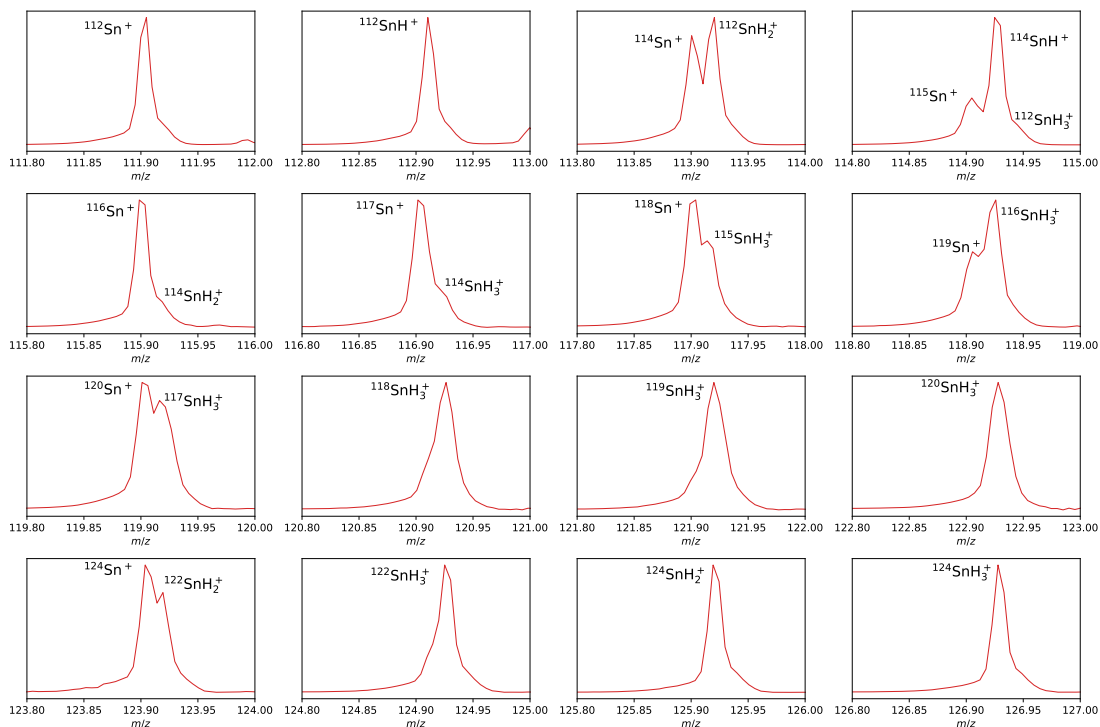


Figure 4.3: Individual signals of the stannane mass spectrum; LTOF MS; EI at 70 eV.

intensities of the mass signals had to be determined manually. Direct comparison of the stannane mass spectra between the LTOF and Aaserud yield a high matching factor of $\xi = 986$. The isotopically pure tabulated 70 eV EI mass spectrum of $^{120}\text{SnH}_4$ published by Saalfeld et al.[83] shows the fragment distribution directly, as there is no superposition of signals caused by isotopes. The data reveal that the fragmentation products of stannane are mainly Sn^+ , SnH^+ , SnH_2^+ , SnH_3^+ and spurious SnH_4^+ . For a direct comparison of the experimental mass spectrum recorded with the LTOF and the results of Saalfeld et al. the isotopically pure signals can be projected onto the natural isotope distribution by applying the relative ratio to each tin isotope. In this way, the relative relationship between the different fragments is maintained. Comparison between the TOF mass spectrum and the projected mass spectrum of Saalfeld's data reveals again a high matching factor of $\xi = 989$. These two high matching factors demonstrate the very good agreement of both literature mass spectra and the experimental mass spectra of the LTOF.

Table 4.3: Comparison of the determined proportions from the LTOF with the literature.

| species | LTOF abundance / % | Saalfeld abundance / % | Aaserud abundance / % |
|-------------------------------|-----------------------|---------------------------|--------------------------|
| Sn ⁺ | 27.49 | 28.72 | 25.47 |
| SnH ⁺ | 6.55 | 8.75 | 7.49 |
| SnH ₂ ⁺ | 20.39 | 21.81 | 23.05 |
| SnH ₃ ⁺ | 45.58 | 40.68 | 43.99 |
| SnH ₄ ⁺ | - | <0.04 | - |

Another method of comparison is to contrast the experimental fractions with calculated fractions of an mass spectrum. Therefore, instead of generating a mass spectrum for comparison from the isotopically pure fragment distribution of Saalfeld's results, the signal distribution is calculated from Aaserud's mass spectrum with the natural isotope distribution using RASP. The distributions are then compared. Table 4.3 contains the different abundances of the calculated distributions from the LTOF and the literature.

The comparison reveals a similar distribution of the fragments. There are some minor differences which do not affect the comparability. Only the presence of SnH₄⁺ in the distribution from Saalfeld et al. is remarkable, but the fraction is at least very small. The only possibility of detecting these species in a mass spectrum of stannane with the natural isotope distribution is at m/z 128, where only ¹²⁴SnH₄⁺ would be detected. However, there is no mass signal at this m/z -value. One possible explanation of this difference is that this signal is not SnH₄⁺ but the corresponding hydrogen isotope peak of the SnH₃⁺ fragment (SnH₂D⁺). The natural isotope abundance of deuterium (D, ²H) is 1.15×10^{-4} % [84] and since there are three molecular sites where the hydrogen can be replaced by deuterium in SnH₃⁺, the probability that one of them is D increases to 3.45×10^{-4} %. Thus, the theoretical relative abundance of SnH₂D⁺ would be 0.014 %. Although this is only about one third of the abundance reported by Saalfeld et al., this reasoning appears to be reasonable.

With regard to the results above, the universal applicability of RASP is demonstrated and it can thus be used to calculate the respective species distribution from superimposed mass spectra. The methods are applied to the analysis of the mass spectra of the samples and the results are presented next to the plot of the mass spectrum. Furthermore, the high-

4 Results & Discussion

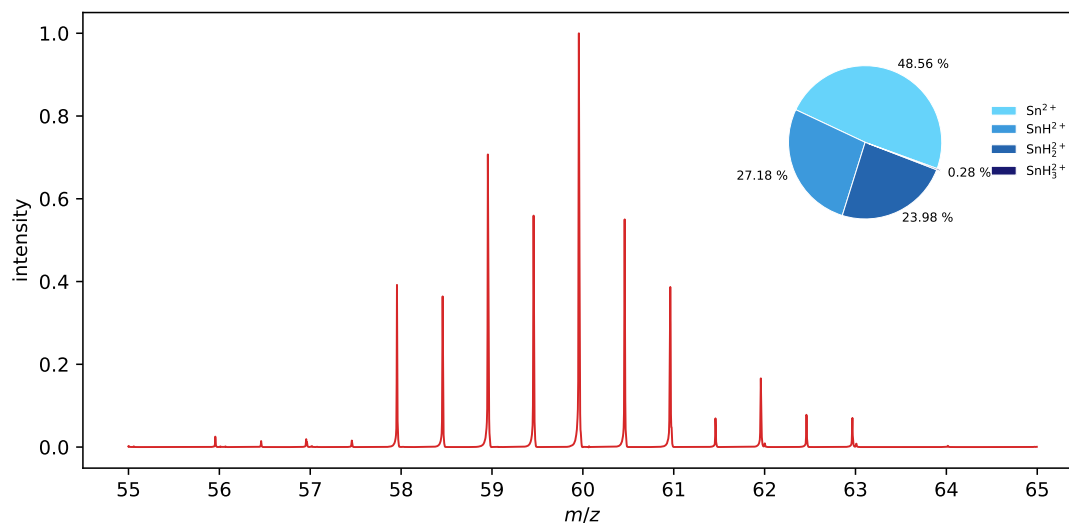


Figure 4.4: Mass spectrum of double charged stannane (SnH_x^{2+}); LTOF MS; EI at 70 eV; $\xi = 997$.

resolution mass spectrum of stannane agrees almost perfectly with the extracted mass spectra from the literature.

4.1.2.1 Doubly charged stannane and the stannane dimer

In the high-resolution EI mass spectra of synthesized stannane, in addition to singly charged stannane, there are also signals of doubly-charged stannane and the stannane dimer, as the following analysis demonstrates.

The mass spectrum of the doubly charged stannane (cf. fig. 4.4) with the formula (SnH_x^{2+}) ranges from m/z 56 to 63. Comparing the intensity of the largest signal of singly and doubly charged stannane ions, respectively, points out that the maximum signal intensity in this spectrum is only 8.1×10^{-2} % in the corresponding SnH_x^+ -spectrum. The fragment distribution calculated with RASP reveals a shift in the relative ratios compared to the singly charged stannane. While the singly charged stannane consists mainly of SnH_3^+ (45.58%), the mass spectrum of the doubly charged stannane has almost no SnH_3^+ signals (0.28%) but consists mainly of Sn^+ signals with 48.56%. In addition to the much lower signal intensity, this implies a much lower stability of multiply charged tin hydride ions and the quantitative fragmentation to the bare tin ion.

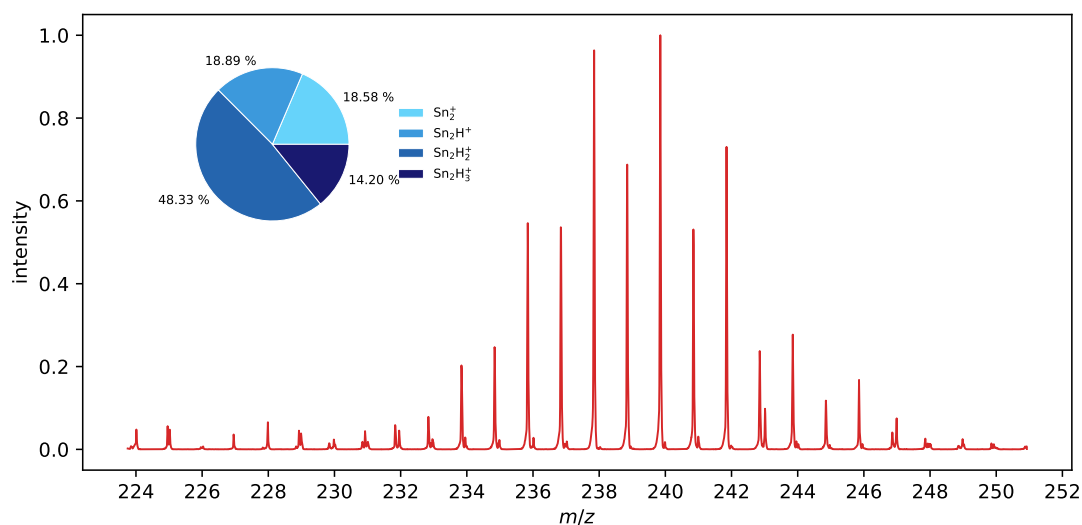


Figure 4.5: Mass spectrum of the stannane dimer (Sn_2H_x^+); LTOF MS; EI at 70 eV; $\xi = 989$.

The mass spectrum of the stannane dimer with the formula (Sn_2H_x^+) is displayed in fig. 4.5. The spectrum ranges from m/z 224 to 250 and the highest peak intensity is only $5.4 \times 10^{-4} \%$ as compared to the singly charged stannane. The distribution calculated by RASP reveals that the fragments consist mainly of Sn_2H_2^+ (48.33%), with the other species present in roughly equal lower fractions. This configuration appears to be more stable than other dimers. However, the low total intensity suggests a very low overall stability. In principle, the mass spectrum alone cannot be used to determine the spatial structure of the dimer. Nevertheless, due to the presence of $\text{Sn}_2^{(+)}$, it can be assumed that there is always an Sn–Sn bond located in the center of all dimer fragments and species. Due to the low signal intensity, debris signals from hydrocarbons (HC) are also visible in the spectrum. They often appear as apparent isotopic double peaks but can be identified by their exact mass. The doubled number of tin atoms per fragment renders the assignment of the different isotopic fragments more difficult. In such cases, RASP unfolds its full potential in almost unequivocally determining the fragment distributions.

4 Results & Discussion

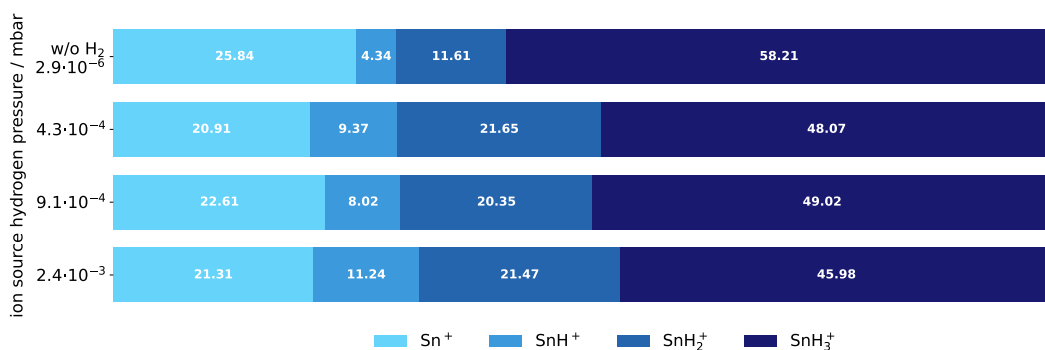


Figure 4.6: Effect of hydrogen gas pressure on stannane fragment distribution in an EI ion source. The pressure value refers to the ionizer region; proportions in percent; LTOF MS; EI at 70 eV.

4.1.2.2 Influences on stannane mass spectra

In order to understand whether the fragment distribution of stannane by EI is always the same or changes with certain experimental conditions, further studies were carried out to investigate the impact of the hydrogen pressure and the ion source temperature on the signal abundance in the corresponding mass spectra.

In the plasma chamber (PC), stannane is mixed with hydrogen prior to entry to the LTOF or the EI ion source. The hydrogen pressure in the chamber, and thus in the ion source, is adjusted using the gas handling manifold coupled to the PC and the butterfly valve of the turbomolecular pump. Figure 4.6 shows the calculated fragment distribution of stannane at different hydrogen pressures. The pressures refer to the recorded pressure in the ionization region of the LTOF. If no hydrogen is added the pressure in the ionizer is 2.9×10^{-6} mbar. The experiments with hydrogen were carried out at 4.3×10^{-4} , 9.1×10^{-4} and 2.4×10^{-3} mbar, respectively. There is clearly a change noted when hydrogen is present during the ionization process, but the actual pressure seems to play a very small role. On the one hand, there is elevated fragmentation in the presence of hydrogen, as there is less SnH_3^+ detected. On the other hand, there is a smaller amount of bare Sn^+ ions. Furthermore, SnH^+ and SnH_2^+ abundance are slightly larger in hydrogen presence. As mentioned in section 2.6.1.2, there is always chemical ionization occurring in an EI ion source at sufficiently high pressure. Depending on the matrix gas, the formation of $[\text{M}+\text{H}]^+$

observed. The smaller abundance of Sn^+ suggests that there is a gas phase reaction between high energetic hydrogen and the Sn^+ ions to the tin hydride ion. As long as the ions are in the ion source, there could be a statistical balance between ion fragmentation and bond formation.

It is well known that HC fragment patterns differ slightly at different ion source temperatures. When in contact with a heated surface, the analyte molecule gains energy and is more easily fragmented by EI. The experiments described here are intended to find out whether this also applies to stannane. Depending on the design of the ion source and the position of the filaments used, a constant temperature of the housing is achieved during operation under constant conditions. The ion source housing of the sector field mass spectrometer (cf. section 3.3.1) can be heated directly by heating cartridges. The cartridges can heat up to 646 K. However, the housing is already heated to 395 K by the operating filament alone. The temperature setting was increased stepwise until the entire casing had reached the new temperature setting. The cold trap containing stannane was connected to the CI port of the sector field mass spectrometer. By removing the cooling from the trap, the vapor pressure increases and stannane effuses into the ion source.

Figure 4.7 displays the calculated stannane fragment distribution at different housing temperatures. There is no change discernible upon increasing the temperature. The small variations indicate no trend but minor fluctuations, which may come from the time span between the additions and/or the manual addition of stannane itself. A possible reason for the lack of temperature dependence is that any ionized and then detected stannane molecule never hit the hot surface. The decomposition rate of stannane on metal surfaces is much higher than that of spontaneous decomposition and depends on to the surface temperature[24, 25]. In case a SnH_4 molecule hitting a hot surface, the decomposition into the elements is most likely to occur and it will not desorb back into the gas phase with additional energy, as HCs do. In high vacuum (about 1×10^{-6} mbar) in the ion source there is no other way to transfer the energy from a heated surface to the molecules inside the ion source because there are too few residual gas molecules (hydrogen, nitrogen, etc.) to carry and to pass on the additional energy. Furthermore, the transfer by thermal radiation is negligible. If these assumptions are correct, then it is not surprising that there is no effect of temperature on the fragmentation pattern, as the measured fragment ions are not affected by temperature. This aspect simplifies the measurement as the exact temperature of the ion source does not change the resulting stannane mass spectra.

4 Results & Discussion

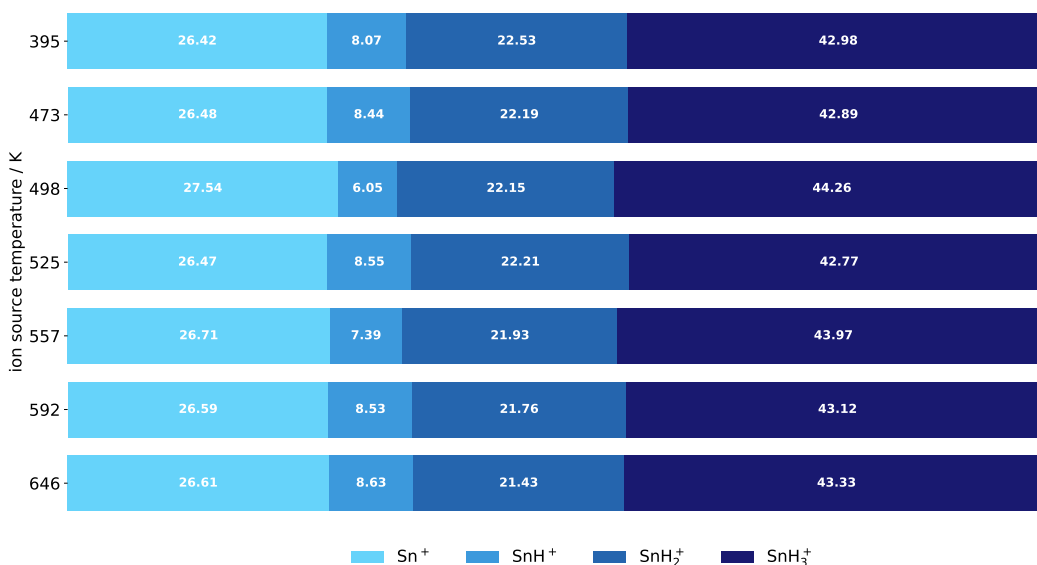


Figure 4.7: Effect of ion source temperature on stannane fragment distribution in a EI ion source; data in percent; SF MS; EI at 70 eV

4.2 Plasma-generated stannane

In an EUVL scanner, stannane is formed in the tin plasma chamber by the reaction of highly excited tin and hydrogen gas or hydrogen atoms. However, stannane can also be formed by the reaction of plasma-generated hydrogen species and metallic tin (cf. section 2.4.1.2). This method is much more feasible under laboratory conditions. This process is known as tin etching and is used in lithography applications to clean tin contaminated surfaces using excited hydrogen. This section covers the mass spectrometric investigation of the formation of stannane by a hydrogen plasma. Because of the different experimental setups, it is even possible to record neutral molecules and native plasma ions independently. Different plasma sources (cf. section 3.2) and mass spectrometers (cf. section 3.3) are used and their results are discussed.

4.2.1 Neutral tin hydrides

For the mass spectrometric investigation of neutral tin hydrides, the plasma chamber (cf. section 3.2.1) was connected to the LTOF (cf. section 3.3.2.1) via a CF40 line. A piece of previously cleaned metallic tin was placed in the plasma region of the plasma cham-

Table 4.4: Plasma chamber parameter for measurement of neutrals.

| Pressure and flow | |
|----------------------------|----------------------------|
| Gas flow (H ₂) | 10 sccm |
| Plasma chamber | 4.72×10^{-2} mbar |
| LTOF ionizer | 7.02×10^{-5} mbar |

ber and the chamber was purged and pumped out several times (achieved vacuum is 4.25×10^{-8} mbar). By adjusting the hydrogen flow via the gas handling manifold and the butterfly valve to the turbo-molecular pump, a constant pressure of 4.72×10^{-2} mbar was applied with simultaneous gas exchange within the plasma chamber. This minimizes contamination from the ambient air. To maintain a pressure gradient between the chamber and the LTOF, an orifice with a diameter of 2 mm was mounted in front of the ion source. This resulted in an ionization region pressure in the LTOF of 7.02×10^{-5} mbar. The flow rates and pressures applied are listed in table 4.4. The RF driver (cf. section 3.2.1) generated hydrogen plasma with 100 W power at minimal power reflection. The LTOF ion source in EI mode allows only neutral particles to enter the ion source while any positive ions are deflected.

Figure 4.8 shows the EI (70 eV) mass spectrum of plasma generated tin hydrides, which are assignable only by inspecting the exact mass, due to the small signals intensities and the relatively high HC background. The distinction between HC and tin is aided by the high resolution of the LTOF, as HC has an exact mass just above the integer m/z and tin has an exact mass just below it. The tin hydride signals are highlighted for clarity. The mass spectrum reaches from m/z 112 to 127; the signals between m/z 112 and 115 are difficult to distinguish from the background due to the low intensity. The determined fragment distribution with RASP reveals that the spectrum consists of Sn⁺ (32.11 %), SnH₂⁺ (19.59 %) and SnH₃⁺ (37.80 %) and to a minor extent of SnH⁺ (10.50 %).

Two conclusions are drawn upon spectrum inspections and the calculated distribution: Firstly, the signals are exactly located at the same m/z -values as the signals of the synthesized stannane (cf. fig. 4.2) and the overall agreement is very good. Secondly, the fragment distributions are almost identical, which can be explained by slightly different conditions in the ion source during ionization. In addition, in order to enter the ion source, the

4 Results & Discussion

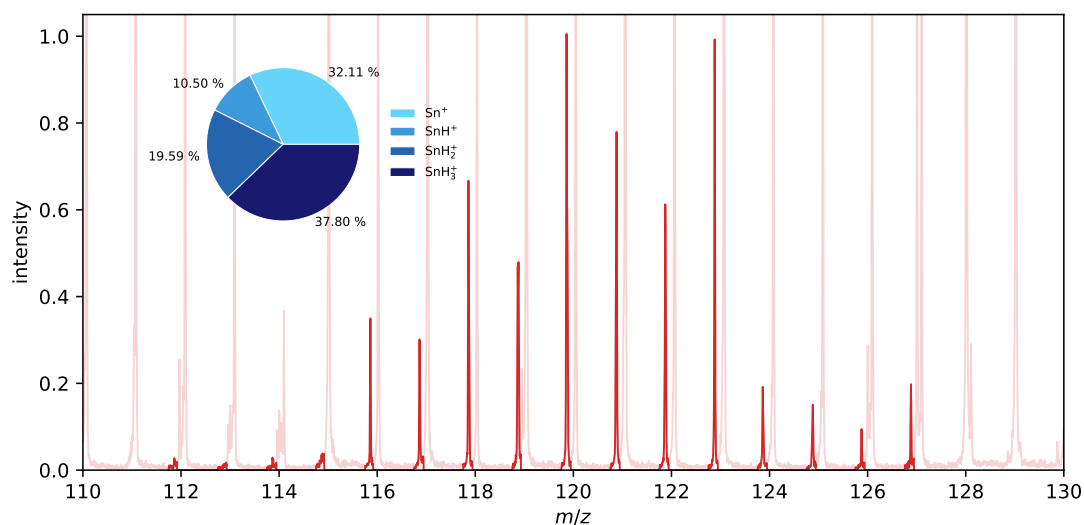


Figure 4.8: Mass spectrum of plasma generated stannane (SnH_x^+); LTOF MS; EI at 70 eV; $\xi = 996$.

molecule that has dissociated into the recorded fragment ions must be neutral. These are very strong indications that uncharged stannane is formed in the hydrogen plasma in the presence of solid tin, which then enters the LTOF via the transfer line and then fragments as the synthesized stannane does.

4.2.1.1 Doubly charged stannane and the stannane dimer

Analogous fragmentation behavior to the experiments with synthesized stannane is also evident in other parts of the mass spectrum. The signals of the doubly charged stannane fragments (SnH_x^{2+}) ranges from m/z 57 to 64. Due to the very low intensity of the signals, not all expected signals are visible. For better differentiation from the background, the tin hydride signals are again highlighted. The difficulty of the signals assignment is also represented by the matching factor of only $\xi = 828$. Unlike synthesized stannane (cf. fig. 4.4), the present mass spectrum consists almost exclusively of bare tin ion (Sn^{2+}) signals with 83.45 % abundance. This suggests that there are less favorable conditions for multiply charged tin hydrides in the plasma and the resulting dissociation to the doubly charged tin ion. However, in addition to the exact mass, the signals between the nominal masses (e.g. m/z 57.5) prove that the ions are doubly charged.

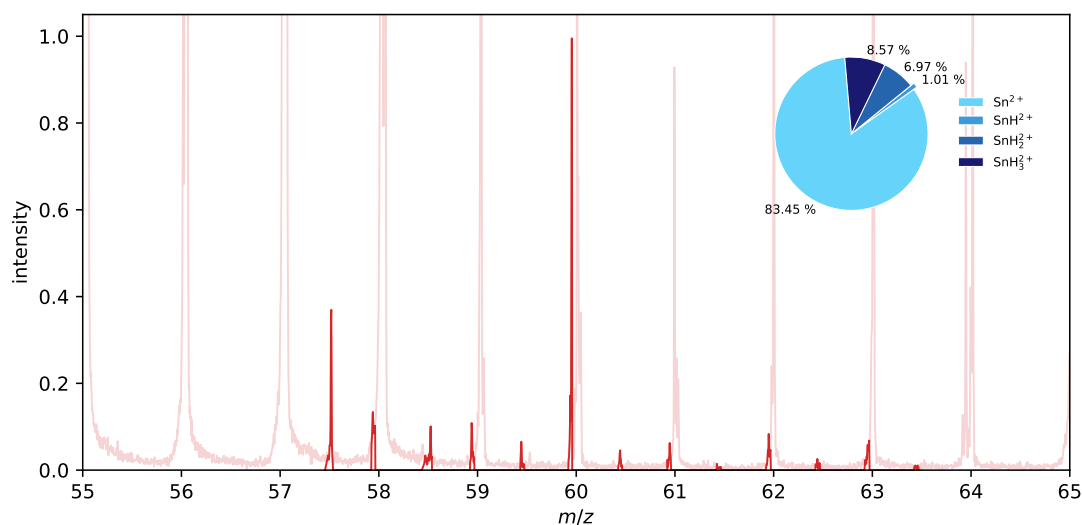


Figure 4.9: Mass spectrum of plasma generated double charged stannane (SnH_X^{2+}); LTOF MS; EI at 70 eV; $\xi = 828$.

The stannane dimer (Sn_2H_X^+) is not reliably qualifiable due to the very low signal intensities. Signals with exactly matching m/z values could indicate the presence of the dimer, but without being visible with a full isotopic pattern.

4.2.1.2 Oxygenated stannane

In the EI mass spectra of the plasma-generated species (cf. fig. 4.10), there are signals ranging from m/z 128 to 144 and they are again highlighted against the HC-background for clarity. These signals can be assigned to the type SnOH_X^+ . They are most likely oxygenated stannane fragments, although the molecular structure prior to fragmentation remains unclear. The distribution calculated with RASP reveals that it consists of SnO^+ (32.67%) and SnOH^+ (67.33%). The difficulty of the assignment of the smaller signals is also represented by the matching factor of only $\xi = 878$. However, it is not clear from the measurement whether the higher hydrides of the oxygenated species do not appear because the corresponding signals are too small to detect or too unstable under the conditions prevailing during EI ionization.

4 Results & Discussion

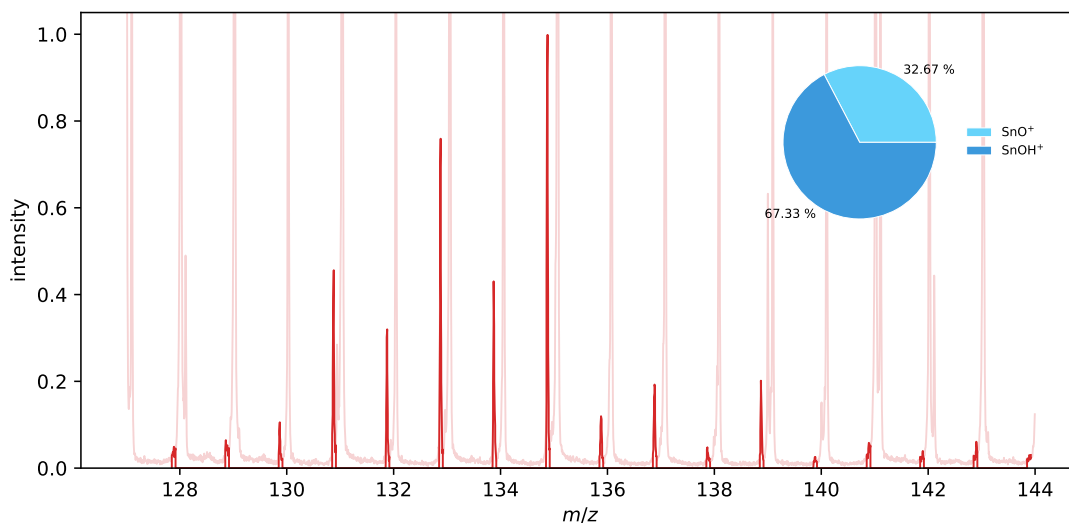


Figure 4.10: Mass spectrum of plasma generated oxygenated stannane (SnOH_x^+); LTOF MS; EI at 70 eV; $\xi = 878$.

It is pointed out that these species are not present in the mass spectra of synthesized stannane. This leads to several questions: (i) Are oxygenated stannanes formed in the plasma only? (ii) Is a gas phase reaction with oxygen species responsible for their formation? If so, why does the reaction not take place with the synthesized stannane? (iii) Is heterogeneous reaction system that only occurs on (tin) surfaces responsible for their formation? Later in this chapter, the origin and dependencies of the oxygenated species will be investigated and discussed in more detail.

4.2.1.3 Comparison of the different experimental set-ups

The availability of several mass spectrometers and plasma sources for the acquisition of plasma-generated stannane allows to make comparisons between the behavior of the different systems under nearly similar experimental conditions. In this way, the influence of each plasma and ion source parameter can be estimated. Due to their design, not every plasma source can be coupled to every mass spectrometer. The systems to be compared here are designed or modified in such a way that only neutral molecules and atoms can enter the ion sources and are ionized via EI; charged particles are actively reflected by corresponding potential settings. It is therefore reasonable to assume that the resulting mass spectra

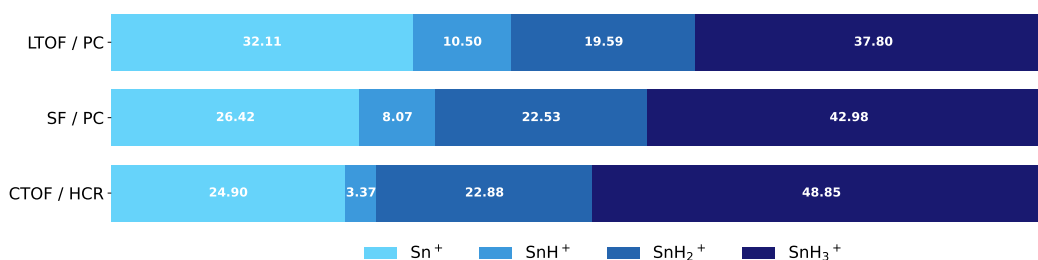


Figure 4.11: Comparison of fragment distributions recorded with different mass spectrometers and plasma sources. Ionization with EI at 70 eV.

solely originate from EI and subsequent fragmentation of stannane parent ion, in addition to other neutral gases present. Any variations of the recorded signal distributions are then only caused by the different EI sources. The differences are mainly the pressure prevailing during ionization (cf. fig. 4.6), the geometry of the source and the electron trajectories within the source.

Figure 4.11 compares the fragment distribution of the different set-ups (LTOF/PC, SF/PC and CTOF/HCR). Although there are some differences, the data shown exhibit similar patterns. The abundance of Sn⁺ is highest in the LTOF/PC system (32.11 %) and similar in SF/PC (26.42 %) and CTOF/HCR (24.90 %) setup. In general, the abundance of SnH₃⁺ behaves in a certain way inversely to the abundance of Sn⁺, while the abundance of SnH₂⁺ is almost identical. Accordingly, the fragmentation degree is higher for LTOF/PC than for SF/PC and lowest for CTOF/HCR. Overall, however, the three setups generate comparable signal distributions and point to stannane as the precursor molecule. The results show that depending on the discussed parameters during ionization, the mass spectrum of the same molecule can be slightly different, which is generally the case in mass spectrometry.

4.2.2 Ionic tin hydrides

In addition to the EI mode, the design of the LTOF's custom ion source also provides the transmission mode, which allows native (plasma generated) ions to be detected. The custom hexapole ion guide (cf. section 3.3.2.1) was mounted between the plasma chamber and the mass spectrometer to transfer ions from the plasma volume loss-free into the ion source. Table 4.5 compiles the parameters and settings of the plasma chamber and the transfer hexapole for the experiments to follow. As previously described, a constant pressure is applied within the plasma chamber by regulating the hydrogen flow by the mixing appa-

4 Results & Discussion

ratus and the butterfly valve to the turbo-molecular pump. An additional turbo-molecular pump is connected to the hexapole ion guide to reduce the pressure to minimize collision induced transformations or ion deflections.

Investigations of the ionic plasma components provide important information about the formation mechanism(s) of stannane. The major advantage of the transmission mode is that any detected signals must originate from ions generated within the plasma, since no further ionization takes place in the mass spectrometer. Consequently, the mass spectrum is much less congested as there are no signals from the LTOF background gas to interfere with.

The mass spectrum of the ionic tin hydride species is shown in fig. 4.12 and ranges from m/z 112 to 127, as expected for stannane. The distribution calculated with RASP indicates that the ionic fragments consist mainly of SnH_3^+ (72.39%). The high abundance of this species indicates an overall low fragmentation of neutral stannane in the hydrogen plasma and in the entire transfer. The transfer potentials are set as flat as possible to measure the fragment distribution in the plasma chamber with minimal collision induced fragmentation in the transfer ion optics. This mass spectrum confirms that ionic tin hydrides are formed in the presence of tin metal in hydrogen plasmas. However, no conclusions can be drawn from these results whether the ions are generated directly at the tin surface by interaction

Table 4.5: Gas flows and pressures within the plasma chamber/ LTOF system and electrical potentials of the hexapole ion guide for ion measurement.

| Pressure and flow | |
|------------------------------|----------------------------|
| Gas flow (H_2) | 20 sccm |
| Plasma chamber | 9.93×10^{-2} mbar |
| Hexapole transfer | 5.43×10^{-6} mbar |
| LTOF ionizer | 2.49×10^{-6} mbar |
| Hexapole transfer potentials | |
| Lens | -70 V |
| In | -30 V |
| Out | -50 V |
| RF | 300 V |

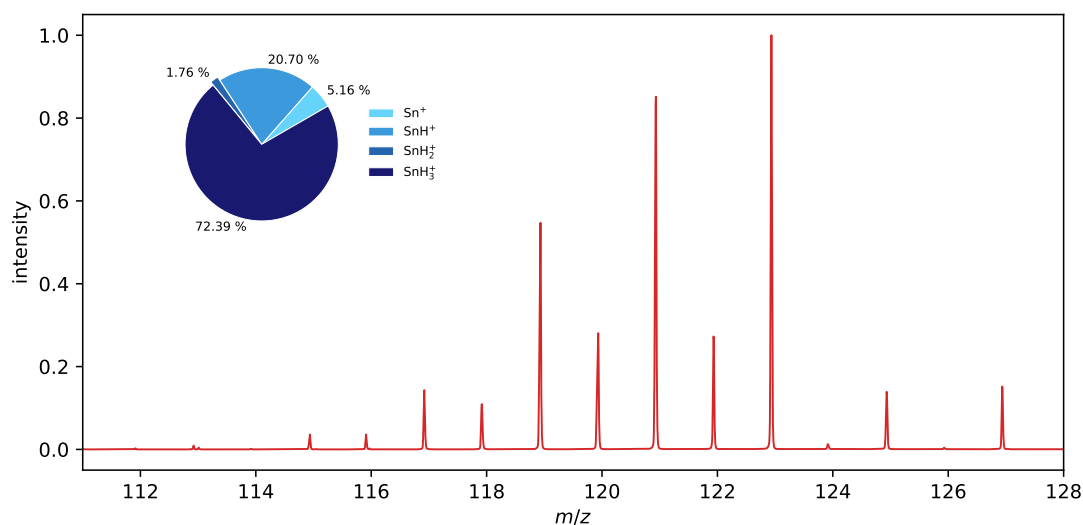


Figure 4.12: Mass spectrum of plasma generated stannane (SnH_X^+); LTOF MS; native ions; $\xi = 997$.

of high-energy hydrogen atoms or radicals with tin or by ionization and fragmentation of neutral stannane by fast electrons or ions in the plasma region. Direct comparison of the distribution of EI generated and native ion fragments from the plasma is thus not expected to yield relevant information. Therefore, only the native ions distribution and the ionic fragments distribution of neutral stannane generated with EI are compared.

4.2.2.1 Doubly charged stannane and the stannane dimer

Figure 4.13 presents the mass spectrum of the plasma generated stannane dimer (Sn_2H_X^+). It ranges from m/z 226 to 250, and the assignment is again based on the exact mass. According to RASP analysis, the mass spectrum consists mainly of the Sn_2H^+ fragment (66.56%) signals, meaning that the singly-hydrated Sn–Sn ion appears to be a thermodynamically stable compound in comparison to the other Sn species. The presence of two tin atoms increases the diversity of the isotopic patterns as compared to single tin fragments. These experiments clearly indicate that the corresponding stannane dimer ions are also formed in the plasma; either directly on the tin surface or in a subsequent gas-phase reaction.

4 Results & Discussion

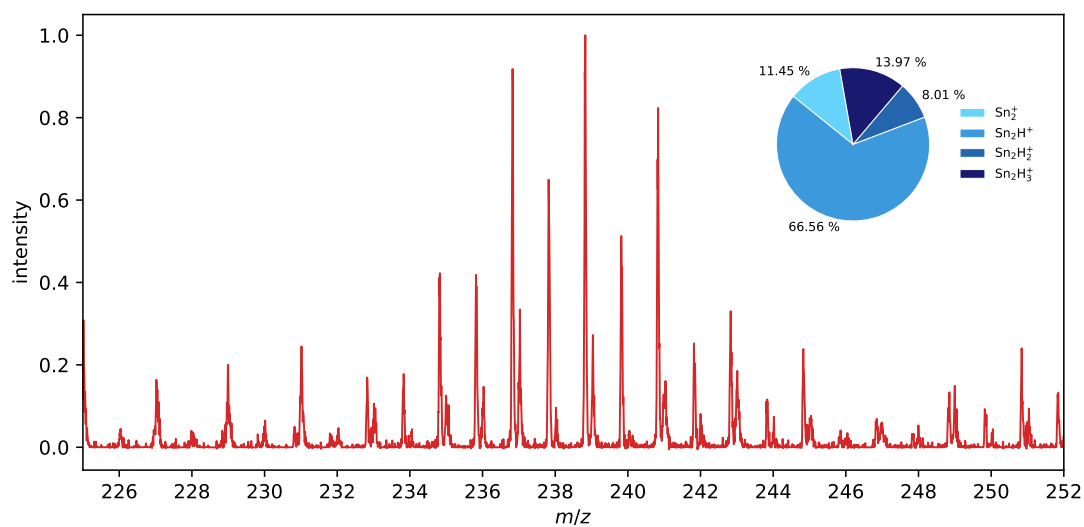


Figure 4.13: Mass spectrum of plasma generated stannane dimer (Sn_2H_X^+); LTOF MS; native ions; $\xi = 871$.

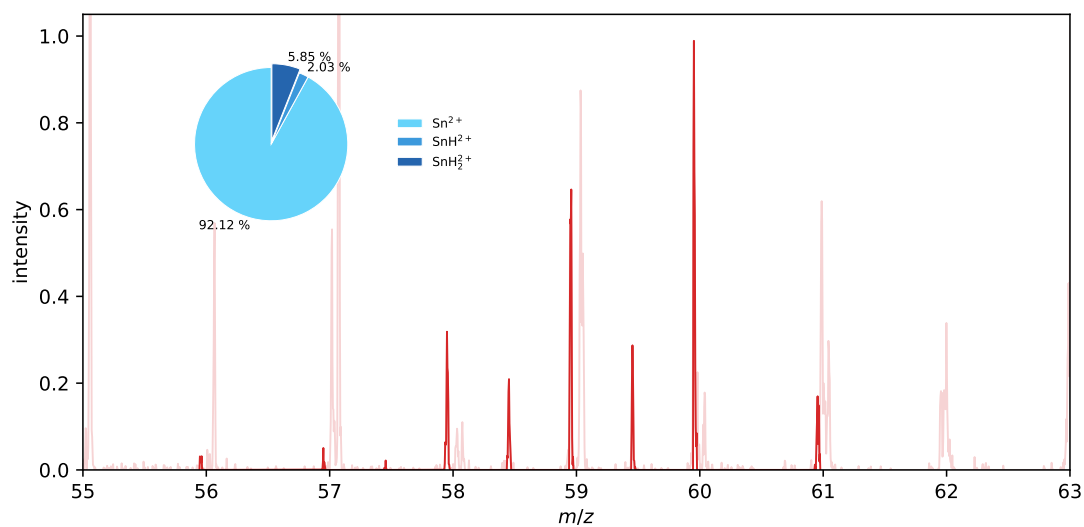


Figure 4.14: Mass spectrum of plasma generated double charged stannane (SnH_X^{2+}); LTOF MS; native ions; $\xi = 988$.

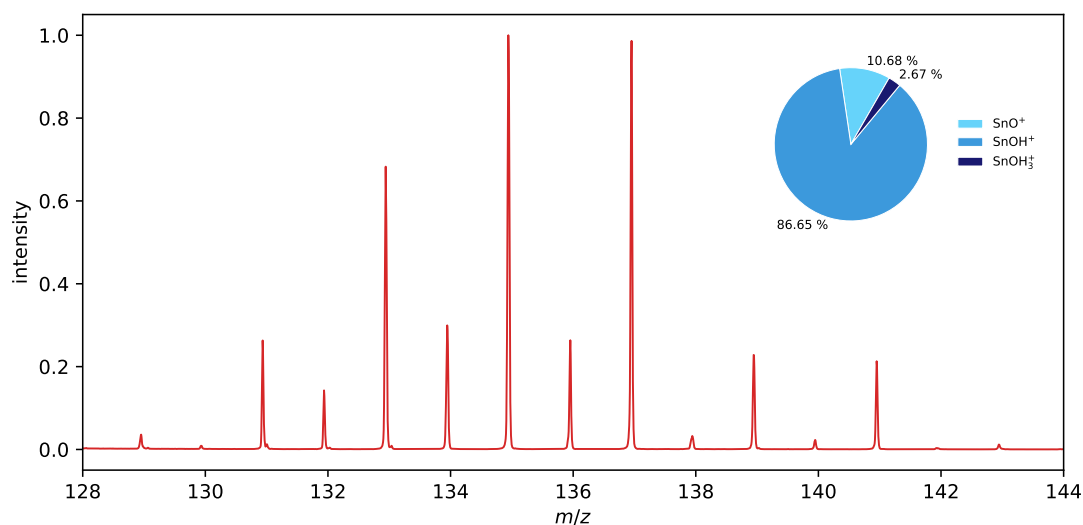


Figure 4.15: Mass spectrum of plasma generated oxygenated stannane (SnOH_x^+); LTOF MS; native ions; $\xi = 995$.

In the mass spectrum shown in fig. 4.14, the signals of the native doubly charged tin hydrides are in the range from m/z 56 to 61. Due to the low signal intensity, not all expected tin signals can be identified, the analysis is mainly based on the exact mass. The associated signals are highlighted for clarity. The fragment distribution determined by RASP shows that the mass spectrum consists almost entirely of Sn^{2+} (92.12%). This suggests that the corresponding hydrides are not stable under plasma conditions and that the electrons and ions accelerated in the RF field of the plasma cause tin to become doubly charged.

4.2.2.2 Oxygenated stannane

As in the plasma-generated neutrals mass spectrum (cf. fig. 4.10), the oxygenated stannane species are detected as native ions in the mass spectrum in fig. 4.15. The signals range from m/z 128 to 143 and exhibit almost exclusively SnOH^+ (86.65%). As with the neutral oxygenated stannane species, no statement can be made about their origin. Either it forms as stannane on tin surfaces or in a subsequent gas-phase reaction in the plasma volume. However, these species are both generated as neutrals and ion by the hydrogen plasma and thus most likely have the same origin.

4.2.2.3 Experimental settings affecting mass spectra

The experimental parameter space for the acquisition of native ion mass spectra becomes increasingly complex, as the instruments provides multiple ion optical settings. Generally, the lens potentials of the LTOF ion optics are tuned to provide the highest signal intensity at the highest resolution. In additions, the settings (c_tune and c_load) of the RF generator matching network are optimized to the lowest RF loss.

The variation of the output power of the RF generator is directly affecting the hydrogen plasma induced chemistry. The power can be adjusted from 0 W to 100 W in incremental steps via the serial interface of the generator. Figure 4.16 shows the dependence of the signal intensity of the extracted ion current (EIC) of SnH_X^+ and SnOH_X^+ on the plasma power and additionally the abundance ratio of these species obtained with a linear fitting function. In the upper part of the figure, it can be seen that the intensity of the signals is not linear but proportional to the power of the RF generator. The experiment was carried with random settings of the RF power. The higher the power is applied to the electrode inside the plasma chamber, the higher the degree of ionization in the gas volume and the more reactive species are formed. As a result, more stannane is produced, clearly discernible in the mass spectra. The signal intensity of SnH_X^+ increases from 8.81 cps at 10 W to 382.91 cps at 100 W and the intensity of SnOH_X^+ increases from 1.38 cps to 31.10 cps. A non-linear increase of the stannane signals with increasing RF power is observed. The bottom plot in fig. 4.16 shows the ratio between the signal intensities of SnH_X^+ and SnOH_X^+ at different RF power settings. A linear correlation between the intensities is observed with a slope of $m = 0.0817 \pm 0.0021$. Accordingly, the signal intensity of SnOH_X^+ is always approximately 8.2% of the signal intensity of SnH_X^+ , independent of the RF power. Based on the fact that tin hydride formation is observed even at very low RF powers, it can be assumed that there is no threshold for plasma-induced stannane formation. If this were not the case, the formation would only take place above a certain RF power, and only at that point would it become detectable. Whenever reactive hydrogen atoms are generated by the plasma, a reaction with tin occurs on the surface. The same behaviour also applies to SnOH_X^+ . This suggest that all stannane species (SnH_X^+ , SnH_X^{2+} , Sn_2H_X^+ , SnOH_X^+ , etc.) form within the same reaction mechanism or originate from the same precursor molecule. Since the highest signal intensity is obtained at maximum power, all experiments are performed at 100 W to achieve the highest possible signal-to-noise ratio. This makes is easier to identify the corresponding signals in the mass spectrum and the analysis with RASP.

Gas pressure, and therefore gas density, significantly affects the plasma dynamics. Very

4.2 Plasma-generated stannane

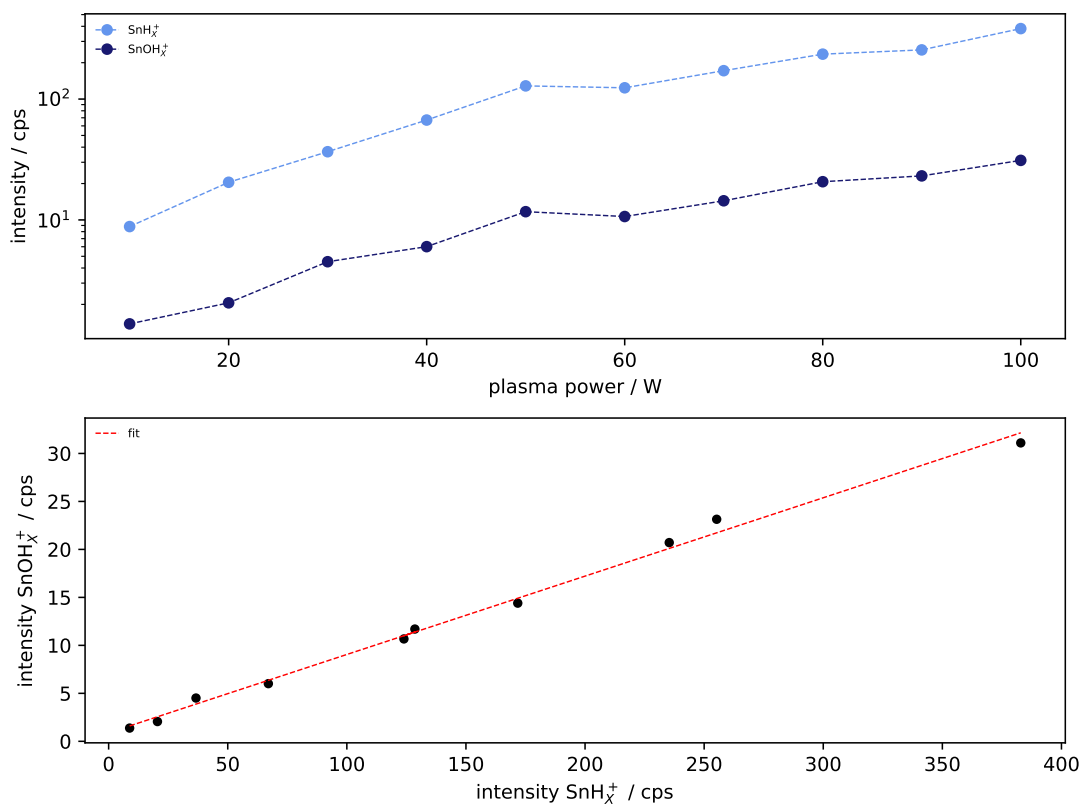


Figure 4.16: Top: dependency of the EIC of SnH_x^+ and SnOH_x^+ at different plasma power. Bottom: ratio of SnH_x^+ and SnOH_x^+ with linear fitting; 6.50×10^{-2} mbar hydrogen pressure; LTOF MS; ion.

low pressures renders plasma ignition and self-sustaining reactions difficult or impossible, since the number of collisions is directly related to the pressure. Too high pressures also have a negative effect on the plasma, as the mean free path decreases and eventually becomes so short that the electrons and ions in the plasma region are unable to build up enough energy in the RF field to ionize further atoms and molecules. The etch rate of tin and thus the amount of formed stannane is directly related to the amount of reactive plasma species. Figure 4.17 portrays the results of the investigation of the influence of pressure on the fragment ion distribution of tin hydrides as calculated with RASP (left) and the total amount of tin species present (right).

The hydrogen pressure was varied from 2.27×10^{-2} mbar to 1.00×10^{-1} mbar. After each

4 Results & Discussion

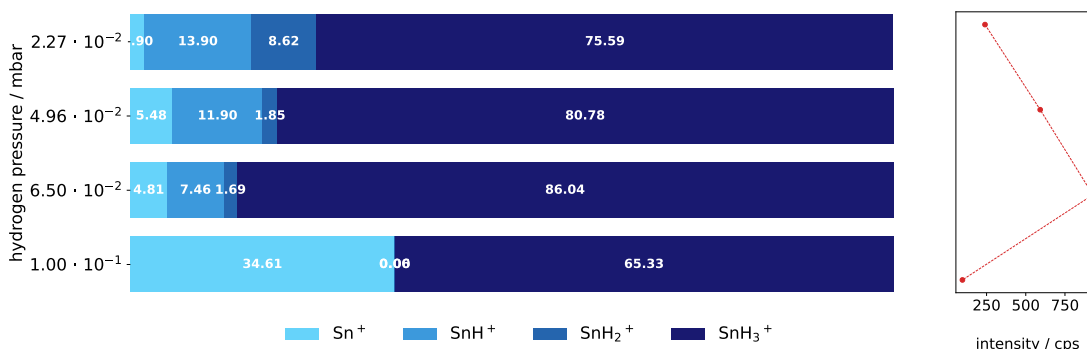


Figure 4.17: Effect of hydrogen plasma pressure on stannane fragment distribution and the signal intensity; LTOF MS, native ions.

pressure change, 15 min settling time ensured that the system was equilibrated again. There are two different trends in the fragment ion distribution with pressure changes. During the initial increase of hydrogen pressure, there is an increase of SnH_3^+ signals and a simultaneous decrease of Sn^+ , SnH^+ and SnH_2^+ signals. This trend shows a maximum at 6.50×10^{-2} mbar. With further increasing the pressure, the second trend becomes apparent and the ion signal distribution changes massively: The abundance of Sn^+ is significantly increased at the expense of the abundance of SnH_3^+ ; SnH^+ and SnH_2^+ are virtually absent. These two trends are also visible in the total intensity of the tin hydride signals (cf. fig. 4.17). When the hydrogen pressure is increased from 2.27×10^{-2} mbar to 6.50×10^{-2} mbar, the total amount of tin species increases proportionally. As the pressure reaches 1.00×10^{-1} mbar, the intensity drops drastically. The dependence of the intensity on the pressure is expressed by two convoluted functions, as can be inferred from the two opposing trends. On the one hand, the more hydrogen molecules per volume are present in the plasma, the more reactive hydrogen is formed, which eventually generates stannane. On the other hand, the mean free path decreases with increasing pressure. This means that less reactive hydrogen can be generated and, more importantly, diffusion to the tin surface and from the surface to the mass spectrometer is hindered. Due to the higher number of available reactive hydrogen radicals, the formation of SnH_3^+ becomes favorable, which is one reason why its abundance increases with increasing hydrogen pressure. At higher pressures, however, there are significantly more collisions, resulting in increased dissociative fragmentation. This is indicated by the shift in the signal abundances towards bare Sn^+ .

4.2 Plasma-generated stannane

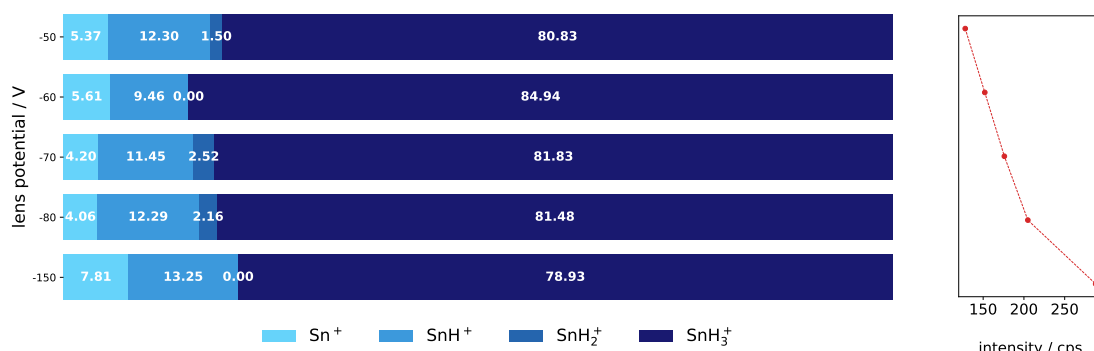


Figure 4.18: Effect of the lens potential of the hexapole ion guide on stannane fragment distribution and the signal intensity; hex-in: -30 V, hex-out: -50 V, RF: 300 V; LTOF MS, native ions.

The hexapole ion guide, its geometry and functionality are described in detail in section 3.3.2.1. The influence of the entrance lens potential and the DC ramp of the hexapole on the stannane signal abundance in the mass spectrum has been studied experimentally. Figure 4.18 provides the results of the lens potential variation, which was varied between -50 V to -150 V. The DC ramp of the ion guide remains constant. On the left of fig. 4.18 the fragment distribution of the different mass spectra as calculated by RASP is shown, and on the right the total signal intensities are plotted. As the lens potential changes, the total signal intensity behaves as expected: The higher the lens potential, the higher the intensity. An almost linear trend is observed. The attractive field generated by the lens potential reaches further into the plasma volume at higher potentials and thus attracts more ions. However, the effect on the overall transfer should not be ignored. As the lens potential varies, the focusing properties of the lens change as well. This also changes the kinetic energy of the ions entering the hexapole ion guide, which affects the ion transfer efficiency of the guide. The results suggests that there are only minimal shifts in the fragment distribution at different lens potentials. Only in the extreme case of -150 V lens voltage a slightly increased fragmentation is noted as inferred by elevated abundance of Sn^+ and the (marginal) decrease of the SnH_3^+ signal. Overall, the effect of the lens potential is negligible and only affects the total intensity as more ions are captured.

To efficiently transfer ions along the ion guide, a gradual DC ramp potential is applied

4 Results & Discussion



Figure 4.19: Effect of the ramp gradient of the hexapole ion guide on stannane fragment distribution and the signal intensity; hex-out: -50 V, RF: 300 V; LTOF MS, native ions.

between the hexapole entrance and exit. The higher the potential, the higher the ion acceleration within the hexapole. For the variation of the DC ramp within the hexapole, the potential difference between the lens and the hexapole entrance remains identical. Figure 4.19 presents the impact of the variation of the DC ramp potential on the recorded ion distribution. The shown potential is the difference between entrance and exit of the hexapole. In this case, the exit potential remains fixed at -50 V. The ramp was varied between 0 V to -40 V; a ramp of 0 V means no additional driving force for ions within the guide.

Even with a DC ramp of 0 V, relatively high EICs are recorded. The potential difference between the lens and the hexapole entrance held at -40 V is still adequate to sufficiently accelerate the ions into the hexapole ion guide. By increasing the ramp, the signal intensity increases; at -20 V ramp potential a maximum is reached. Between 0 V to -20 V ramp potential the distribution shifts to SnH_3^+ by simultaneously decreasing the abundance of Sn^+ and SnH^+ . With steeper ramps (-30 V to -40 V) a signal decrease of the EIC and an inverse shift in the distribution is observed. As a result, fewer native ions follow a stable trajectory through the ion guide transfer stage, leading to lower signal intensities. It also appears that there is an increase in fragmentation towards the smaller tin hydrides. In addition, the simultaneous change of the lens potential results in a different attraction force on the ions. The recorded signal intensity is thus a function of the lens potential and the ramp gradient.

4.2.2.4 Comparison of the different experimental set-ups

A comparison of the distributions of the plasma-generated native ions can be made in the same way as for the EI mass spectra of the neutral stannane (cf. section 4.2.1.3). Not only do the ion sources affect the fragmentation of stannane and thus the signal distribution, but also the plasma source, the hydrogen pressure in the chamber and the transfer stage, as well as the potentials of the ion guide transfer.

Figure 4.20 shows the calculated fragment distributions of the native ions measurement with the LTOF/PC system and the CTOF/HCR system. In contrast to the similar signal distribution obtained for neutral stannane, a completely different situation emerges here. The distribution recorded with the LTOF/PC set-up reveals that it mainly consists of SnH_3^+ (72.39 %) and only to a small extent of Sn^+ (5.16 %). Mass spectra recorded with the CTOF/HCR system consist to a large extent of Sn^+ (59.42 %) and SnH^+ (36.36 %). SnH_3^+ is barely present with 3.10 % abundance. The primary product of the reaction between reactive hydrogen species and tin is most likely neutral stannane. Ionization and fragmentation occur by a subsequent interaction with the accelerated electrons and ions in the plasma region. Accordingly, stannane undergoes a significantly higher degree of fragmentation in the CTOF/HCR setup. The plasma source is the main difference between the two systems. Due to the large volume of the PC there is virtually no gas flow and a homogeneous pressure can be assumed inside the chamber. Due to the time it takes for the initially generated ions to reach the entrance of the transfer stage, thermodynamic control of the ion distribution is most likely. Unlike the CTOF/HCR set-up, there is a flow of hydrogen gas through the glass tube with a pressure gradient along the tube. In addition, the lower power output of the HCR RF driver generally requires a higher pressure than the driver employed in the PC. Moreover, the plasma torch of the HCR is much more inhomogeneous than the bulk plasma in the PC and because of the higher surface-to-volume ratio within the tube, the plasma sheath occupies a proportionally larger space. As the borosilicate glass tube has little or no electrical conductivity, high wall potentials build up on the surface, extending into the plasma volume and interacting with the ions and electrons. The combination of higher pressure and the harsher conditions is most likely responsible for the higher degree of fragmentation. The electrostatic optics of the CTOF should not have a significant impact on the degree of fragmentation. The fragment distribution of the native ions is therefore an indicator of the conditions under which the native ions are formed and of the nature of the travel path to detection.

4 Results & Discussion

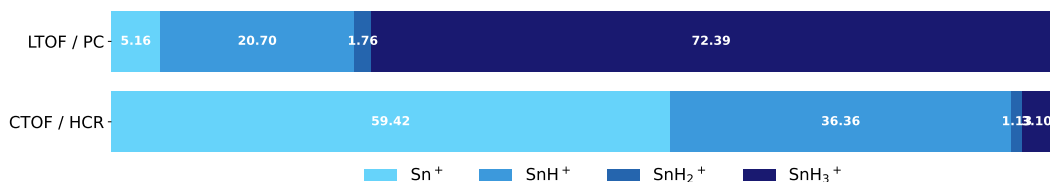


Figure 4.20: Comparison of fragment distributions at different mass spectrometers and plasma sources.

4.2.3 Tin deuterides

Deuterium (D_2 ; 2H_2) has chemical and physical properties which are almost identical to hydrogen (H_2). When D_2 is added to the plasma chamber (PC) replacing H_2 , a deuterium plasma is formed whose reactive species can naturally undergo the exact same reactions as hydrogen. Accordingly, it is to be expected that all plasma-generated products will contain D instead of H.

Figure 4.21 depicts the fragment signal distributions of the deuterium plasma generated stannane species calculated with RASP. During the experiment, the LTOF ion source was switched between the EI and transmission mode in order to detect neutral and ionic species. The distribution shown in fig. 4.21a reflects the expected fragment distribution for EI ionization. However, for attaining the highest matching factor, the inclusion of the hydrogen species is mandatory. The tin hydride fragments follow the similar relative distribution as that of tin deuterides. Assuming that the respective abundance of Sn^+ is the same for hydrides and deuterides, the ratio between them can be calculated (cf. fig. 4.21b). As a result, the neutral tin species consist of 91.65 % tin deuterides and 8.35 % tin hydrides. However, the calculations do not take into account and include mixed products containing hydrogen and deuterium.

The same behavior is observed for the native ions (cf. fig. 4.21c). The distribution of ionic tin deuterides is also similar to the expected distribution of native ions from a hydrogen plasma and is best described using RASP by taking the tin hydrides into account. Here, the native tin ions consist of 93.12 % deuterides and 6.88 % of hydrides (cf. fig. 4.21d). The relatively high fraction of 8.35 % and 6.88 % of the respective hydrides may not be explained by an impurity of the deuterium gas (5.0 purity), but imply a hydrogen source. Even in the case of a well-evacuated volume, there remains a layer of adsorbed water on the stainless steel surface, which can be desorbed and/or dissociated by the plasma and may serve as a corresponding hydride source. At this point it cannot be determined whether

4.2 Plasma-generated stannane

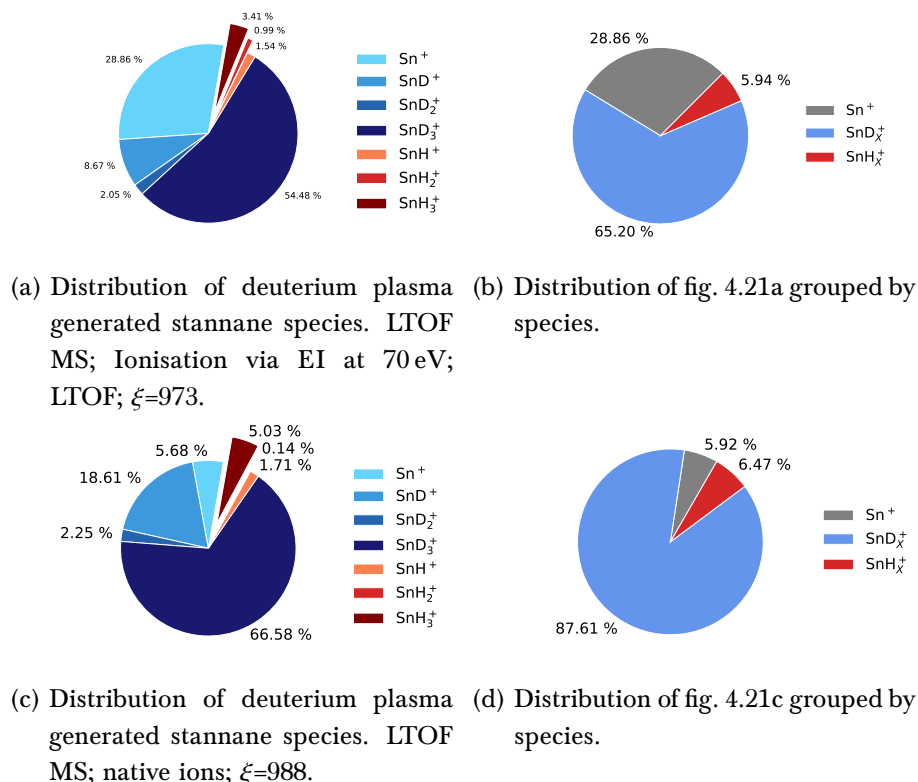


Figure 4.21: Calculated distribution of the deuterium plasma generated stannane hydrides. (a),(b): EI fragments from neutral stannane. (c),(d): native ions from the plasma.

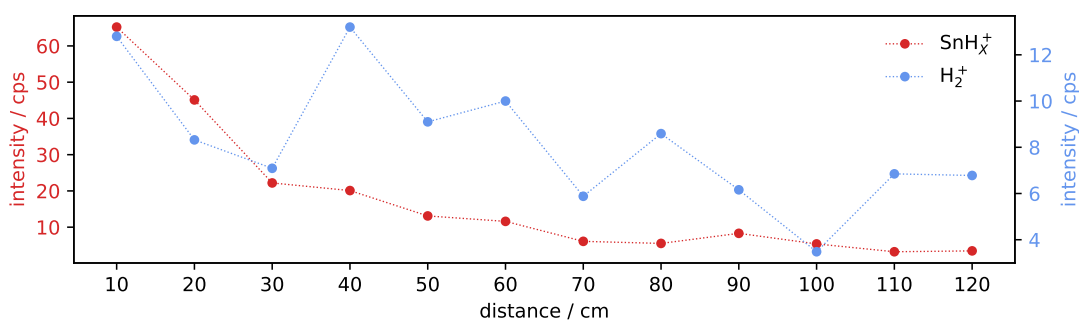
the Sn–H bond is already formed on the tin surface or in downstream gas phase reactions. Furthermore, deuterated molecules and ions such as D_2O^+ , N_2D^+ and ArD^+ were detected, as well as mixed products containing H and D, as for example HDO^+ or NH_2D_2^+ . The ratio between deuterated and hydrogenated species is similar to that of tin compounds. This strongly supports the hypothesis that there must be a surface source of hydrogen. The assumption that surface bound water most likely interacts directly or indirectly with plasma constituents and that surface chemistry plays a significant role will be discussed further down.

4.3 Transport behavior of neutral and ionic tin hydride molecules in glass tubes

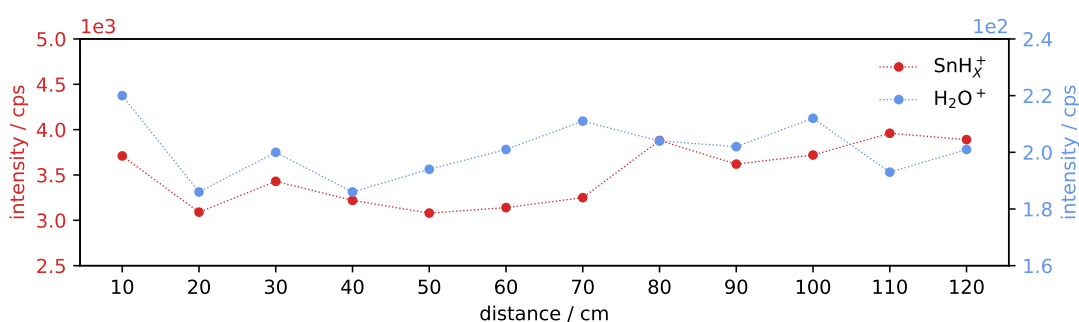
The stability of metal hydrides upon contact with surfaces has been discussed repeatedly in this work, particularly that for stannane (SnH_4). In addition to temperature, the surface material determines the rate and type of decomposition. Unlike to the LTOF/PC design, which is largely made of stainless steel, the CTOF/HCR stage design is based on a glass tube that joins the ion optics of the mass spectrometer (cf. section 3.3.2.2). The advantage of this setup is that the influence of the length of the glass tube, and therefore the surface area, can be systematically investigated without much effort. This is due to the freely selected length of the tube and the fact that the HCR plasma can be moved freely along the tube just like the tin target inside the tube. The tin target was fitted with an iron core and could thus be moved by a magnet from the outside. By recording the intensity of the corresponding neutral and ionic tin hydride fragments, two parameters can be investigated: Firstly, the influence of the distance between the source of the stannane on the target and the analyzer at a constant plasma-target distance, and secondly, the influence of the distance between the plasma source and the tin target at constant distance from the analyzer.

A 150 cm glass tube with an outer diameter of (12.09 ± 0.15) mm and a wall thickness of (0.94 ± 0.07) mm was mounted as a transfer stage for the first experiment. The distance varied is the distance between the tin target and the first electrode of the CTOF mass spectrometer. By switching the potentials of the ion source (cf. section 3.3.2.2), either native ions from the plasma or neutral molecules can be detected, the latter by employing EI. Figure 4.22a compares the signal intensities of native SnH_x ions with that of H_2^+ as a marker for non-tin ions from the plasma at different distances from the analyzer. The signal intensities of the tin hydride fragments have their maximum value of 65.2 cps at the minimum distance. As the distance increases, the intensity decreases exponentially and remains almost constant over the last few centimeters at about 3 cps. For each distance, the composition of the tin hydride fragments was determined by RASP, which, however, does not change at all. Therefore, the glass transfer stage surface does not affect the fragmentation pathway. The signal trace for H_2^+ shows clearly more fluctuations, but basically follows a similar trend. The fluctuations of both species may probably be attributed to the not always exactly identical distances between the plasma coil and the tin target. The HCR plasma inside the glass tube generates a high density of charged particles, which

4.3 Transport behavior of neutral and ionic tin hydride molecules in glass tubes



(a) Influence on the ionic fragments



(b) Influence on the neutral molecules.

Figure 4.22: Influence of the distance between tin target and analyzer at constant plasma-target distance; CTOF MS.

can affect the trajectories of the ions through space charge effects. In addition, glass is non-conductive, so that a high electric potential can build up on the inner surface, also affecting the ion trajectories as well. In order to achieve the optimal detection scheme for the plasma-generated species, the shortest possible distance between the source and the detection site should thus be selected. In general, there is a decrease in the TIC with distance, an indication that ions may be lost on the surface and thus do not reach the analyzer. The longer the distance, the greater the surface area and the greater the likelihood of invasive ion-surface interactions.

Figure 4.22b shows the dependence of the neutral molecules ionized by EI with the length of the glass tube. The signal of H₂O⁺ mainly originates from water from the gas background of the mass spectrometer. However, if larger amounts of water were produced in the plasma, this could be detected in the ionogram. The small fluctuations are probably again due to

4 Results & Discussion

the not always exactly identical distances between the plasma coil and the tin target. Taking such effects into account, it is assumed that there is no dependence on distance, neither for the tin species nor for the water species. In other words, stannane does not decompose readily on contact with the glass surface (the mean free path is a few millimeters), but is carried into the ion source with the gas flow. This is consistent with previous studies and the corresponding literature: the decomposition of metal hydrides is strongly inhibited on oxidized surfaces. However, if tin is deposited on the glass surface over time, the decomposition process becomes favorable and less stannane is detected. This process has been studied in more detail and is described in section 4.4. The experiment shows the progression of the decomposition process, where the rate is initially slow and then accelerates as tin atoms cover the surface.

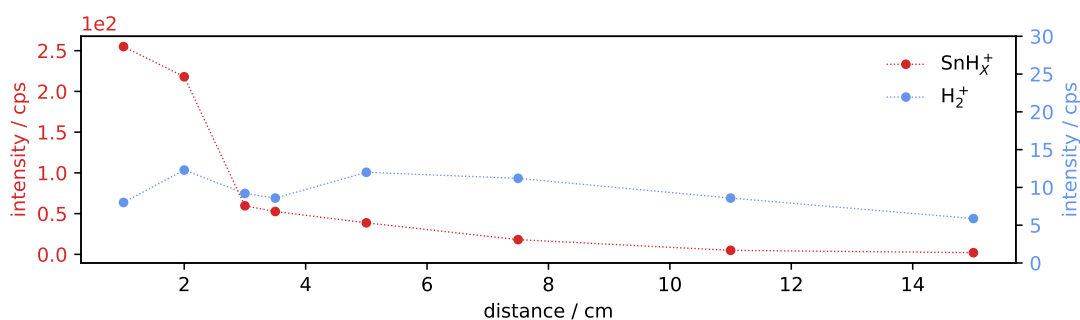
In summary, for the analysis of neutral and stable metal hydrides, even over long distances, glass is well suited.

The results of the second experiment, where the distance between the HCR coil and the target is varied at constant distance (10.3 cm) from the CTOF analyzer are presented in fig. 4.23. Plotting the signal intensity of the native ions against the distance (cf. fig. 4.23a) reveals a dependence for the stannane fragment ion signal, which is not observed for H_2^+ . At the closest distance of 1 cm between plasma and tin, the highest amount of tin hydride ions is detected with 2.55×10^2 cps. At a distance of 2 cm, the signal intensity drops only slightly to 2.18×10^2 cps. Between 2 cm to 3 cm, however, the signal drops rapidly and decreases exponentially as the distance increases. Apart from small fluctuations, the amount of H_2^+ remains stable, although a small downward trend may begin at a larger distance.

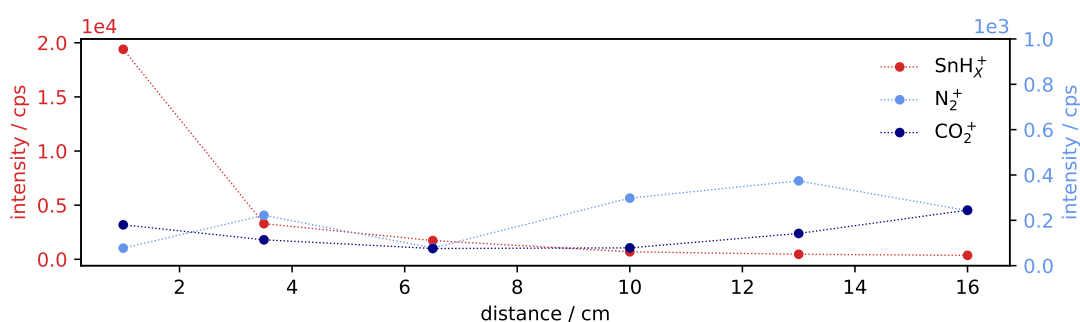
Figure 4.23b shows the dependence of the neutral molecule signal on the plasma-tin distance. For stannane, the trend is very similar to the corresponding native ions: at the shortest distance, significantly more stannanes are formed with 1.94×10^4 cps. At a distance of 3.5 cm between the plasma and tin, the signal intensity and therefore the amount of produced stannane decreases by a factor of 5. A further increase in distance yields a subsequent exponential decrease in the signal. A systematic dependence of N_2^+ and CO_2^+ with distance is not observed in the process of variation.

It was found that a much higher fractions of native tin hydride ions and neutral tin hydrides were formed when tin was in close proximity to the plasma. This may have two reasons: firstly, the density of plasma constituents is highest in the vicinity of the plasma;

4.4 Decomposition process of stannane on glass



(a) Influence on the ionic fragments



(b) Influence on the neutral molecules.

Figure 4.23: Influence of the distance between HCR coil and tin target at constant target-analyzer distance; CTOF MS.

secondly, the tin is reactive towards ions accelerated in the plasma. These ions can thus interact with the tin surface and influence the etching process.

4.4 Decomposition process of stannane on glass

Monitoring the change of the gas phase concentration of stannane by FTIR is a well suited experimental method to follow the process of stannane decomposition. For the experiment, synthesized stannane was transferred into a previously cleaned and pumped glass cell equipped with KBr windows. For the experiment, a method of the FTIR spectrometer was used in which a spectrum was recorded every 250 s to enable long-term measurements. The FTIR spectrum shown in fig. 4.24 is plotted in absorbance rather than transmission. This allows a more direct comparison of concentration and intensity. The lower the absorbance,

4 Results & Discussion

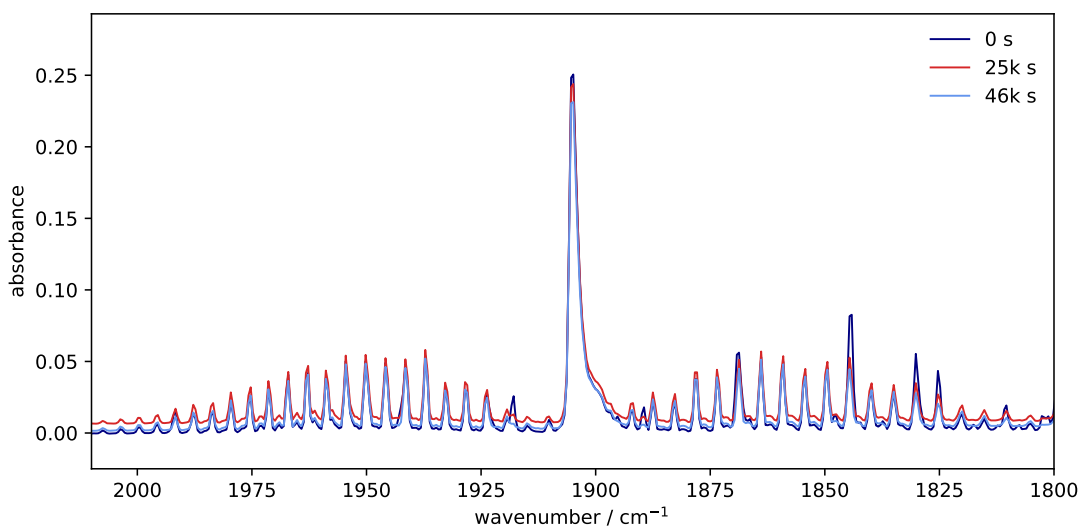
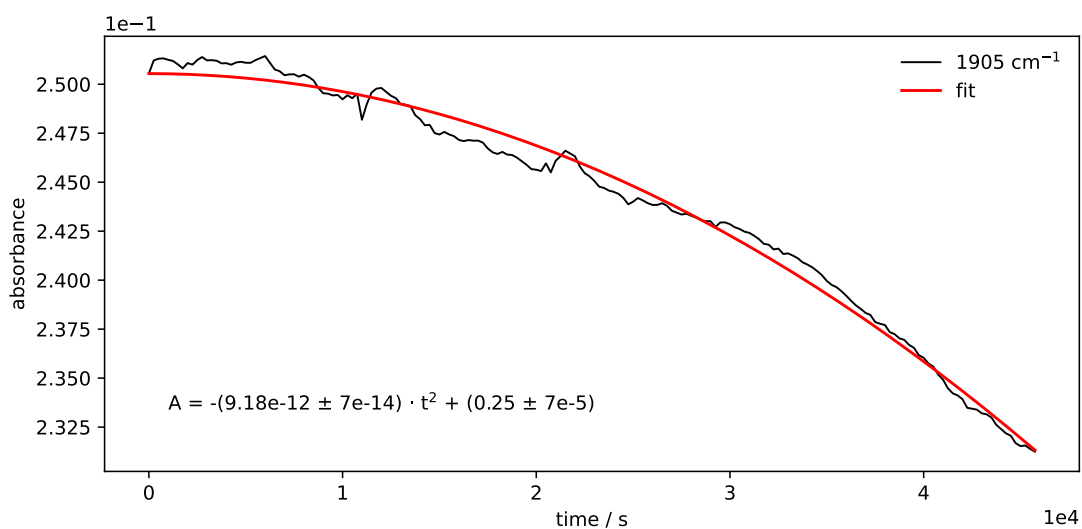


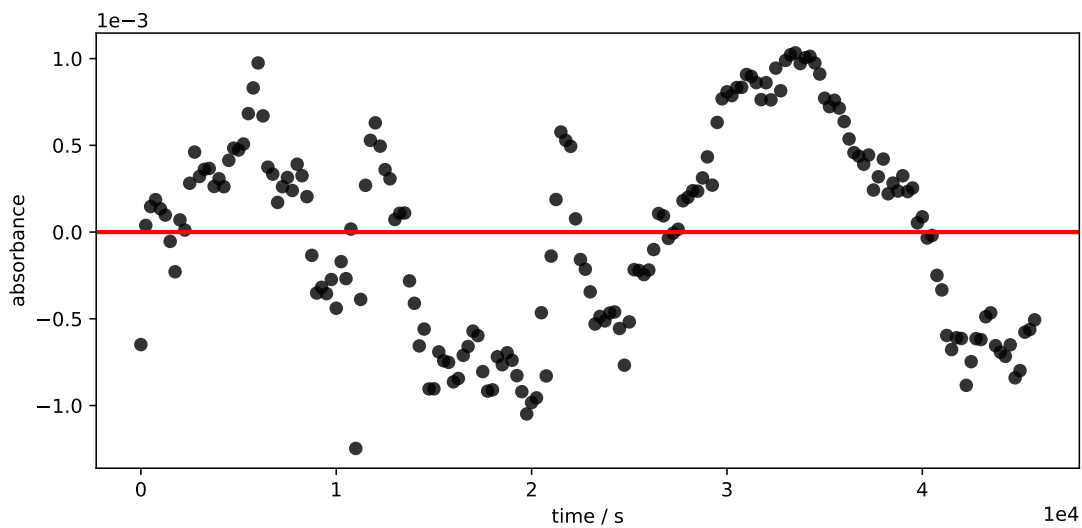
Figure 4.24: Intensity variation over time of the gas phase infrared spectrum of synthesized stannane.

the lower the corresponding concentration in a linear relationship. The monitored IR spectra are restricted to the main signal of stannane between 1800 cm^{-1} to 2050 cm^{-1} , because in this region the largest absorbance changes are expected. For illustration, the FTIR spectra recorded at 3 selected experiment times (0 s, 25 000 s, 46 000 s) are shown in the plot, which indicate a decreasing intensity of the signals with time. In order to further investigate the process of decomposition, the intensity change of the feature at 1905 cm^{-1} with time is plotted in fig. 4.25a. The data clearly show a decrease in intensity which is slow initially and then accelerates. The applied fitting function (red curve) describes the curve fairly accurately, assuming a quadratic function. The corresponding function is also given in the plot. A residual plot of the data was made, as shown in fig. 4.25b, to validate the applicability of the determined function. A random scatter around the function would confirm the applicability. In this case there are values only above or below the straight line in some areas, indicating a deviation from the function. However, the fluctuation of the entire measurement series is relatively high, which renders a better fit difficult. In general, however, sufficiently small deviations from the fitted function is observed. It is therefore argued that the stannane decomposition rate corresponds with a quadratic function.

4.4 Decomposition process of stannane on glass



(a) Intensity of the signal at 1905 cm⁻¹ versus time. A quadratic fit is also plotted and the corresponding function is given.



(b) Residual plot of the data shown in (a).

Figure 4.25: Intensity variation over time of the 1905 cm⁻¹ signal from synthesized stannane in the FTIR spectrum and fitting of the data.

4 Results & Discussion

The rapidly decreasing intensity of the signal, and thus the gas-phase concentration of stannane, can be explained by the way stannane is decomposing. As already discussed, decomposition is favored on clean metal surfaces, but strongly inhibited on oxide surfaces. Accordingly, the rate of stannane decomposition on the glass surface of the cell is very low initially, but the more tin is deposited on the glass surface, the higher the decomposition rate. The decomposition process of stannane on tin is highly favored and tin islands start to grow, as described in section 2.4.1.1. It is therefore a self-accelerating, surface-driven process. This experiment is yet another demonstration of the importance and the influence of the surface material in the decomposition process of these kinds of molecules.

4.5 Other plasma-generated metal hydrides

In addition to tin/ stannane, which is the primary subject of this work, others metals have been studied under nearly identical conditions. However, the investigation was not as systematic and extensive as for tin. The research objective for these metals was to evaluate their ability to form hydrides that are stable enough to be detected by mass spectrometers. From these measurements, conclusions can then be drawn about their potential for contamination in the vicinity of the plasma. Different plasma sources, gas compositions, and mass spectrometers were used for the studies.

Lead (Pb), magnesium (Mg), copper (Cu), silicon (Si), tantalum (Ta) and nickel (Ni) were studied. The metal samples are either present as foils or small chunks.

No corresponding molecules or native ions were detected for the metals tantalum and nickel. The results for silicon are inconsistent. N_2^+ and N_2H^+ have the same nominal masses as Si^+ and SiH^+ , respectively, and due to the significantly higher signal intensity of the nitrogen species, any silicon (hydride) signals that may be present are masked.

The non-detectability of Ta and Ni may have a number of reasons, which are summarized as follows: (1) the experimental setup is not sufficiently sensitive, (2) the generated metal hydrides are unstable and (3) the natural oxide layer present on the metal samples are too stable and/or too thick and thus not accessible to excited hydrogen. (1) may be alleviated by an optimized and specifically tailored coupling between plasma and analyzer, as well as by accumulating the mass spectra over a long period of time. For the assessment of (2) and (3), there are unfortunately no data on the stability of the corresponding hydrides, as well as on the reactivity (homogeneous and heterogeneous) and volatility of the reaction

products available.

4.5.1 Lead (Pb)

As a member of the 14th group of the periodic table (carbon group), lead (Pb) has a reactivity towards excited hydrogen which is comparable to the corresponding hydride of tin. The thermodynamic instability of plumbane (PbH_4), like that of stannane, is well known and has been described in the literature[104]. Interaction of plumbane with surfaces leads to decomposition reactions to the elements, forming a Pb mirror on the surface. Due to the fact that lead has only four stable isotopes (^{204}Pb , ^{206}Pb , ^{207}Pb and ^{208}Pb), the expected mass spectrum is less complex than that of stannane, which has ten stable isotopes.

The mass spectrum of the ionic plumbane fragments is displayed in Figure 4.26. The associated signals range from m/z 204 to 211, with m/z 208 at maximum abundance. The detected signals originate exclusively from native ions from the plasma volume, as no further ionization takes place within the CTOF. The presence of the corresponding signals in the mass spectrum proves that lead hydrides are formed by interaction of excited hydrogen with the metallic lead. Comparison with mass spectra obtained with the LTOF and the sector field mass spectrometer reveals that the CTOF records superimposed signals at each m/z value. However, using the software RASP, the relative fractions of the species present are calculated. The high matching coefficient of $\xi=987$ indicates that the calculated distribution is very close to the experimental mass spectrum. The distribution shows that the ionic fragments are mainly consist of Pb^+ (86.00%). The species PbH^+ (11.45%) and PbH_3^+ (2.55%) are present to a much lesser extent and PbH_2^+ is not detectable at all. The high fraction of the metal ions indicates a high degree of fragmentation, assuming that PbH_4 forms on the lead surface as the precursor molecule. A very similar distribution is observed in the investigation of the native ions of stannane with the CTOF. Accordingly, the signal distribution appear to be setup-dependent.

Oxygenated plumbane with the molecular formula $\text{PbOH}_x^{(+)}$ is formed in the same way as the stannane equivalent. No further studies of the formation conditions for Pb have been carried out, but the chemical similarity to tin strongly suggests that the same heterogeneous reactions lead to the lead hydride molecule. As a result of surface and/or

4 Results & Discussion

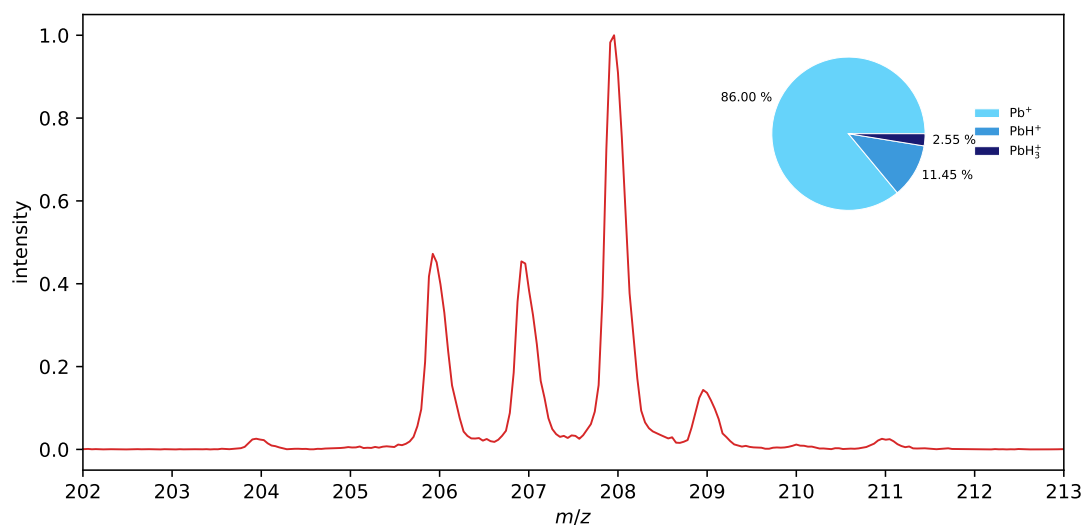


Figure 4.26: Mass spectrum of plasma generated plumbane (PbH_X^+); CTOF MS; native ions; $\xi = 987$.

gas-phase reactions in the plasma, these compounds fragment and are detected as native ions. The corresponding mass spectrum is shown in fig. 4.27. The mass spectrum of the oxygenated lead hydride fragments range from m/z 223 to 229 with m/z 225 as the signal with the highest abundance. Again, only the superimposed signals are detected due to the limited CTOF resolution; using the software RASP ($\xi = 972$) the following distribution are calculated: PbO^+ (1.80%), PbOH^+ (35.38%), PbOH_2^+ (26.02%), PbOH_3^+ (28.16%) and PbOH_4^+ (8.64%). The observation that PbOH_4^+ occurs with significant abundance is remarkable. Both in the experiment and in the literature, the tin equivalent cannot be detected at all or only to a negligible extent due to its low stability. A definitive confirmation of the existence of this ion would be a signal at m/z 212 since this signal can only be caused by $^{208}\text{PbH}_4^+$. However, due to the low intensity in the mass spectrum, this cannot be confirmed at this time.

The CTOF is capable of also detecting neutral metal hydrides by ionizing and fragmenting them with EI in the ion source of the mass spectrometer. However, the coupling of the HCR plasma source with the CTOF is currently far from being optimized for metal hydride detection as there are several metal surfaces present in the sampling path, and, in

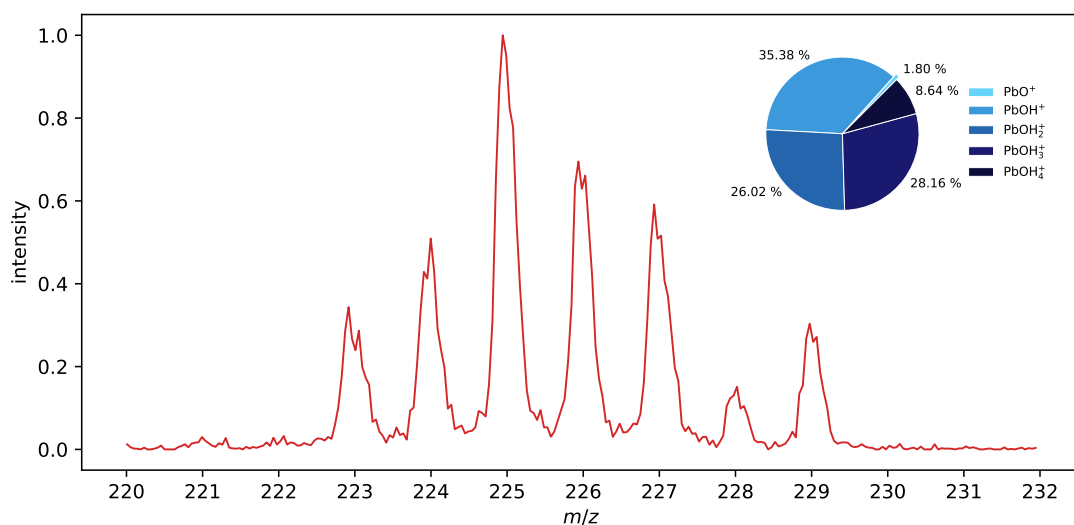


Figure 4.27: Mass spectrum of plasma generated oxygenated plumbane (PbOH_x^+); CTOF MS; native ions; $\xi = 972$.

general, the surface-to-volume ratio is unfavorable. Thus, only the most prominent signal at m/z 208 is clearly detectable and assignable. Other signals are buried in the background. The mass resolution of the CTOF is not sufficient to discern the lead hydride signals from those of the background (mainly HCs). The nominal mass alone cannot be used to determine which species (one or more) cause the signal at m/z 208. Theoretically, the following ionic species or the superimposition of several are possible: $^{208}\text{Pb}^+$, $^{207}\text{PbH}^+$, $^{206}\text{PbH}_2^+$ and $^{204}\text{PbH}_4^+$. Hydrogen isotopes are not taken into account due to their low abundance. Without additional signals, a calculation of the individual proportions of different species with RASP is not possible. The low signal intensity of the lead hydrides may also be due to the general instability of these molecules in addition to the unfavorable coupling between plasma source and CTOF. According to Saalfeld[104], plumbane is significantly less stable than the other metal hydrides of the 14th group of the periodic table and thus rapidly decomposes into the elements.

In addition to the mass spectrum of stannane already described in section 4.1.2, the only available literature mass spectrum of plumbane also emerges from the work of Saalfeld and Svec[105]. The relative distribution pattern of the literature spectrum is listed in table 4.6. The pattern reveals that fragmentation by EI of plumbane yields mainly PbH_2^+ and PbH_3^+ and to a certain extent Pb^+ . However, the characterization of the CTOF/HCR setup leads

4 Results & Discussion

Table 4.6: Distribution of plumbane fragments from Saalfeld and Svec and possible species from CTOF measurement.

| species | Saalfeld, Svec | CTOF |
|-------------------------------|----------------|----------|
| Pb ⁺ | 25.0 % | possible |
| PbH ⁺ | 5.0 % | possible |
| PbH ₂ ⁺ | 100.0 % | possible |
| PbH ₃ ⁺ | 60.5 % | - |
| PbH ₄ ⁺ | <0.01 % | possible |

to a significantly higher fragmentation degree than the other mass spectrometer coupling stages used, resulting mainly in observations of the M⁺ species. Thus, it is conceivable that in this setup the fragmentation pattern of plasma-generated neutral plumbane shows mainly the pure metal cation. This is consistent with the experimental spectrum (cf. fig. 4.26) granted the signal at m/z 208 is caused by ²⁰⁸Pb⁺.

Expected species (molecules or native ions) such as doubly charged plumbane fragments or plumbane dimers can not be identified with certainty because the signal intensity is not sufficient. However, the appearance of the signal at m/z 208 proves that neutral lead molecules are formed as a result of the plasma interactions and can be analyzed using EI. It is assumed that the molecule is PbH₄ as the precursor molecule. It is further assumed that the other species also form with lead and would be detected with sufficient sensitivity.

4.5.2 Magnesium (Mg)

Magnesium (Mg) belongs to the alkaline earth metals (group 2 of the periodic table). There are three stable isotopes of magnesium. In Mg compounds, it mostly has an oxidation number of +2. The only known stable molecule with magnesium and hydrogen is magnesium hydride (MgH₂). MgH₂ is a colorless, crystalline substance, which is not volatile and decomposes into the elements at higher temperature. However, surface reactions between magnesium metal and excited hydrogen are not reported in the literature.

Somewhat surprisingly, experiments conducted demonstrate that neutral magnesium hydrides are formed by the interaction of magnesium metal and hydrogen plasma species.

The mass spectrum of the neutral molecules ionized with EI is presented in fig. 4.28. The MAT95 mass spectrometer provides bar plots as the default output. For the plotted mass spectrum, a Gaussian curve was applied to the bar values, which has a width corresponding to the resolution of the mass spectrometer. The spectrum ranges from m/z 24 to 29 with a maximum signal intensity at m/z 26. Using RASP, the fragment distribution is calculated with a matching factor of $\xi = 993$. The experimental mass spectrum is very well matching with the theoretical mass spectrum. According to RASP, the ensemble consists of Mg^+ (3.36%), MgH^+ (12.45%), MgH_2^+ (66.82%) and MgH_3^+ (3.36%). This suggests, a tetrahydride and not a dihydride as precursor. In this context, the chemical ionization (CI) part in an EI ion source has to be taken into consideration (cf. section 2.6.1.2). The hydrogen gas as matrix, despite the relatively low pressure in the ion source of the sector field mass spectrometer causes CI. The ratio of ArH^+/Ar^+ is a useful indicator of the extent of CI occurring in EI mode at the corresponding conditions. The CI ratio was 1.6% in the studies with Mg, which means this is not sufficient as a sole explanatory factor for the occurrence of MgH_3^+ , assuming MgH_2 as precursor molecule. The neutral precursor molecule cannot be deduced directly from the mass spectrometric measurements. It is also possible that under the conditions prevailing in the experiment, higher magnesium hydrides may be formed than under normal circumstances. The determination of the native Mg could provide additional information about the structure and the formation of these species.

Compounds such as oxygenated magnesium hydride and the magnesium hydride dimer were not detected. It remains unclear whether this is due to insufficient sensitivity of the experimental setup or to the instability of these molecules under the prevailing conditions.

4.5.3 Copper (Cu)

Copper is a group 11 element of the periodic table with only two stable isotopes (^{63}Cu , 69.15% and ^{65}Cu , 30.85%). In the case of copper, in addition to the general question of the possibility of volatile compounds being formed in the presence of a hydrogen plasma, the influence of different oxidation states of the Cu surface on building volatile compounds is of particular interest.

An oxidized copper component with characteristic reddish surface was exposed to a hydrogen plasma under the same condition as for the metals described previously. The plasma products (neutral and ionic) were determined using the LTOF mass spectrometer. In preliminary experiments, a bare copper sample was treated with hydrogen plasma to investigate the ability to form volatile hydrides in general. Both the oxidized copper piece and the bare copper piece did not yield neutral or ionic copper species at all that were

4 Results & Discussion

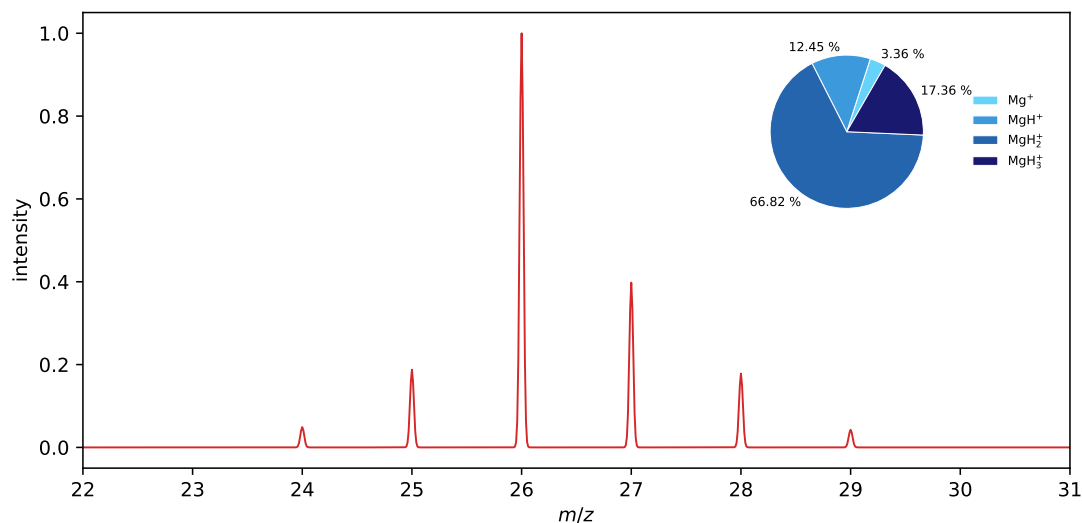


Figure 4.28: Mass spectrum (processed) of plasma generated magnesium hydride (MgH_x^+); SF MS; EI at 70 eV; $\xi = 993$.

detectable by the LTOF. Sensitivity enhancement attempts and long-term signal accumulation were also unsuccessful regarding the recording of any copper related mass signals. It is not evident from the experimental results whether this is due to the lack of formation of corresponding volatile compounds or to metrological reasons.

According to Wu et al.[106] the etching of Cu using a hydrogen plasma without additional chemical agents or physical methods is hardly possible and mostly ineffective. Examples of these agents are, in the chemical case, pre-etching by chlorine gas plasma and, in the physical methods case, activation by laser, UV or IR radiation. One of the main reasons is the instability of the reaction product CuH at temperatures above 273 K. CuH slowly decomposes into the elements. This reaction accelerates drastically at higher temperatures and beyond 373 K the molecule decomposes instantaneously[106]. Furthermore, experimental and theoretical studies[107, 108] suggest that the gas phase reaction



has no activation barrier and there is no evidence for an intermediate CuH_2 species. The density of H radicals in the plasma as well as in the EI source is far sufficient to drive such a reaction.

Additionally, from the work of Fitzsimons and Jones[109], it follows that copper hydride

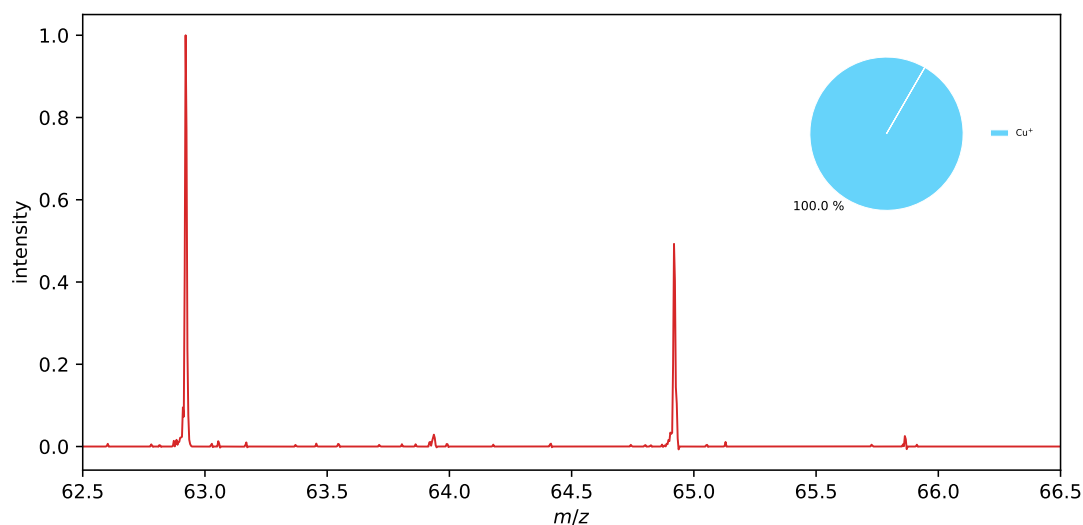


Figure 4.29: Mass spectrum of copper ions by laser ablation (Cu^+); LTOF MS; native ions; $\xi = 997$.

is very sensitive to irradiation with electrons present in an electron microscope and rapidly decomposes into ultra-fine copper particles and hydrogen. Even though the electron energies are not comparable between an electron microscope and an EI source or plasma, certain parallels can be drawn regarding the stability of copper hydrides towards electron collisions. However, if even the hydride is formed on the copper surface in the experiment, it may swiftly decompose in the plasma directly or after transport into the EI source without forming cations.

To increase the probability of detecting copper or copper hydride as neutral molecules or ions, a quartz window was mounted on the plasma chamber. The unfocused fundamental of an Nd:YAG laser with 500 mJ at 1064 nm (cf. section 3.6) was directed perpendicularly onto the copper target within the chamber to maximize the photon exposure on the target surface. Based on Wu[106], the additional energy should enable or accelerate the etching process with excited hydrogen. Various experiments were carried out with and without hydrogen gas at different pressures and with and without ignited plasma.

The resulting mass spectrum of the ionic species without added hydrogen is displayed in fig. 4.29. The mass spectrum essentially consists of two signals at m/z 63 and m/z 65,

4 Results & Discussion

which are the two stable isotopes of Cu^+ with the ratio of 1 : 0.45. This corresponds exactly to the natural isotope distribution. The signals at m/z 64 and m/z 66 could theoretically belong to copper species and represent the respective hydride CuH . However, the relative intensity does not correlate with the isotopic ratio. The calculation with RASP yields a distribution of only Cu^+ . Furthermore, adding hydrogen to the PC does not increase the presumed copper hydride signals, but results in a generally lower signal intensity of the copper ions, depending on the chamber pressure. It is thus irrelevant whether the plasma is ignited or not. No corresponding signals are detected in the search of neutral copper (hydrides) using the EI mode of the LTOF. Regardless of whether hydrogen is added or the plasma is ignited.

Only the irradiation of the target with the laser light leads to the detection of Cu ions with the LTOF. The experimental results suggest that this is a pure laser ablation process and that there is no activation of the hydrogen etching process at all. Higher chamber pressures lead to a significant reduction on the mean free path length, which reduces the probability of ions passing into the analyzer, resulting in a decreasing signal intensity.

In general, no difference was observed in the experiments using the oxidized and the bare copper target. However, both targets show an initially increasing signal intensity of the copper ions, which decreases after few seconds and then remains constant. This effect is reproducible by moving the laser spot to another area of the metal surface. In the case of the oxidized copper target, the exposure to the IR radiation results in a removal of the reddish oxide layer finally yielding a pure copper surface. In conclusion, a significant effect of a surface oxide on building volatile Cu species was not observed in the laboratory experiments.

4.6 DFT calculations

The DFT calculations performed are intended to aid in understanding the experimental mass spectra and the underlying formation mechanism of stannane and other metal hydrides. For this purpose, geometry optimizations were performed. In a typical geometry optimization calculation the local minimum of the energy $E(r)$ for an initial input structure is searched. In each numerical step of the calculation the distance r between the atoms is changed as the energy of a structure $E(r)$ is a function of r . This finally leads to the most stable conformation for the structure. The software and methods used are detailed in section 3.8.2. Two basis sets (3-21G and DEF2-TZVPP) were used and the results were compared. 3-21G is the smallest of the Pople basis sets and is used to initially probe the

stability, before calculating the structures using the latter Karlsruhe basis sets. These have a considerably larger set of functions and thus lead to much more precise results. Due to the small extent of functions, the Pople basis sets are very efficient in terms of calculating speed and computational cost and are thus used for initial optimizations. The resulting calculated energies are not directly comparable with each other, but principally indicate the same trends in the respective stabilities.

From the experimental results, as well as from the literature, the existence of different cationic and neutral tin hydrides is established, thus some of these structures are initially investigated with DFT calculations. Generally, the study includes neutrals, cations and anions of various metal hydrogen compounds as well as species as for example dimers. All energies are given in units of Hartrees (a.u.).

4.6.1 Cationic tin species

Geometry optimization yield the calculated energy $E(r)$. The values for the energies of the cationic tin species are given in table 4.7, but some of the calculations did not converge. This could be due to a number of reasons. For example, the number of iteration steps may be too small or a certain threshold may not be reached at the end of the calculations. For these molecules, further investigations could be promising. In some cases the molecules dissociated/fragmented in a specific pattern, e.g. Sn^+ and Sn . This is indicated appropriately.

The results for the cationic tin hydrides (SnH_x^+) provide only partial agreement with the experiments. Not all experimentally observed ions are reproduced in the calculations. For SnH_4^+ , SnH_2^+ and SnH^+ the calculations with 3-21G basis set suggest that there is no stable geometry and either the ions fragment into smaller ions under ejection of H atom(s), or, for SnH_2^+ there is no convergence. Using the DEF2-TZVPP basis set, SnH_4^+ and SnH_2^+ do not converge in the calculations. This consistent with the experimental results for the unstable SnH_4^+ . Saalfeld et al.[83] have reported the detection of this ion, but only at very low abundance and not without doubt, as discussed before. However, the proposed dissociation of SnH^+ and the non-stability of SnH_2^+ are not consistent with experimental observations. Further calculations with optimized input parameters or other basis sets are thus necessary. All results and conclusions for cationic deuterated tin species (SnD_x^+) are identical to those for the equivalent hydrogen species.

4 Results & Discussion

Table 4.7: Results of the calculation of the cationic tin species.

| species | 3-21G | DEF2-TZVPP |
|-------------------------|--|--|
| Sn^+ | minimum found | minimum found |
| SnH^+ | dissociation into Sn^+ and H | minimum found |
| SnH_2^+ | no convergence | no convergence |
| SnH_3^+ | minimum found | minimum found |
| SnH_4^+ | dissociation into SnH_2^+ and 2 H | no convergence |
| SnD^+ | dissociation into Sn^+ and D | minimum found |
| SnD_2^+ | no convergence | no convergence |
| SnD_3^+ | minimum found | minimum found |
| SnD_4^+ | dissociation into SnD_2^+ and 2 D | no convergence |
| SnO^+ | minimum found | minimum found |
| SnOH^+ | no convergence | no convergence |
| SnOH_2^+ | minimum found | minimum found |
| SnOH_3^+ | dissociation into SnOH_2^+ and H | minimum found |
| Sn_2^+ | dissociation into Sn^+ and Sn | dissociation into Sn^+ and Sn |
| Sn_2H^+ | no convergence | dissociation into Sn^+ , Sn and H |

In the case of the oxygenated tin hydride ions (SnOH_X^+) the DEF2-TZVPP basis set is better suited in reproducing the experimental results, in so far that SnOH_3^+ has a stable geometry. When the 3-21G basis set is used, dissociation into SnOH_2^+ and H occurs. For the SnOH^+ ion, no convergence occurs using both basis sets. An interesting fact is that there are two different results for SnOH_2^+ using the 3-21G basis set. While the initial optimization from the geometry input suggests an isomer with a hydrogen atom attached to both, the tin and the oxygen atom, the dissociation of SnOH_3^+ suggests an isomer where both hydrogen atoms are attached to the oxygen atom and the weaker bond between the tin atom and the third hydrogen atom cleaves. The non-converged molecular states suggest dissociation between oxygen and hydrogen when using 3-21G and no cleavage with DEF2-TZVPP.

The experimental results prove the existence and formation of tin hydride dimers (Sn_2H_X^+). Both basis sets do not lead to a corresponding calculated structure. When using the DEF2-TZVPP basis set both ions Sn_2^+ and Sn_2H^+ dissociate into the tin ion(s) and with the 3-21G basis set, the Sn_2H^+ ion model does not converge.

Table 4.8: Results of the calculation of the neutral tin species.

| species | 3-21G | DEF2-TZVPP |
|------------------|----------------------------|------------------------------|
| Sn | minimum found | minimum found |
| SnH | dissociation into Sn and H | minimum found |
| SnH ₂ | no convergence | dissociation into Sn and 2 H |
| SnH ₃ | minimum found | minimum found |
| SnH ₄ | minimum found | minimum found |
| SnD | dissociation into Sn and D | minimum found |
| SnD ₂ | no convergence | dissociation into Sn and 2 D |
| SnD ₃ | minimum found | minimum found |
| SnD ₄ | minimum found | minimum found |

In summary, both basis sets used to investigate the stability of cations cannot satisfactorily reproduce the experimental results. However, the calculations show a similar trend for the molecules when a minimum was found. The stabilities in turn allow conclusions to be drawn about the fragmentation processes. In order to be able to describe all the molecules and ions observed, further calculations and the application of other basis sets are mandatory.

4.6.2 Neutral tin hydrides

Neutral metal hydrides can only be detected with mass spectrometry upon their ionization. This makes simulations of potentially occurring neutral species of high interest, as this may provide direct insights into their formation mechanism. The results shown in table 4.8 are calculations for the neutral tin hydrides that may occur.

Again, there is a discrepancy between the two used basis sets concerning the SnH molecule. Since the cationic species was better modelled by the DEF2-TZVPP basis set, it is reasonable to assume that this is also the case here. Unlike its cation, SnH₃ is not trigonal planar symmetric, but rhombohedral tetrahedral symmetric. For SnH₄, the calculations indicate a stable molecule in contrast to the cation. The results in the case of non-convergence for SnH₂ indicate bond cleavage as well as when using DEF2-TZVPP. The

Table 4.9: Results of the calculation of the anionic tin species

| species | 3-21G | DEF2-TZVPP |
|------------------|--|---|
| Sn^- | minimum found | minimum found |
| SnH^- | dissociation into Sn^- and H | dissociation into Sn^- and H |
| SnH_2^- | no convergence | no convergence |
| SnH_3^- | dissociation into Sn, H^- and 2 H | dissociation into Sn, H^- and 2 H |
| SnH_4^- | dissociation into Sn, H^- and 3 H | dissociation into SnH_2 , H^- and H |
| SnD^- | dissociation into Sn^- and D | dissociation into Sn^- and D |
| SnD_2^- | no convergence | no convergence |
| SnD_3^- | dissociation into Sn, D^- and 2 D | dissociation into Sn, D^- and 2 D |
| SnD_4^- | dissociation into Sn, D^- and 3 D | dissociation into SnD_2 , D^- and D |

results for the tin-deuterium compounds are identical to those for the hydrogen equivalent. The identical behaviors is also seen in the experimental results.

In general, the results suggest the existence of several stable tin-hydrogen compounds. Whether and how such molecules are formed remains unclear. In the literature it is generally assumed that SnH_4 is the primary product of tin etching. How the other species are formed, and whether they form directly on surfaces or in the gas phase, remains to be investigated.

4.6.3 Anionic tin hydrides

Due to the large number of free electrons in the plasma and their broad kinetic energy distribution, anionic plasma products are plausible. However, since none of the mass spectrometers used has a negative operational mode, no corresponding experiments were possible. Therefore, the simulation results are of great interest, which are listed in table 4.9.

Here, both basis sets yield similar results with the exception of the SnH_4^- ion, where different dissociation products are calculated. However, the results of the bond cleavage are expected, as the basis set DEF2-TZVPP did converge predicting a neutral SnH_2 molecule

as one product channel, while application of the 3-21G set, resulted information of the elements. Both cases of non-convergence suggest a bent molecule without bond cleavage occurring. Once again, the results obtained with deuterium are exactly the same as those obtained with hydrogen.

In general, if the calculated results are reliable, only Sn^- and H^-/D^- are expected in the negative mode for mass spectrometric experiments. As the inconsistent results show, it may be possible to detect $\text{SnH}_2^-/\text{SnD}_2^-$ as well.

4.6.4 Conclusion of the simulation results

In addition to the energies, the calculations yield optimized molecular geometries when a stable conformation results. Selected geometries are shown in fig. 4.30.

The main intention of the DFT calculations was to validate the experimental data with calculations and to identify species that are not experimentally detectable. The study was useful in highlighting the differences between two different basis sets used in the DFT calculations. In the case of charged tin molecules, the DEF2-TZVPP performed superior and in better agreement with the experimental results, while the 3-21G basis set was superior for neutral molecules. For a better and more complete computational description of the tin species, it is necessary to find a more suitable basis set. Nevertheless, the results described provide a basis for further calculations.

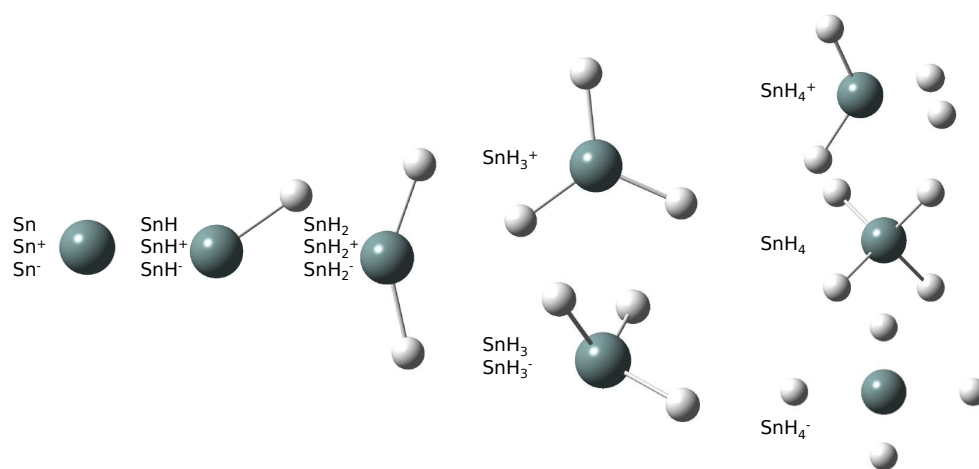
4.7 Initial etching phenomenon

4.7.1 Description of the phenomenon

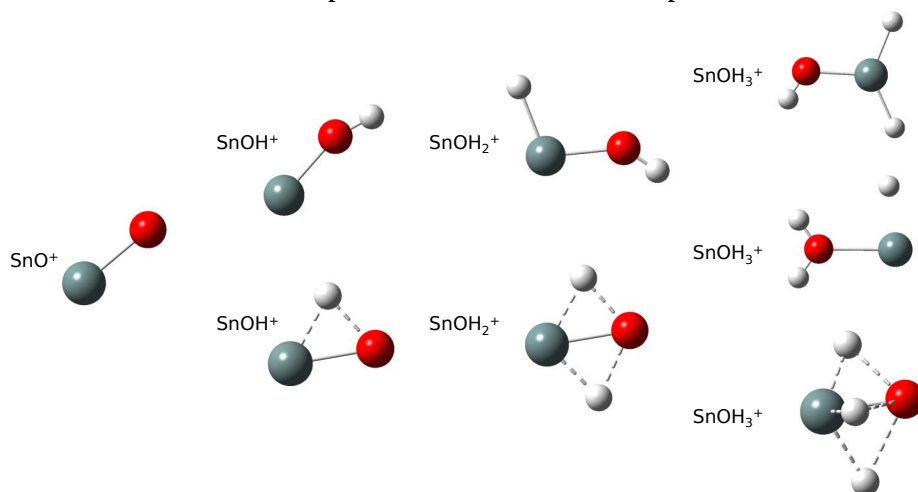
When the plasma is switched on after a new metal target has been introduced into the plasma chamber (PC), e.g. a solid tin target, an event that lasts several hundred seconds take place reproducibly: Within a few seconds after the ignition of the hydrogen plasma, the extracted ion current (EIC) of stannane reaches its maximum, before an exponential signal decrease takes place until a constant signal intensity is reached. This phenomenon is independent of the used mass spectrometer and the plasma source. The general trend remains the same. However, the duration of the decrease and the height of the maximum vary from experiment to experiment.

Figure 4.31 illustrates an example of the temporal evolution of the EIC of stannane using the LTOF/PC setup. At 0 s, the hydrogen plasma is ignited and the signal reaches its maximum almost instantaneously. The signal then decreases exponentially until a constant

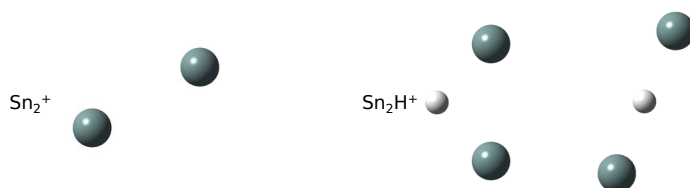
4 Results & Discussion



(a) Optimized structures of SnH_X species.



(b) Optimized structures of SnOH_X species.



(c) Optimized structures of Sn_2H_X species.

Figure 4.30: Optimized structures of the DFT calculated tin species.

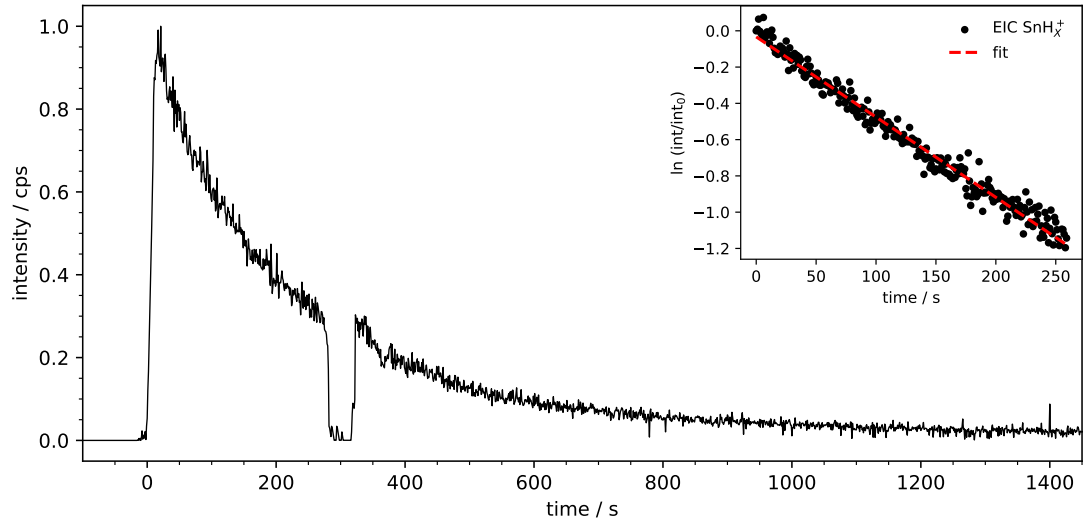


Figure 4.31: Ionogram of plasma-generated stannane. The hydrogen plasma ignites at 0 s and is temporarily switched off between 260 s to 330 s. Additionally, a linear fitting function is applied to the data. LTOF MS; native ions.

signal intensity is reached after about 1200 s, which in this case is about 5% of signal intensity of the maximum. The intensity of the signal then remains constant for hours. The exponential trend (here the first 250 s) is linearized by plotting $\ln(\text{int}/\text{int}_0)$ against time (cf. overlay plot in fig. 4.31), where int_0 is the maximum intensity and int the intensity at time t . A linear relationship is apparent, translated to a first order kinetics. Applying a fitting function to the data yields the following function:

$$f(t) = k \cdot t = (-4.42 \cdot 10^{-3} \pm 4 \cdot 10^{-5}) \cdot t \quad (4.1)$$

The determined slope represents the rate constant k and the corresponding half-life ($t_{1/2}$) is calculated via

$$t_{1/2} = \frac{\ln(2)}{k} = (156.82 \pm 1.46) \text{ s} \quad (4.2)$$

as about 157 s. This extended period of time is more likely pointing to slowly changing source properties than to plasma equilibration processes.

The slope calculated via eq. (4.1) represents the sum of all signals assigned to stannane. The same fitting procedure can be performed for each individual EIC of stannane as

4 Results & Discussion

Table 4.10: Calculated slopes and errors of the slopes of selected EICs from stannane.

| m/z | slope | error |
|-------|------------------------|----------------------|
| 112 | -1.97×10^{-3} | 3.8×10^{-4} |
| 118 | -4.56×10^{-3} | 1.3×10^{-4} |
| 119 | -4.46×10^{-3} | 1.1×10^{-4} |
| 120 | -4.37×10^{-3} | 9×10^{-5} |
| 121 | -4.51×10^{-3} | 8×10^{-5} |
| 122 | -4.50×10^{-3} | 1.1×10^{-4} |
| 123 | -4.38×10^{-3} | 8×10^{-5} |

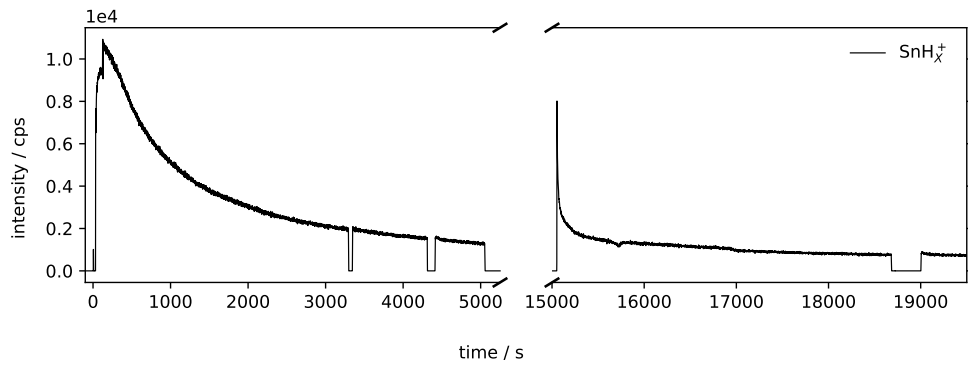
displayed in table 4.10. The results reveal slopes that are in the same range with minimal deviations, except for the EIC of m/z 112, which is smaller. The associated error is also the highest by comparison, further indicating that the data are affected by noise in the mass spectrum. The signal is not fully resolved from the background. The remaining peaks between m/z 112 and 118 were not identified. Excluding m/z 112, the individual slopes and therefore the half-life values show almost the same value, proving that there is no shift in relative intensities and therefore no shift in fragment distribution during this period of time. The entire etching process is accelerated and/or energetically more favorable during the initial period.

Between 260 and 330 s the plasma is temporarily switched off. As a result, the signal intensity immediately drops to zero. It is noteworthy that after the plasma is turned on again, the signal returns to the same value when the plasma was turned off. This suggests that it is not an effect of switching on and off the plasma, but rather a change in the experimental conditions during the etching process. A systematic investigation of this effect is described in the following.

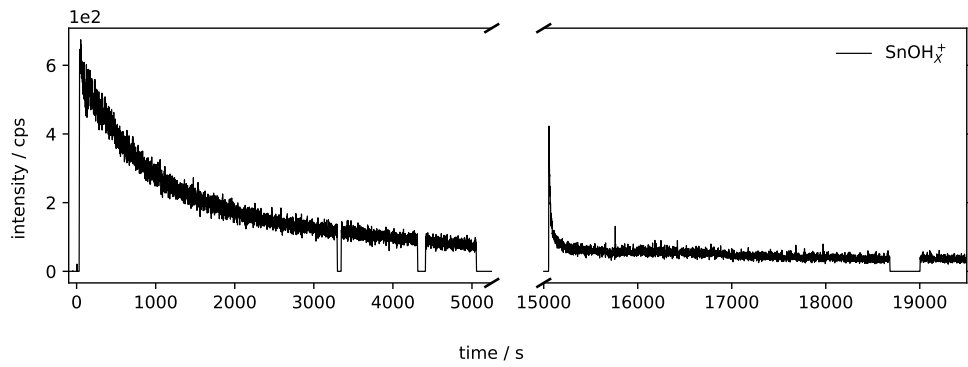
4.7.2 Oxygen exposition

Even after extended exposure to hydrogen (independent of the pressure) with the plasma turned off, the effect of a strong initial signal increase followed by an exponential signal decrease is not seen, but even a short exposure to laboratory air is sufficient to cause this effect. The extent of the effect here depends on the duration of laboratory air exposure. It stands to reason that this is related to either oxygen or water present in the laboratory air,

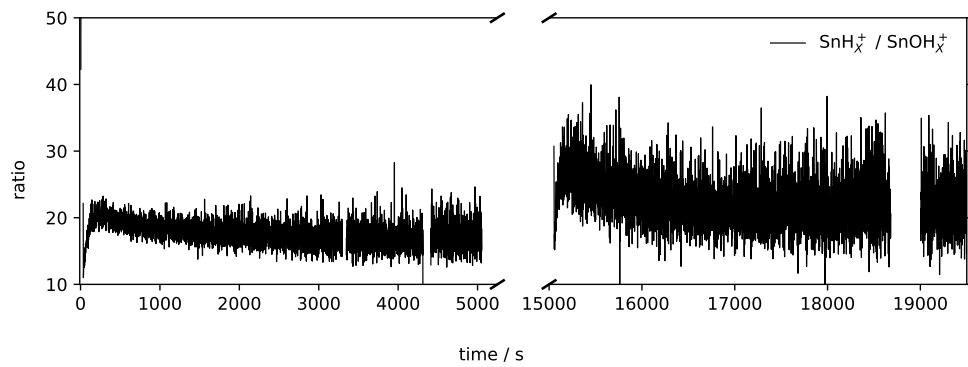
4.7 Initial etching phenomenon



(a) Ionogram of stannane (SnH_x^+).



(b) Ionogram of oxygenated stannane (SnOH_x^+).



(c) Ratio of $\text{SnH}_x^+ / \text{SnOH}_x^+$.

Figure 4.32: Ionogram of stannane (a) and oxygenated stannane (b) and the ratio of both (c) before (until 5050 s) and after (after 15 100 s) exposure to oxygen (O_2); LTOF; native ions.

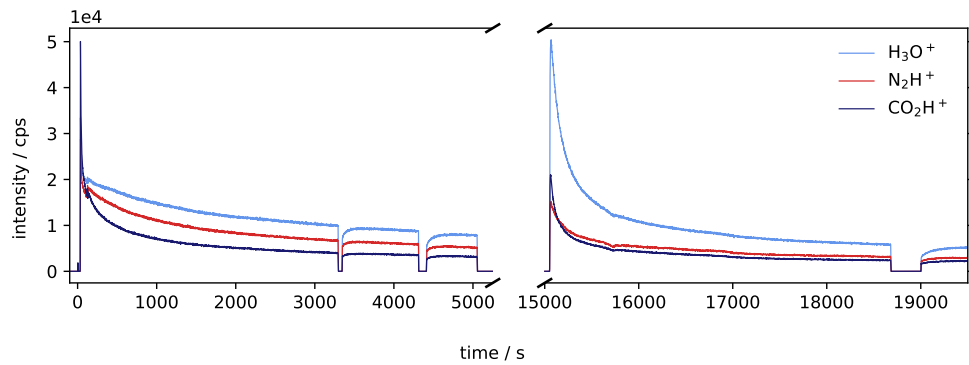
4 Results & Discussion

or both. The influence of oxygen is studied in two different experiments in which the tin target is in the PC. In the first experiment, the chamber was evacuated (1.1×10^{-8} mbar) and purged several times with hydrogen and the plasma is then ignited at 1.2×10^{-1} mbar. After 5000 s the signal is assumed to remain constant after the initial fast increase and subsequent exponentially decay phase. The system was evacuated again and then filled with a gas mixture containing 1000 ppmV O_2 in H_2 to approximately 1 bar. The tin was exposed to this mixture for 90 min before the chamber was evacuated again. The hydrogen pressure was adjusted to 1.2×10^{-1} mbar and the plasma was ignited. While the plasma is active, native ions from the plasma volume were sampled with the LTOF.

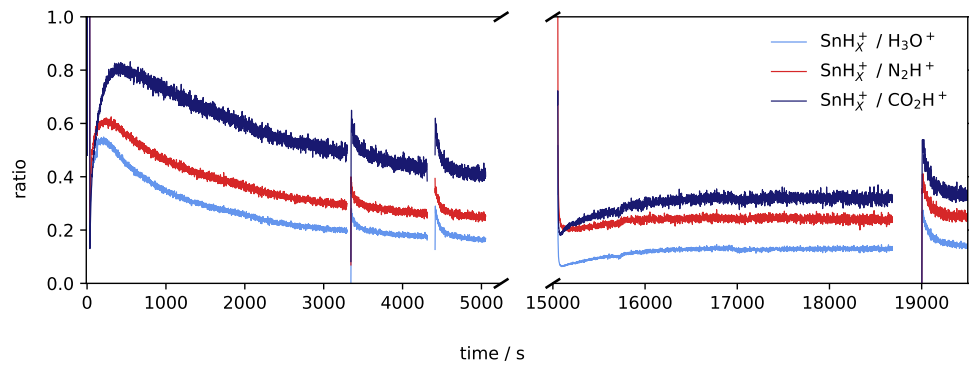
Figure 4.32 illustrates the progression of the EICs of SnH_X^+ (fig. 4.32a) and $SnOH_X^+$ (fig. 4.32b) in this experiment. Upon ignition of the plasma (at 0 s), the described effect appears again (initial maximum, 1.1×10^4 cps, exponential decay to a constant value, approx. 1.5×10^3 cps). During the run, the plasma is temporarily switched off twice (at 3200 s and 4300 s) and thus the signal drops to 0 cps but returns directly to the original value after the plasma is re-ignited. After exposure to oxygen and pumping (5050 s to 15100 s) and H_2 refill, the signal climbs to a second maximum (8.0×10^3 cps), and the decays back to the lower, constant value in much shorter time. Switching the plasma off and on again results in a drop to 0 cps and a rise again to the constant value. Thus, exposure of tin to oxygen causes a temporally limited but large increase in the etching rate after the plasma is turned on. This event is visible both in the ions from stannane and those from oxygenated stannane. However, if the second peak is disregarded, it appears as if the exponential trend in the first part of the measurement continues. The exposure only led to a briefly increased etch rate.

The abundance ratio of $SnH_X^+ / SnOH_X^+$ (cf. fig. 4.32c) may be an indicator of a possible shift of one species to the other. In the first part of the measurement there is a short drop of the ratio at the point where the maximum is located in the ionograms. A lower value corresponds to a larger fraction of $SnOH_X^+$. However, after a short period of time, the ratio change follows a constant trend, while the EICs progress through the exponential decrease. The ratio gradually becomes noisier as all signal intensities decrease. After oxygen exposure, the second part of the measurement reveals a peak in the ratio, indicating again a shift in the fractions of the species towards SnH_X^+ . This time, however, it takes longer to return to a constant value. Generally, the ratio is elevated, i.e. higher SnH_X^+ fractions is present. Thus, the exposure of tin to oxygen results in a temporarily significantly increased etch rate and a moderate shift of $SnOH_X^+$ to SnH_X^+ , which is currently not understood.

4.7 Initial etching phenomenon



(a) Ionogram of H_3O^+ , N_2H^+ and CO_2H^+ .



(b) Ratio of SnH_x^+ with H_3O^+ , N_2H^+ and CO_2H^+ .

Figure 4.33: Ionogram of different plasma species (a) and the ratio of stannane and these (b) before (until 5050 s) and after (after 15 100 s) exposure to oxygen (O_2); LTOF; native ions.

In addition to the tin species, there are many others plasma-generated species that are detected as native ions. The progressions of three of these species (H_3O^+ , N_2H^+ and CO_2H^+) are plotted in fig. 4.33a (hereafter referred to as plasma species).

At first glance, the ionograms look similar to those of the stannane and oxygenated stannane, but there are differences. The initial peaks upon plasma ignition are significantly sharper and collapse within a few seconds. This short effect appears to be directly associated with the ignition and could be caused by the formation of the plasma potential before equilibrium is reached. The two times when the plasma is temporarily turned off (at 3200 s and 4300 s), the EICs are not immediately returning the the value when the plasma was turned off, but need several seconds. After oxygen exposure, however, the subsequent

4 Results & Discussion

peaks have a different shape as compared to the initial peak. The decrease from the maximum is flatter and occurs over a longer period of time. It is noticeable that especially the ions with oxygen atoms respond more strongly to the exposure. The second maximum of H_3O^+ is even higher than the first maximum. The plot for CO_2H^+ after exposure shows a similar trend as in the first part of the experiment, but with a generally increased signal intensity. N_2H^+ on the other hand is hardly affected by oxygen exposure, the overall signal intensity is even below that of the first part with a small second peak, which quickly drops to constant values. The nitrogen originally present was probably displaced from the PC by pumping and flushing with oxygen and hydrogen.

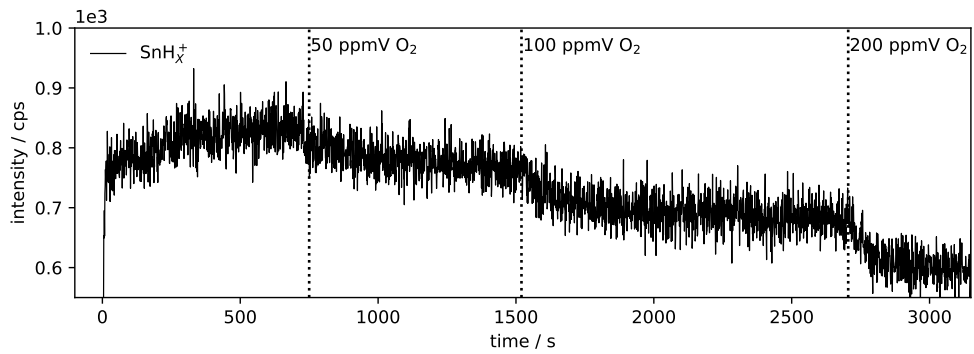
In order to assess the difference of the temporal evolutions of these plasma species (fig. 4.33a) and stannane (fig. 4.32a), the $\text{SnH}_x^+ / (\text{H}_3\text{O}^+, \text{N}_2\text{H}^+, \text{CO}_2\text{H}^+)$ ratios are presented in fig. 4.33b. It is evident that the EICs of the plasma species and tin species are different. Within the first 500 s, the ratio rises to its maximum before slowly decreasing over the entire first phase of the experiment. A large ratio corresponds higher stannane signals, and thus higher etch rate. The decrease in the ratio is due to the greater decrease in the EIC of stannane. The slow increase of the ratios after exposure corresponds to a higher signal intensity of plasma species than tin species. This is seen clearly in the case of the oxygen-containing compounds (H_3O^+ and CO_2H^+).

In summary, the comparison described here suggests that the ignition of the plasma and the time briefly after influence the formation of native ions. However, this burn-in phase of the plasma cannot describe the behavior of the ionic stannane fragments and the etching process in general. Consequently, there has to be another, so far not understood process, which directly affects the etching mechanism and the formation of stannane. Furthermore, these experiment do not clarify whether the adsorbed oxygen on the surface affects heterogeneous surface chemistry or is also conveyed by the plasma into the gas phase and initiates corresponding gas phase reactions. It is also conceivable that the effect on the tin species is caused by heterogeneous, oxygen-induced processes while the effect on the other plasma species is via homogeneous gas phase reactions. Moreover, it remains unclear whether oxygen is participating as O atoms, O_2 or even H_2O , respectively, or as the corresponding ions.

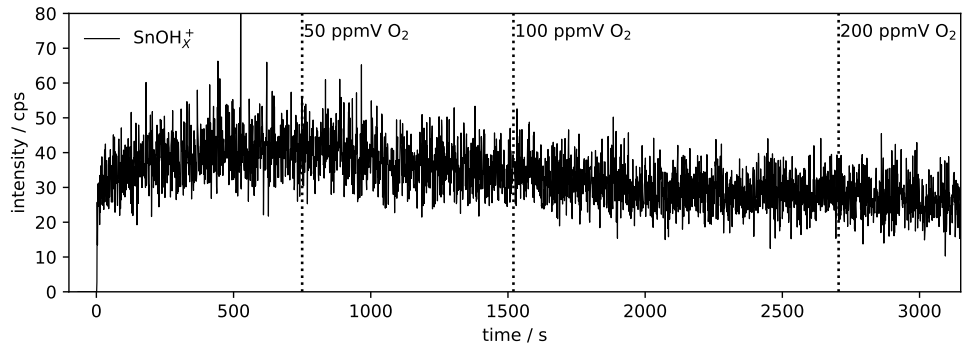
4.7.3 Addition of oxygen

In order to investigate if and how oxygen in the gas phase affects the plasma-induced chemistry and, in particular, the etching process, O_2 was added to the hydrogen feed at various concentrations while the plasma was running. Figure 4.34 summarizes the EICs of

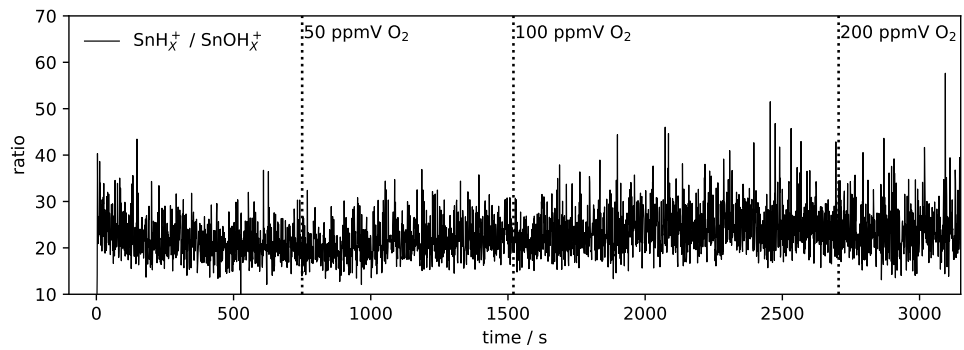
4.7 Initial etching phenomenon



(a) Ionogram of stannane (SnH_X^+).



(b) Ionogram of oxygenated stannane (SnOH_X^+).



(c) Ratio of $\text{SnH}_X^+ / \text{SnOH}_X^+$.

Figure 4.34: Ionogram of stannane (a) and oxygenated stannane (b) and the ratio of both (c). The mixing ratio of O_2 in H_2 and the time of addition are marked in the plots; LTOF; native ions.

4 Results & Discussion

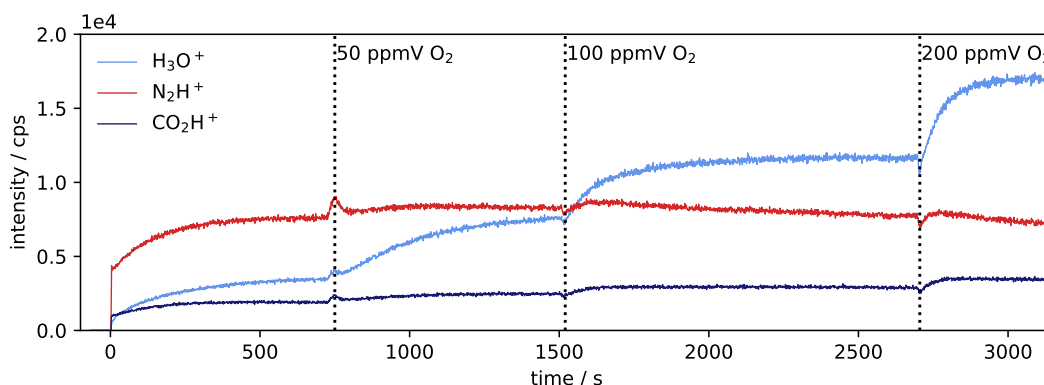


Figure 4.35: Ionogram of H_3O^+ , N_2H^+ and CO_2H^+ . The mixing ratio of O_2 in H_2 and the time of addition are marked in the plots; LTOF; native ions.

the stannane and the oxygenated stannane signals and the ratio of the two in dependence of the O_2 mixing ratio. The mixing ratio of O_2 in H_2 and the time of addition are marked in the plots. During the initial 750 s, only hydrogen was introduced into the plasma chamber (PC). Since the Sn target was not in contact with ambient air prior to the experiment and was etched previously in the hydrogen plasma, the characteristic peak as discussed in section 4.7.1 does not occur upon ignition of the plasma. However, for SnH_x^+ and SnOH_x^+ , a settling time is observed. Before the addition of oxygen, a constant signal intensity is recorded. Once 50 ppmV of oxygen is present in the plasma, the EICs decrease for the first approximately 300 s before becoming constant. This effect is even more pronounced when the oxygen mixing ratio is increased to 100 ppmV and 200 ppmV, respectively. The ratio shows that the relative signal decrease is the same for both stannane and oxygenated stannane (cf. fig. 4.34c). The ratio remains nearly constant during the entire experiment and is not influenced by the oxygen mixing ratio. It is concluded, that the presence of oxygen inhibits the formation of stannane. Furthermore, the results suggest that no reaction channels exist between stannane and oxygen to the oxygenated stannane, otherwise a shift between these species should occur.

In contrast, the results (fig. 4.35) for oxygen-containing plasma species (H_3O^+ , CO_2H^+) show a clear influence of O_2 . After an initial settling period, a directly proportional dependence on the oxygen mixing ratio on the signal intensities is observed. As expected, particularly the H_3O^+ signal responds strongly to the addition of oxygen, as most probably water or water related species (proton bound clusters etc.) are formed. It is noticeable that

when the oxygen concentration changes, it takes several hundred seconds for the signal to become constant again. This suggests that surface adsorptions causes this effect. The surface coverage with water or water species may change until the participating gas phase constituents are in equilibrium with corresponding surface bound compounds. The EIC of CO_2H^+ also increases proportionally with increasing oxygen mixing ratio, but to a much lesser extent. In addition, the signal responds much more swiftly to changes of the gas composition than the signal of H_3O^+ . As a result, wall effects do not occur, or only to a minor extent. N_2H^+ as a non-oxygen-containing ion is unaffected by O_2 addition. After the settling phase, even a minor but steady decrease of the signal intensity is observed.

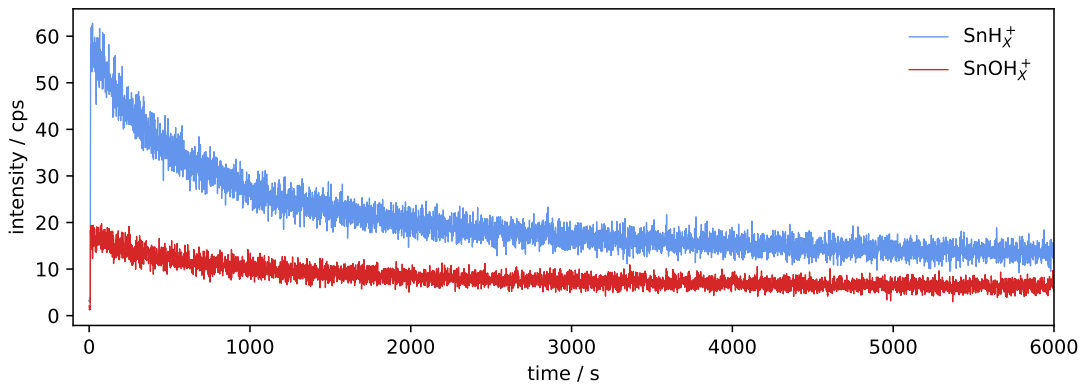
Previous experiments with synthetic air (20.5% O_2 , 79.5% N_2) in H_2 revealed strong effects on the plasma itself due to the significantly increased oxygen content. Oxygen can capture low energy electrons, so the quasi-neutrality of the plasma is disturbed. Visually, this is noted by a decrease in the plasma light emission intensity. As more oxygen is added, the plasma volume darkens and recesses to the electrode. The disruption of the hydrogen plasma by oxygen leads to a reduction of reactive hydrogen, which in turn means that less stannane is formed. This also affects the formation of other plasma species, such as H_3O^+ and CO_2H^+ .

4.7.4 Tin oxide as target

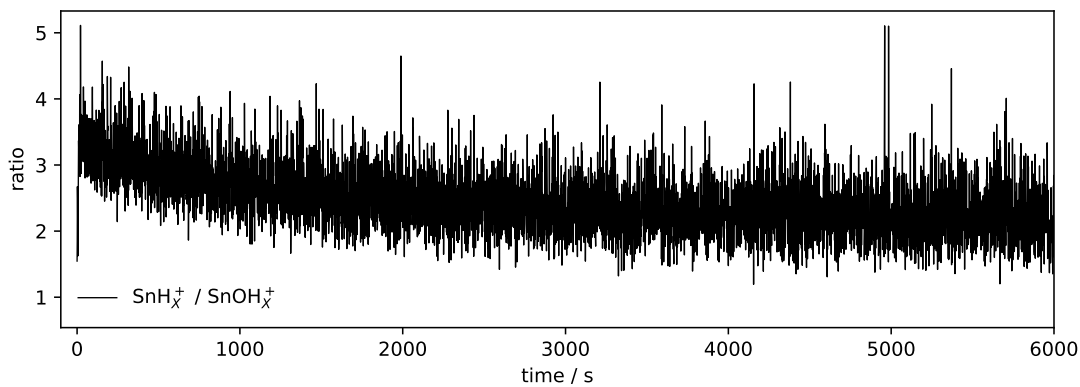
The previous measurements demonstrate that in the case of tin, the event may not be caused by gas phase reactions, but rather heterogeneous reactions at the surface. Tin is oxidized to tin oxide by oxygen, or by water formed by reaction of oxygen with H_2 at the surface. In order to investigate the extreme scenario of a completely oxidized tin surface, SnO_2 (synthesis described in section 3.7.2) was prepared and treated with a hydrogen plasma inside the plasma chamber.

The EICs of SnH_X^+ and SnOH_X^+ (cf. fig. 4.36a) recorded with the SnO_2 target show a similar temporal evolution during plasma ignition to that of the tin target (cf. fig. 4.31 and fig. 4.32). It takes about 4000 s for the signal to tail off, as observed before. However, a significantly lower number of ions per second is detected with a similar total target area exposed to the plasma. The maximum of the SnH_X^+ signal is about 2.5 orders lower than the maximum of the EIC of SnH_X^+ in fig. 4.31. Most remarkable is the change in the ratio of SnH_X^+ to SnOH_X^+ , which is initially around 3.2 and drops to around 2.5 after 4000 s. This means that there is significantly more SnOH_X^+ relative to SnH_X^+ present than in any

4 Results & Discussion



(a) Ionogram of stannane (SnH_X^+) and oxygenated stannane SnOH_X^+ .



(b) Ratio of SnH_X^+ and SnOH_X^+ .

Figure 4.36: Detected native ions of SnO_2 in H_2 plasma; LTOF; native ions.

previous experiment. Furthermore, during the 4000 s the ratio shifts further in favor of SnOH_X^+ .

Based on the work of Yamazoe et al.[88] it appears that O_2 , H_2O and H_2 on SnO_2 surfaces form reactive species as adsorbates even at lower temperatures. Different species can be formed and remain adsorbed on the surface, depending on the conditions. In particular, species such as O^- and OH^- strongly influence the surface chemistry. In analogy to zinc (Zn), it is speculated that even neutral H_2 is capable of reducing SnO_2 or SnO to the pure metal or further to SnH (as pre-cursor of stannane), at the same time OH is formed[88, 110]. The reactive hydrogen species in the plasma are no less reactive than surface bound H_2 and are equally capable of oxide reduction. Thus, even with pure hydrogen and a clean

target surface, an at least partial coverage of the SnO₂ surface with various H, O, OH and H₂O species can be assumed. This would explain the observed behavior of the initial maximum. Nevertheless, the overall intensity is significantly lower than recorded with pure tin metal. This could be due to the fact that the incident H radicals are first consumed for the reduction of the tin oxide before Sn–H bond formation can occur. The existence of a Sn–O bond in the case of SnO₂ could explain why there are much larger SnOH_X⁺ signals relative to the SnH_X⁺ signals in the spectra. However, the exact mechanism of formation of stannane and oxygenated stannane is not sufficiently understood to draw further conclusions.

4.8 Quartz crystal microbalance measurements

The hydrogen plasma driven etching of tin or etching processes in general are quantifiable upon using the quartz crystal microbalance (QCM) as mass change sensitive device. The principle of operation (cf. section 2.7) and the instrumentation are described in section 3.4.

4.8.1 Sensor characterization

For the quantitative experiments it is essential to characterize the response of the electronics and the sensors under plasma conditions and to determine any additional effects on the sensors frequency response. An uncoated clean QCM sensor was mounted inside the plasma chamber (PC) above the active plasma volume. The sensor was connected via feedthroughs to the electronics of the QCM, which was located outside the chamber.

To ensure that the frequency reading remains constant over a longer period of time and there is no frequency drift due to intrinsic effects, long-term tests were carried out in vacuum and with hydrogen at standard plasma pressure (1.2×10^{-1} mbar), with the plasma switched off. The results of 20 h long recordings in both cases showed no frequency drift and only a marginal deviation of ± 4 Hz at a sensor resonance frequency of 10 MHz, equivalent to $\pm 4 \times 10^{-5}$ %. The detection system is therefore well suited for the experiments. As the experiments were carried out under air conditioned laboratory conditions, the sensor temperature is assumed to remain constant.

The effect of the plasma or plasma species generated on the clean sensor and therefore on the frequency response was investigated next. Since the sensor acts as an antenna for the electric fields generated by the RF driver, it is not possible to measure the frequency as long as the plasma is ignited. In the worst case, the 100 W of the plasma driver would be completely captured by the QCM, causing irreversible damage to the electronics. However,

4 Results & Discussion

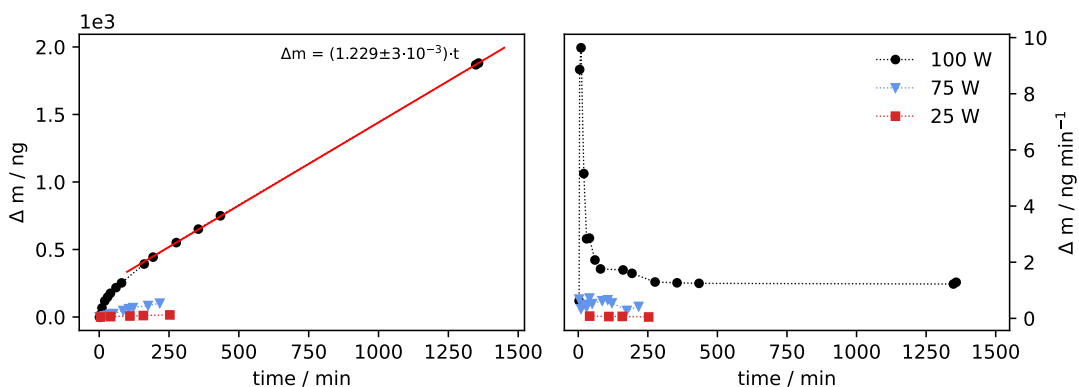


Figure 4.37: Clean QCM sensor in H_2 plasma (1.2×10^{-1} mbar) at different plasma power. Left: mass change over time; Right: mass change rate over time.

in order to obtain a suitable temporal resolution, a discontinuous technique was used by periodically switching off the plasma to take a QCM reading. For each reading, after a settling time for the QCM electronics of 5 min, a one-minute averaged frequency value was recorded. Figure 4.37 presents the mass change of the gold sensor as calculated using the recorded change of the resonance frequency of the crystal oscillator. The markers correspond to the individual frequency recordings connected by the dotted lines provide an overview of the temporal evolution of the sensor's response. It is immediately apparent that the relative mass change of the sensor is a function of time. The experiment with 100 W was followed by 75 W and 25 W, respectively, with the same sensor. During the first 60 min at 100 W, a maximum of 9.6 ng/min mass change rate is quickly reached and then drops as sharply. Subsequently, the ratio remains almost constant at around 1.3 ng/min. Since this initial maximum in the mass change rate only occurs in the 100 W measurement as the first of the three runs, it is reasonable to assume a surface conditioning upon the first exposure to the H_2 plasma. As the conditions do not change thereafter, no further initial conditioning takes place. Apart from this transient behavior, the sensors record a constant, and thus linear, mass increase. This demonstrated by an over 22 h (1358 min) long experiment of sensor plasma exposure at 100 W RF power: A fitting function applied to the data yields a linear relationship over a period of 1200 min with very small deviations. The slope of the straight line (1.229 ± 0.003) matches the mean mass change rate in the same time interval (cf. fig. 4.37). In addition, the mass change rate is directly related to the plasma power: The higher the power the plasma is operated at, the higher the mass

Table 4.11: Rates of mass gain due to the hydrogen plasma at different plasma powers.

| plasma power / W | mass change rate / ng min ⁻¹ |
|------------------|---|
| 100 | 1.229 ± 0.003 |
| 75 | 0.395 ± 0.021 |
| 25 | 0.051 ± 0.004 |

increase per time (cf. table 4.11). This result strongly suggests that the mass increase is caused by plasma-generated species, and that the amount of sensor captured species is directly related to the power of the plasma. Hydrogen has unique properties in terms of diffusion into metals, especially when atomic hydrogen is involved. Interstitial diffusion, in combination with the quantum tunneling, leads to an exceptionally high level of mobility of hydrogen atoms in metals and thus to a general ability to incorporate hydrogen into the metal structure[111]. These non-etching processes effects need to be considered in further experiments. Furthermore, all sensors were exposed to the H₂ plasma for at least 45 min to clean and condition the sensor's active gold surface.

4.8.1.1 Hydrogen etching of electroplated tin

The initial hydrogen etching experiments were carried out on electroplated sensors, i.e., only the gold electrodes are coated, leaving the quartz surface unaffected. For the results shown in fig. 4.38, two sensors (denoted as S-1 and S-2) were prepared and coated with Sn at the same time to ensure the greatest possible degree of comparability. To further ensure the same conditions during hydrogen plasma etching, both sensors were mounted in adjacent positions within the plasma chamber. After each plasma etching cycle, 2 min to 3 min were waited to allow the sensors to cool down, which may have been thermally heated by the plasma interaction. This was done to minimize the effect of temperature change on the sensor's resonant frequency. The left plot in fig. 4.38 displays the mass loss on the sensor over the period of time the plasma is ignited. Both sensors show an initial large mass change within the first 5 min, tailing off over the following 95 min. While both sensors have a very similar mass loss during the first plasma cycle (S-1: 316.8 ng; S-2: 322.4 ng), a pronounced difference is noticeable during the further course of the experiment. However, the general trend remains the same. The difference between the sensor responses is also clearly visible in the plot on the right of fig. 4.38. Sensor S-2 was exposed to an overall

4 Results & Discussion

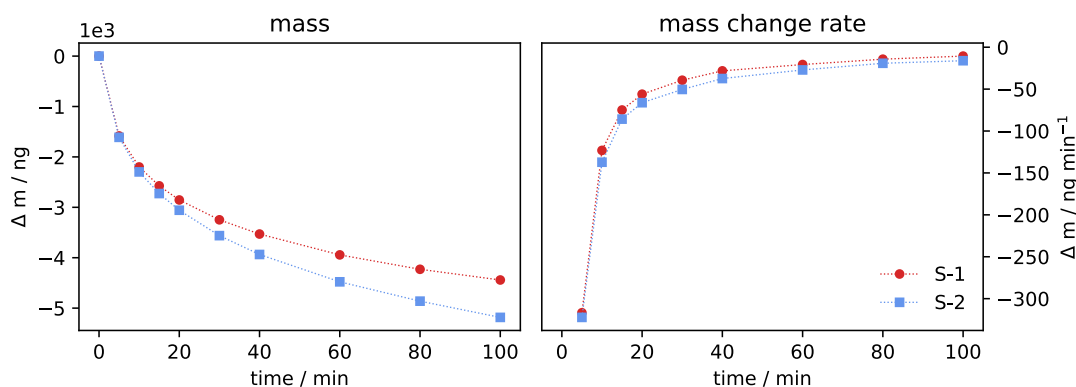


Figure 4.38: Comparison of etching of two identical electroplated QCM sensors (S-1 and S-2). Hydrogen plasma (1.2×10^{-1} mbar), 100 min. Left: mass change over time; right: mass change rate over time.

Table 4.12: Measured change in the mass of the QCM sensors (S-1 and S-2) and derived values. Hydrogen plasma (1.2×10^{-1} mbar), 100 min.

| change of | sensor S-1 | sensor S-2 |
|--------------------------|-----------------------|-----------------------|
| frequency / Hz | 3557.6 | 4152.0 |
| mass / ng | 4441.9 | 5184.0 |
| mole / nmol | 37.4 | 43.7 |
| volume / mm ³ | 6.11×10^{-4} | 7.14×10^{-4} |
| layer height / nm | 21.6 | 25.2 |
| numbers of layers | 99.7 | 116.3 |

higher etch rate than sensor S-1 of around 5 ng/min as compared to 9 ng/min over the entire duration of the experiment. The amount of material etched (most likely tin metal) during the 100 min plasma treatment, i.e. the mass loss, is listed in table 4.12 for both sensors. It is important to note that the calculations of volume, layer height and number of layers is based on idealized tin crystals. Irregularities and the effect of layer growth on the surface are not taken into account. From visual examination of the surface (cf. fig. 3.8 and fig. 3.8) that it is not uniform. The calculations are primarily ballpark estimates. During the experiment, 4441.9 ng or 37.4 nmol tin were etched from sensor S-1. Provided ideal

conditions, this corresponds to the removal of 99.7 layers of tin for a sensor diameter of 6 mm (cf. section 3.4). According to eq. (R 2.14), one atom Sn is converted to one molecule SnH_4 by reacting with plasma-generated H radicals. Consequently, 37.4 nmol of stannane were formed by hydrogen etching, which corresponds to a gas volume of 9.1 cm^3 at standard temperature and pressure (STP), assuming ideal gas behavior.

Although the results obtained with the two sensors, which were coated and etched at the same time and in the same way, are comparable and follow a similar trend, this experiment demonstrates that quantifiable conclusions can only be drawn within one measurement and only for one sensor in each case.

4.8.1.2 Etching vs. sputtering

In addition to the observed hydrogen etching of Sn by H radicals, ions accelerated in the alternating electric RF field driving the plasma may cause sputtering processes depending on their mass and kinetic energy[112]. In order to rule out the possibility that the loss of Sn in the previous experiments was mainly caused by sputtering, two sensors electroplated with tin as in the previous experiment were exposed to an Ar plasma and a He plasma, respectively. Both gases are readily producing plasmas upon RF excitation; as they have significantly different masses (He: 4.003 u and Ar: 39.948 u [27]), plasma sputtering rates should thus also differ significantly. In fig. 4.39 the mass change (left) of the sensors and the corresponding rate (right) are plotted.

The results obtained with S-2 in the previous hydrogen plasma exposure experiment (cf. section 4.8.1.1) are included for comparison. In a noble gas plasma, the mass change behavior is completely different as in a hydrogen plasma: In the initial plasma exposure period, a mass loss rate of 137.5 ng/min in the Ar plasma and 57.9 ng/min in the He plasma is observed; with continued exposure to the plasmas, fluctuating rates of $(-1.7 \pm 2.0) \text{ ng/min}$ for argon and $(-1.9 \pm 2.2) \text{ ng/min}$ for helium prevail, with a small but steady loss of mass on the sensor. The fluctuation of the rate is clearly visible and in some cases it reaches positive values, corresponding in an increase in mass. In addition to sputtering (removal of material by bombardment of the surface by ions) there are other effects such as ion implantation[113] or ion beam deposition[114]. In the present experiments, ion implantation plays only a minor role due to the low kinetic energy of the impinging ions. Furthermore, the comparatively low removal rate could be due to the combination of the mass increase due to the low impinging rate of argon or helium atoms and the sputtering rate.

A previous experiment with a clean uncoated gold sensor placed in an argon plasma demonstrates that after an initial mass loss, the mass loss rate fluctuates around 0 ng/min.

4 Results & Discussion

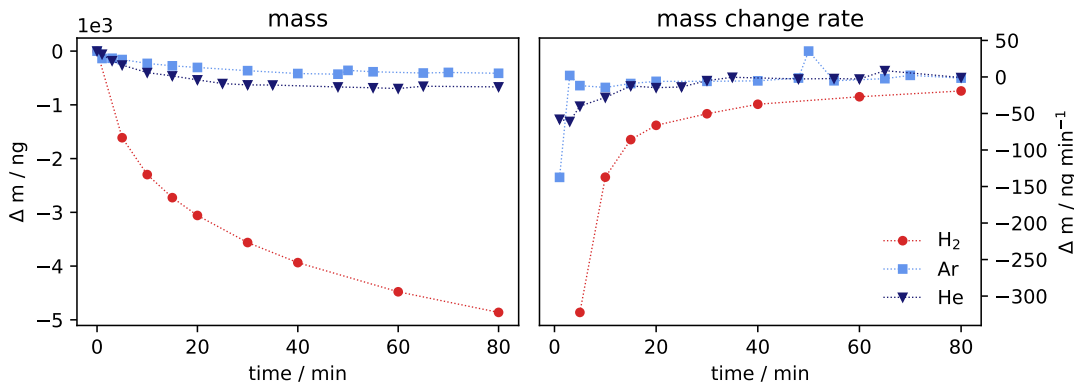


Figure 4.39: Comparison of different plasmas (H_2 , Ar, He) with identical electroplated QCM sensors. 1.2×10^{-1} mbar, 80 min. Left: mass change over time; right: mass change rate over time.

The difference in the mass loss rate of the uncoated and the tin-coated sensor correlates with both the metal and the thickness of the metal. The QCM gold electrode consists of 10 nm Ti and 200 nm Au (cf. section 3.4). This metal layer is thus significantly thinner than the Sn coating. The larger metal volume more efficiently accommodates the impinging atoms during implantation, resulting in a constant increase in mass. No further investigation was made to determine if the rate is proportional to the thickness of the metal coating or whether it becomes insignificant above a certain thickness due to the limited penetration depth of the impinging ions.

The results obtained with the two noble gases differ only slightly. Minor differences are probably due to different coating properties, which cannot be avoided even upon simultaneous electroplating. In the helium experiment, there is a convergence to the final rate within the first 20 min. The reason for this is not evident from the measurement. Apart from the first plasma cycle, which is most likely a removal of impurities, there is no apparent trend to be seen. As a result, there is no change to the surface, or more specifically, no change that affects the sputtering. Only hydrogen adds a chemical factor to the sputtering effect, which is limited though due to the low molecular mass of H/H_2 . The chemical formation of stannane is therefore a significantly more efficient and effective process than sputtering in the ion kinetic energy range occurring in the plasmas used. In summary,

4.8 Quartz crystal microbalance measurements

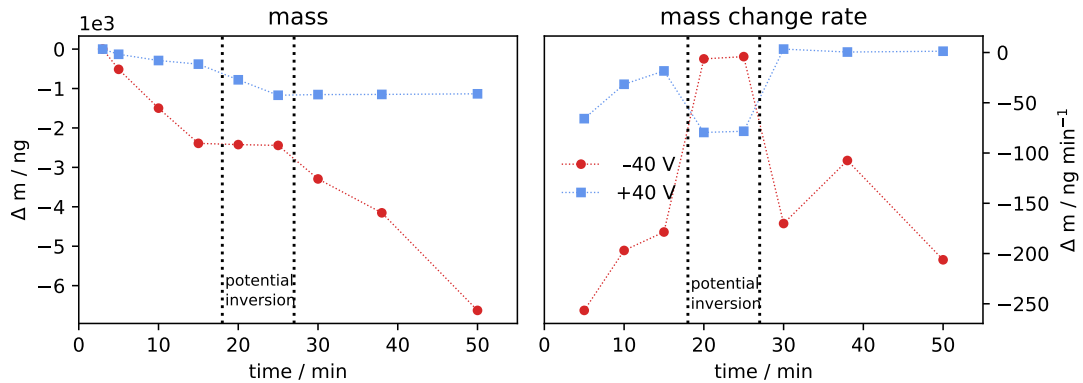


Figure 4.40: Comparison of two identical electroplated QCM sensors with different applied potentials (+40 V, -40 V); The potential is inverted within the dotted lines. Hydrogen plasma (1.2×10^{-1} mbar), 50 min. Left: mass change over time; right: mass change rate over time.

over the period of 80 min of plasma exposure, 4861.8 ng were ablated/ etched in hydrogen plasma, 412.9 ng in argon, and 666.1 ng in helium. Hydrogen etching is therefore much more effective by about one order of magnitude.

4.8.1.3 Influence of potentials on electrodes

The results of the studies reported by Elg et al. suggests that the limiting factor of the etch rate is not the quantity of available H radicals, but the ion energy flux[45–47]. This process is described in more detail in section 2.4.1.2. This principle could be exploited by applying a repulsive or attractive potential to the electrodes of the QCM sensor during the plasma exposure phase. An experiment was designed with two similar electroplated Sn-coated QCM sensors positioned equidistant from the plasma. A potential of +40 V was applied to the coated electrode of one sensor and -40 V to the other. The behavior of the two sensors is not directly comparable due to possible differences in the Sn coatings. However, in order to see a possible effect, the potential was inverted for two cycles during the experiment, so any effect should be at least cancelled or reversed. This indicator should be clearly visible in the respective mass change rate.

Figure 4.40 shows the progression of the mass loss over time with the two different potentials applied, where the potentials are always referenced to ground. It is clearly discernible that a negative bias voltage is leading to a higher etch rate. After 15 min, 2390.9 ng at

4 Results & Discussion

-40 V and 381.1 ng at +40 V were etched, which is about one order of magnitude more tin removal with the negative bias. The significantly higher etch rate is also evident in the right-hand plot. Reversing the potentials leads to an interesting result: the rate on the sensor with the previously -40 V bias drops from -189.6 ng/min to only -4.1 ng/min. On the other hand, the etch rate on the sensor with the previously +40 V bias increases from -18.3 to 79.5 ng/min. As effect of the inverted bias potentials is more than evident, the etch rates are not directly responding to the potential change. After the returning the original bias at 25 min, the rates return as well to a similar etch rate value as they were before the change. The mass change rate on the sensor with the +40 V bias also reveals another effect: it becomes positive, i.e. the mass on the sensor increases. This is in line with the trend that was already apparent prior to the change of the bias potential. Why a repulsive potential should inhibit the stannane formation to such an extent that there is no removal of tin and even an increase in mass is observed, remains unclear. Which species are responsible for the mass increase also remains uncertain, although an implantation of neutral or negatively charged (hydrogen) ions appears to be plausible.

In any case, the experiment shows that even a bias potential of only 40 V is significantly impacting on the etch rate of tin in a hydrogen plasma.

4.8.2 Additional methods of sensor coating

In addition to electroplating, which tends to create thicker, irregular layers on the QCM sensor, several other methods are applicable. The methods used in this work are described below.

4.8.2.1 Sensor coating via thermal evaporation

A number of QCM sensors have been coated with tin by means of physical vapor deposition (PVD), or more precisely by means of thermal evaporation. Compared to electroplating, this method promised to produce a different surface morphology and thinner layers. The cleaned bare sensors were mounted in a vacuum chamber and a weighted tin sample was evaporated through resistive heating. Taking into account the distance between QCM sensors and the crucible, the angle and the amount of evaporated tin, a resulting layer thickness of 10 nm is calculated.

The mass change rate of such a coated sensor when exposed to a hydrogen plasma is presented in fig. 4.41. The shape of the curve is largely different from that obtained with the electroplated sensors. Within the first minute of plasma treatment, a significant

4.8 Quartz crystal microbalance measurements

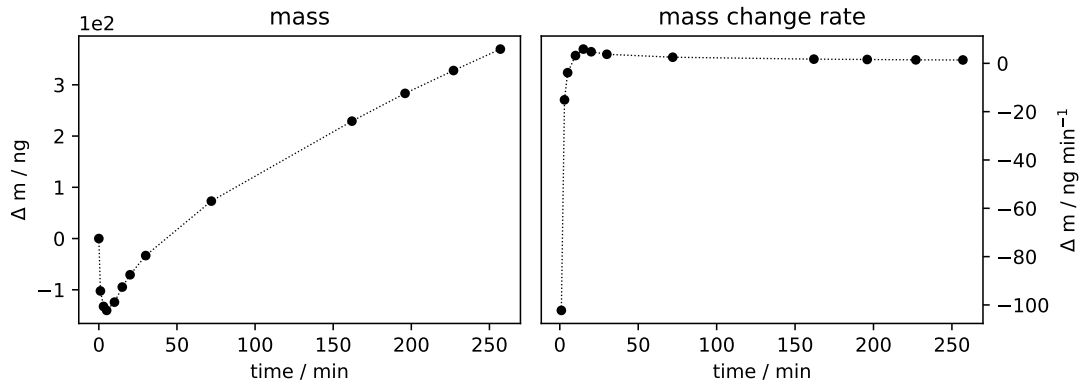


Figure 4.41: Tin coated QCM sensor via thermal evaporation. 10 nm layer thickness (calculated); hydrogen plasma (1.2×10^{-1} mbar), 257 min. Left: mass change over time; right: mass change rate over time.

mass change occurs, although the rate of mass change decreases in the following minutes. Between 5 min to 10 min the rate changes from negative to positive, which means that the mass is increasing. The etch rate reaches its highest value at 15 min, and then it constantly decreases again to a value of 1.4 ng/min. After approximately 50 min, the sensor carries the same mass as before the plasma treatment and the mass continues to increase upon further exposure to the plasma. The increase in mass is linear from 100 min to the end of the experiment, just as it was observed with an uncoated sensor. The reason for that will most likely be the same. In other words, two processes operating in opposite directions take place: hydrogen etching of the coated tin and presumably the adsorption or absorption of hydrogen atoms in/into the material of the sensor. As the respective individual mass change rates can only be measured as a total rate, it is difficult to determine the amount of tin remaining on the sensor. Assuming that there was an ideal 10 nm thick uniform layer of tin on the sensor, the calculated mass is 2069 ng. However, the sensor has only lost 140.2 ng in the best case. This is not plausible, even taking into account the opposite increase in mass due to hydrogen uptake. Due to the small amount of evaporated tin, the tin mass applied to the sensor cannot be predicted exactly. The predictions of the etching behavior for sensors coated in this way are not reliable. It would take several attempts and different coating thicknesses to arrive at more reliable numbers. Since electroplated QCM sensors are easier and quicker to prepare due to the simpler laboratory setup, so they are used for all subsequent measurements.

4.8.2.2 Sensor coating via stannane decomposition

Studying the decomposition of stannane (SnH_4) on surfaces is interesting from several perspectives. Firstly, the rate of mass increase on the sensor could be expected to correspond to the rate of decomposition of stannane and a change in this rate over time could be used to draw conclusions about the decomposition mechanism on surfaces. In this case, all relevant processes and their influence on the frequency measurement need to be known and quantifiable. Reactive coating of the surface using stannane additionally has the advantage of mimicking the real decomposition processes in lithography systems. Secondly, it would be feasible to obtain a thin coating on specific surfaces by decomposition of stannane. This decomposition most likely leads to the various layer growth processes already described (cf. section 2.4.1.1).

For such a coating experiment, the sensor was mounted 3 cm away from a curved piece of tin foil with a surface area of about 8 cm^2 oriented toward the sensor in the plasma chamber (PC). The principle idea of this experiment is that stannane is formed on the tin surface by interaction of plasma-generated H species, and then desorbs from the surface into the gas phase. Diffusional transport towards the surface of the sensor and decomposition of the SnH_4 then leads to the formation of a thin Sn layer on the QCM electrode. As shown in fig. 4.42, the mass of the sensor decreases by 50.1 ng within 1 min of plasma treatment. In the following 19 min, the mass change rate fluctuates around 0 ng/min, before becoming a constant positive value. In the initial period of time, adsorbates and purities are probably etched from the surface, after which the mass increase occurs. The rate remains constant over for more than 1000 min, representing a steady increase in mass.

This experiment (cf. fig. 4.42) is only one example of several to improve the understanding of the observed mass increase. Geometrical variations of the setup aimed to study different effects, such as the relative orientation (distance and angle) of the sensor surface to their tin foil or the common distance to the RF electrode. Taking all the rates obtained during the different measurements yields a mass growth rate of $(1.17 \pm 0.11) \text{ ng/min}$. This rate corresponds within its error limits to the determined rate of $(1.229 \pm 0.003) \text{ ng/min}$ from a clean uncoated sensor exposed to a H_2 plasma. This leads to the conclusion that the observed mass increase is not due to stannane or tin take-up but only to the effects caused by the hydrogen plasma itself. In theory, the proximity of the sensor to the surface of stannane formation should result in a interaction between the stannane and the sensor electrode. However, the etching rate is probably significant higher than the decomposition rate, or the quantity of H radicals in the gas phase is much higher than that of stannane. This results in a barely noticeable presence of additional tin on the gold electrode. For

4.9 Simultaneous measurement of QCM and LTOF

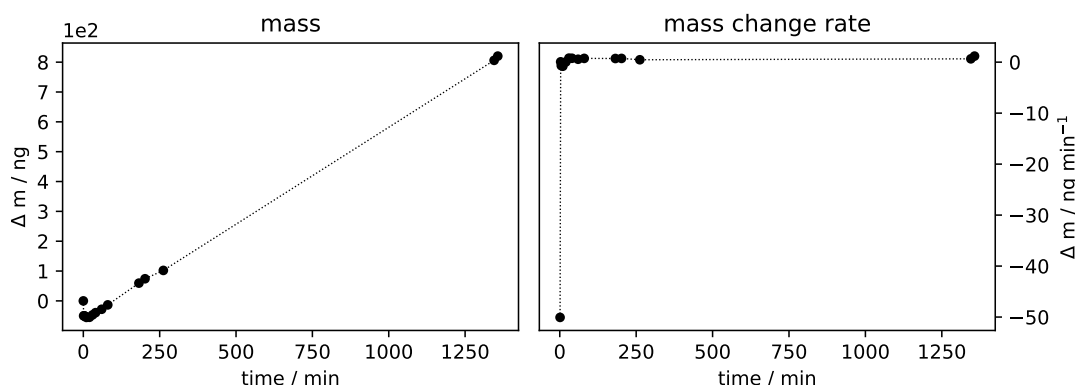


Figure 4.42: Stannane coating: clean QCM sensor 3 cm away from tin foil; hydrogen plasma (1.2×10^{-1} mbar), 1357 min. Left: mass change over time; right: mass change rate over time.

this type of coating, the gas phase stannane concentration has to be significantly larger. Results presented by Elg et al. suggest that stannane deposition is a rather slow process. Diffusion of the plasma generated stannane on the tin foil surface to the chamber walls is therefore more likely than decay on the QCM electrode[47].

One option could be the direct coating of metal surfaces using synthesized stannane samples. The amount of gas phase stannane would be much higher and because there is no plasma, no etching process would interfere.

4.9 Simultaneous measurement of QCM and LTOF

Compared to mass spectrometry, QCM measurements have the advantage of providing direct and quantitative results. The determination of native ions by the LTOF mass spectrometer could be directly correlated to the mass loss of the sensor if the stannane source is an electroplated QCM sensor. However, some assumptions and limitations have to be made for such a direct link between the measurement systems: it is assumed that only the hydrogen-driven etching process of tin and the hydrogen absorption on the QCM electrode surface are changing the resonance frequency of the sensor. Possible sputtering processes that do not lead to ionic tin species are ignored. Furthermore, in terms of mass analysis, either the native ions or the neutral molecules can be detected simultaneously with the QCM data. Geometries, pressures and potentials, for example, clearly affect the relevant

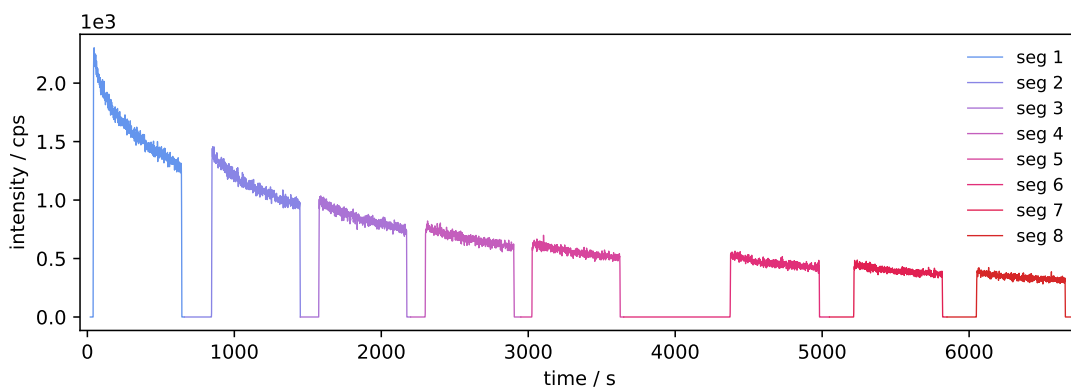
4 Results & Discussion

processes, as previous measurements have shown. Thus any correlation between the two data sets is, at this point, qualitative in nature only.

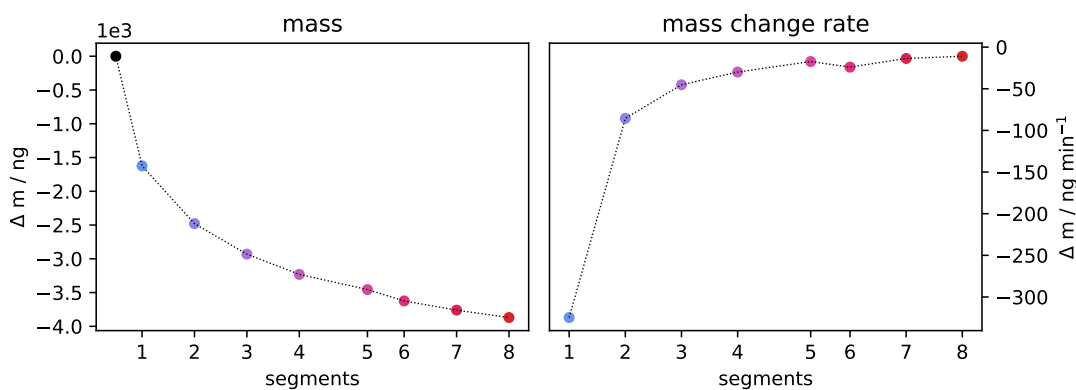
In the experiment, an electroplated sensor was mounted in the plasma chamber as before. The hydrogen plasma was ignited for 2 min before the start of the data acquisition. Actual recording started at time 0 s. Figure 4.43a displays the ionogram of the native tin hydride ions. The characteristic decay is clearly discernible: after an initial maximum, the signal intensity decreases exponentially with time until it slowly approaches a constant value. Every 10 min, the plasma was switched off to perform a QCM measurement. The period of time during which the plasma is operating will be referred to as a segment. It is noticeable that segment 2 starts with a slightly higher intensity than segment 1 ends. In the other segments, this does not occur or only to a minor extent. After evacuation, there may still be residual oxygen and water in the volume of the PC which affect the etching process. A total of 8 segments were recorded in 6750 s. The segments are color-coded for ease of reference. After switching off the plasma, a certain time was waited with the QCM measurement to ensure that the sensor has room temperature and was not still heated up by the plasma. The calculated mass differences after each plasma period and the resulting mass change rate are displayed in fig. 4.43b. The results are also color-coded in the same way as the ionogram. An initially high signal can be seen, which continuously decreases in the following segments. This is also noticeable in the mass change rate, which approaches about 10 ng/min from the initial 324.7 ng/min. This kind of progression is expected and consistent with the experiments described in previous chapters.

In order to relate the signal intensity of the native ions to the QCM mass loss data, the respective results are scaled to the respective segment. In fig. 4.43c, the sum of the LTOF counts and the mass loss on the sensor of the QCM are compared in a bar plot for each segment. In both cases, the trend is similar and in line with the previously described temporal evolution of the signals. The results for the individual segments are shown in table 4.13. The result that both the etch rate and the quantity of detected ionic tin hydrides follow a similar course supports the hypothesis that there are one or more processes that influence the etching rate directly and thus the quantity of formed stannane. Furthermore, previous experiments have shown that the process needs to be heterogeneous in nature and occur on the surface. However, the comparison of these results also show that the relative decrease of the signals with time is not identical. In addition to effects such as ion guidance efficiency and location of the sampling, it is important to point out that with

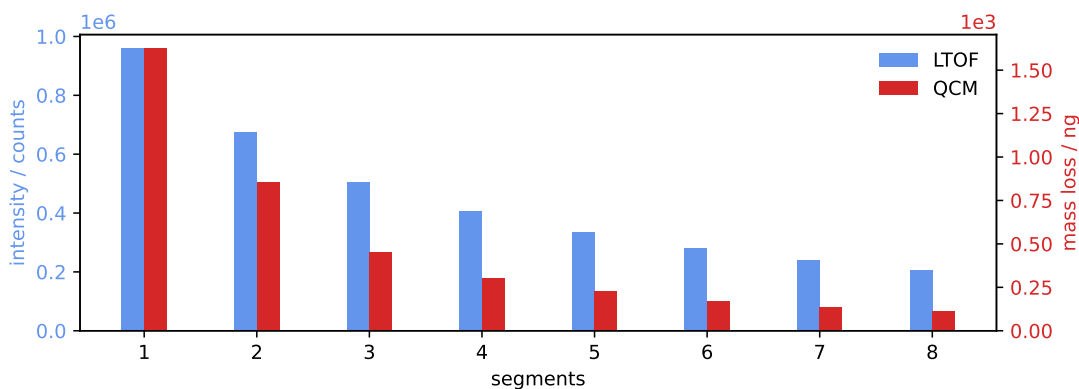
4.9 Simultaneous measurement of QCM and LTOF



(a) Signal intensity of tin species; LTOF.



(b) Mass change over time of an electroplated sensor; QCM.



(c) Comparison of the direct mass loss of the QCM with the signal intensity of the LTOF.

Figure 4.43: Simultaneous measurement of the QCM and the LTOF. Hydrogen plasma (1.2×10^{-1} mbar), 7350 min.

4 Results & Discussion

Table 4.13: Comparison of LTOF and QCM measurement results. Hydrogen plasma (1.2×10^{-1} mbar).

| segment | LTOF | QCM | | |
|---------|--------------------|--------------------|-------------------------|---|
| | intensity / counts | mass loss / ng | counts ng^{-1} | $\frac{\text{counts}_{theo}}{\text{counts}_{exp}^{-1}}$ |
| 1 | 9.58×10^5 | 1.62×10^3 | 5.90×10^2 | 8.59×10^9 |
| 2 | 6.75×10^5 | 8.55×10^2 | 7.90×10^2 | 6.42×10^9 |
| 3 | 5.06×10^5 | 4.52×10^2 | 1.12×10^3 | 4.53×10^9 |
| 4 | 4.05×10^5 | 3.00×10^2 | 1.35×10^3 | 3.75×10^9 |
| 5 | 3.34×10^5 | 2.25×10^2 | 1.48×10^3 | 3.42×10^9 |
| 6 | 2.80×10^5 | 1.68×10^2 | 1.67×10^3 | 3.04×10^9 |
| 7 | 2.39×10^5 | 1.36×10^2 | 1.75×10^3 | 2.90×10^9 |
| 8 | 2.06×10^5 | 1.10×10^2 | 1.88×10^3 | 2.70×10^9 |

this setup, either native ions or neutral species, but not both at the same time, can be detected by the LTOF. The amount of neutral stannane formed is therefore not included in the calculations, since only the native ions are recorded.

The table 4.13 contains estimates of the relationship between the two recorded signals systems in addition to the measured values. The ratio (counts ng^{-1}) of the signal intensity to the mass loss on the QCM sensor shows an increase from segment to segment. This means that the change between segments is greater at the beginning and becomes less and less significant as the experiment proceeds. During the 8th segment, the initially recorded maximum has nearly disappeared, allowing the assumption of a constant etching rate. The ratio between the LTOF and the QCM is 1.88 counts ng^{-1} of etched tin. For a direct comparison at the atomic level, the ratio of the theoretical intensity to the recorded intensity is used. The theoretical intensity is the maximum number of counts that were recorded if every etched tin atom on the sensor is captured and detected by the TOF analyzer. At a constant etch rate, the ratio is in the range of 2.70×10^9 , or in other words, for every tin ion detected, 2.70×10^9 tin atoms were etched from the surface. This also means that using this experimental setup on average at least this amount of stannane must be formed to be detected as 1 count with the mass spectrometer.

This low ratio can be partly explained by the geometric layout of the setup. Due to the low pressure, the Knudsen number is about 1 (assuming an ideal gas). In this region, the gas motion is characterized as Knudsen or free molecular flow. There is no contin-

uum flow in the direction of the transfer and the attractive potential for collecting ions does not extend far into the volume of the chamber. Assuming a point source of stannane and a spherical expansion, only $8.559 \times 10^{-3} \%$ of the particles reach the entrance lens of the hexapole ion guide. Furthermore, and as mentioned before, only the ionic species are taken into account. The total amount of detached tin is thus underestimated to an unknown amount. The experimental setup used here shows that for very small ion quantities, a carefully optimized experimental design is essential. Alternatively, instead of in-situ determinations, concepts for pre-concentrating stannane need to be studied.

Despite all limitations, the calculations presented are relevant for a general estimation of the ion capture efficiency. Furthermore, a conversion factor between the signal intensity of the LTOF and the amount of generated stannane or stannane species was derived, which is specific to set-up with the experimental conditions.

4.9.1 Comparison with literature data

References for the experiment and results described in the last two sections were found in the literature only in the work of Elg et al.[47]. Their setup and the experimental conditions are similar to those used in this work, but without the use of a mass spectrometer for the determination of the neutral gas and the ions. Using a QCM array detector, Elg et al. observed that the etch rate of tin with excited hydrogen is time-dependent. The etch rate is largest immediately after plasma ignition and decreases exponentially to a constant low etch rate. The reported behavior is in good agreement to that shown in fig. 4.38. Elg et al. investigations of the phenomenon have been the subject to a wide range of experiments. Indirectly mentioned is also the effect that exposing the tin coated QCM sensor to ambient air leads to a temporary increase of the etching rate. The magnitude of the effect depends on the length of air exposure. Re-deposition of the generated stannane, which in turn decreases the net etching rate, was also ruled out by several different experiments. The combination of mass spectrometry and QCM as described in this work confirms that this behavior is not just a superimposed effect of the weight determination on the sensor, since the same trend would not be seen in the mass spectra in this case. From the correlations in fig. 4.43 it is clear that there must something else that affects the etching rate.

Similarly, this literature study points out the effects of an oxid layer state present on the tin surface. However, a contrary rational to the one developed in this work is discussed. Their hypothesis is based on the premise that SnO and SnO₂ react markedly slower with excited hydrogen than Sn. The more tin oxide is residing on the tin Sn surface, the lower the etching rate. Thus, the initial etching rate will be determined by the fraction of exposed

4 Results & Discussion

pure tin. During the etching process, the areas of pure Sn become fewer, resulting in a correspondingly lower etch rate. This consideration is supported by XPS measurements, which show that the ratio of pure tin to oxidized tin shifts towards the oxidized species. Nevertheless, this does not explain why an exposure of the tin target to air again leads to a temporarily increased etch rate as demonstrated in fig. 4.32. Furthermore, the experiment indicates that an exposure leads to a small increase of the SnH_X^+ fragments relative to the SnOH_X^+ fragments.

The rationale of Elg et al. theory is that the plasma source initially in use was not sufficiently powerful for a high etch rate. The initial high etch rate was simply the removal of surface contamination. It has been repeatedly demonstrated in this work, that this is not the case. Instead, it is the surface-driven formation reaction of stannane that changes the reaction rate. However, in another setup, Elg et al. demonstrated that this phenomenon does not occur at significantly increased ion energy fluxes. Thus, it may be a process that dominates at more moderate conditions and is less important at high ion and radical densities.

5 Conclusion & Outlook

The focus of this work was to mass spectrometrically characterize metal hydrides (primarily stannane, SnH_4), along with their chemical behavior in the gas phase and upon contact with diverse surfaces at the ultra-trace level. In addition, studies are being conducted to determine how other selected elements volatilize by hydride formation and thus cause contamination by subsequent decomposition reactions. For this purpose, the formation and decomposition mechanisms of various (metal) hydrides were studied, in particular stannane as well-known source of debris in EUVL. In the course of this research, many effects have been studied and new observations have been made. These have contributed to a more detailed understanding of the dynamics and mechanisms leading to debris.

A reference high-resolution 70 eV electron ionization mass spectrum of stannane, where the conditions upon ionization are precisely known, was recorded. For this purpose, stannane was synthesized. To the best of our knowledge, this is the only published high-resolution EI mass spectrum. With a second analytical technique, Fourier-transform (FT) infrared (IR) spectroscopy the chemical identity (i.e., SnH_4) of the synthesized product was confirmed along the absence of detectable contamination byproducts. The *reverse analysis of superimposed signal patterns* (RASP) analysis program has been developed because even the high resolution of the employed instruments is not sufficient for the complete identification of all species due to the small mass differences between the different signals per nominal mass. With RASP, it became possible to calculate the expected distribution of the signals of the individual species, which upon deviation minimized summation reproduces the experimentally derived signal pattern. The species distribution therefore provides important information about the processes of compound formation and decomposition.

Using mass spectrometry, it has been confirmed experimentally that both neutral and ionic tin hydrides are formed by interaction of elemental tin with hydrogen plasma species. Furthermore, the results provide further evidence that these species are volatile and are thermodynamically stable in the chemical systems studied. It was demonstrated that the native ionic species, depending on the i) selected plasma source, ii) ion transfer stage, and iii) mass spectrometer/ion source used, significantly different signal distributions are obtained for tin hydrides. These fragmentation patterns allow to drawing conclusions on

5 Conclusion & Outlook

ion transport properties from the origin of formation to the collision-free mass analyzer region. On the other hand, 70 eV EI mass spectra of neutral did not show any significant signal pattern variations as expected, since the probability of collision induced changes of the fragmentation distribution is minimal in this case. Comparison of the mass spectra obtained for the synthesized and plasma-generated tin species also suggests that SnH_4 is the precursor molecule, which is then ionized and fragmented by further processes in the plasma respectively the ion source. In addition to SnH_X^+ , several other tin hydride species were determined, such as the tin hydride dimers (Sn_2H_X^+), doubly charged tin hydrides (SnH_X^{2+}), and oxygenated tin hydrides (SnOH_X^+).

In addition to tin, other elements, i.e., lead (Pb), magnesium (Mg), copper (Cu), silicon (Si), tantalum (Ta) and nickel (Ni) were also studied with regard to their ability to form volatile hydrides. The ability to form volatile hydrides with sufficient stability to be detected was inconsistent. A systematic scheme of stability related to chemical properties of the elements could not be deduced due to the restricted number of elements investigated.

DFT calculations were performed to obtain additional information on the stability and the molecular geometry of various neutral, cationic and anionic metal hydride species. In some cases, different trends in the stabilities of the species considered were observed with the two basis sets employed. More in-depth work is certainly needed to rationalize the experimentally observed species. It was way beyond the scope of this work, which centers on experimental studies.

Furthermore, an initial significantly increased etch rate of tin by hydrogen plasma species was observed, which is directly related to the prior exposure of the tin surface to ambient air. It could not be conclusively determined, whether oxygen or water or both cause this effect, nor how it affects the etching process on the atomic level. Experimentally, it has been demonstrated that this effect must be due to heterogeneous surface processes, since adding oxygen to the gas phase does not lead to a corresponding effect. This supports the hypothesis that surface oxidation is a feasible route to increased etching rate. This phenomenon is not unique to tin but also occurs with other metals.

Experiments with quartz crystal microbalance (QCM) instruments allowed direct determination of the etch rate of tin-coated sensors in a hydrogen plasma. Since QCMs detect the mass changes directly, quantitative data are becoming available. The etching effects described in the mass spectrometry based analyses were reproduced in the QCM experiments. For simultaneous QCM/MS experiments, the tin removal from the QCM sensor occurred via tin hydride ion formations, as demonstrated with the mass spectrometrical results.

It has been repeatedly discussed in the individual thesis sections, that further work is required to advance the understanding of the processes and chemical reactions involved. The present work is only a scratch on the surface of the overarching subject, where the results of each new experiment lead to a multitude of new questions. Carefully voiced, future experiments should focus on investigating and elucidating the molecular level surface processes leading to the formation of metal hydrides and the parameters that affect these processes. Furthermore, the role oxygen within these surface processes is of great interest. Since metal oxide surfaces result in much higher etch rates with hydrogen plasma species, this may be an option for accelerating the cleaning of tin-contaminated surfaces. This requires in-depth knowledge of the reactions occurring between oxygen and the metal at the surface. Techniques as for example X-ray photoelectron spectroscopy could be used to elucidate surface processes that cause morphology to change. For example, surface oxidation or the reaction of plasma species with an oxidized surface could be monitored. It is emphasized that the experimental results presented here have only limited applicability to EUVL scanner processes. The conditions of the plasma, the surfaces, and the geometrical dimensions of the experiments are rarely comparable with those present in the EUVL instruments.

This work aids in paving the way for further investigations focused specifically on the design, optimization and characterization of mass spectrometric tools for hydrogen plasma systems. Such future investigations may aim to determine the relevant ionic and neutral species and to adapt laboratory results to real plasma systems. Such a real-time monitoring can provide entirely new information about the temporal changes in the systems and allow to get closer to the processes taking place than was previously possible. However, here again it has to be said:

The journey has just begun.

References

- [1] G. E. Moore, “Cramming more components onto integrated circuits”, *Proceedings of the IEEE* **86**, 82–85 (1998) DOI: 10.1109/JPROC.1998.658762.
- [2] T. Hoeren, “The Semiconductor Chip Industry The History, Present and Future of Its IP Law Framework”, *IIC International Review of Intellectual Property and Competition Law* **47**, 763–796 (2016) DOI: 10.1007/s40319-016-0511-8.
- [3] H. J. Levinson, *Principles of lithography: Third edition*, 3rd ed. (SPIE Press, 2011), pp. 1–505, ISBN: 9780819483256, DOI: 10.1117/3.865363.
- [4] E. Abbe, “Beiträge zur Theorie des Mikroskops und der mikroskopischen Wahrnehmung”, *Archiv für Mikroskopische Anatomie* **9**, 413–468 (1873) DOI: 10.1007/BF02956173.
- [5] R. A. Burdt, Y. Tao, M. S. Tillack, S. Yuspeh, N. M. Shaikh, E. Flaxer, and F. Najmabadi, “Laser wavelength effects on the charge state resolved ion energy distributions from laser-produced Sn plasma”, *Journal of Applied Physics* **107**, 043303 (2010) DOI: 10.1063/1.3309413.
- [6] F. Torretti, R. Schupp, D. Kurilovich, A. Bayerle, J. Scheers, W. Ubachs, R. Hoekstra, and O. O. Versolato, “Short-wavelength out-of-band EUV emission from Sn laser-produced plasma”, *Journal of Physics B: Atomic, Molecular and Optical Physics* **51**, DOI: 10.1088/1361-6455/aaa593 (2018) DOI: 10.1088/1361-6455/aaa593.
- [7] J. R. Hoffman, A. N. Bykanov, O. V. Khodykin, A. I. Ershov, N. R. Bowering, I. V. Fomenkov, W. N. Partlo, and D. W. Myers, “LPP EUV conversion efficiency optimization”, in *Emerging lithographic technologies ix*, Vol. 5751, edited by R. S. Mackay (2005), p. 892, DOI: 10.1117/12.601048.
- [8] T. W. Barbee, Jr., “Multilayers For X-Ray Optics”, *Optical Engineering* **25**, 898–915 (1986) DOI: 10.1117/12.7973929.
- [9] E. Spiller, “Low-loss reflection coatings using absorbing materials”, *Applied Physics Letters* **20**, 365–367 (1972) DOI: 10.1063/1.1654189.

- [10] C. Wagner and N. Harned, “EUV lithography: Lithography gets extreme”, *Nature Photonics* **4**, 24–26 (2010) DOI: 10.1038/nphoton.2009.251.
- [11] R. Allen Burdt, “UC San Diego UC San Diego Electronic Theses and Dissertations Title Ion emission and expansion in laser-produced tin plasma”, Dissertation (University of California, San Diego, 2011), <https://escholarship.org/uc/item/0vb83923>.
- [12] Y. M. Chung, E. M. Lee, T. Masuoka, and J. A. Samson, “Dissociative photoionization of H₂ from 18 to 124 eV”, *The Journal of Chemical Physics* **99**, 885–889 (1993) DOI: 10.1063/1.465352.
- [13] I. Langmuir, “Oscillations in Ionized Gases”, *Proceedings of the National Academy of Sciences* **14**, 627–637 (1928) DOI: 10.1073/pnas.14.8.627.
- [14] U. Stroth, *Plasmaphysik* (Springer Berlin Heidelberg, Berlin, Heidelberg, 2018), ISBN: 978-3-662-55235-3, DOI: 10.1007/978-3-662-55236-0.
- [15] C. Chiuderi and M. Velli, *Basics of Plasma Astrophysics*, UNITEXT for Physics (Springer Milan, Milano, 2015), p. 279, ISBN: 978-88-470-5279-6, DOI: 10.1007/978-88-470-5280-2.
- [16] W. H. Kegel, *Plasmaphysik: Eine Einführung* (Springer Berlin Heidelberg, 2013), ISBN: 9783642587719, <https://books.google.de/books?id=0tIkBgAAQBAJ>.
- [17] B. M. Smirnov, *Properties of Gas Discharge Plasma*, Vol. 84, Springer Series on Atomic, Optical, and Plasma Physics (Springer International Publishing, Cham, 2015), pp. 13–29, ISBN: 978-3-319-11064-6, DOI: 10.1007/978-3-319-11065-3_2.
- [18] I. Langmuir, “Positive ion currents from the positive column of mercury arcs”, *Science* **58**, 290–291 (1923) DOI: 10.1126/science.58.1502.290.
- [19] M. A. Lieberman, *Principles of Plasma Discharges and Processing*, Vol. 1 (Wiley, 2005), ISBN: 9780471724254, DOI: 10.1002/0471724254.
- [20] H. Conrads and M. Schmidt, “Plasma generation and plasma sources”, *Plasma Sources Science and Technology* **9**, 441–454 (2000) DOI: 10.1088/0963-0252/9/4/301.
- [21] T. W. Johnston and J. M. Dawson, “Correct values for high-frequency power absorption by inverse bremsstrahlung in plasmas”, *Physics of Fluids* **16**, 722 (1973) DOI: 10.1063/1.1694419.
- [22] G. V. Ostrovskaya and A. N. Zadel, “Laser spark in gases”, *Soviet Physics - Uspekhi* **16**, 834–855 (1974) DOI: 10.1070/PU1974v016n06ABEH004094.

References

- [23] David R. Lide, “CRC Handbook of Chemistry and Physics, 87th ed
Editor-in-Chief: David R. Lide (National Institute of Standards and Technology).
CRC Press/Taylor and Francis Group: Boca Raton, FL. 2006. 2608 pp. \$139.95.
ISBN 0-8493-0487-3.”, *Journal of the American Chemical Society* **129**, edited by
D. R. Lide, 724–724 (2007) DOI: 10.1021/ja069813z.
- [24] V. M. Crijns, “Hydrogen atom based tin cleaning”, Masterthesis (Eindhoven
University of Technology, 2014).
- [25] K. Tamaru, “The thermal decomposition of tin hydride”, *Journal of Physical
Chemistry* **60**, 610–612 (1956) DOI: 10.1021/j150539a024.
- [26] I. W. Levin and H. Ziffer, “Vibrational spectra and potential function for SnH₄
and SnD₄”, *The Journal of Chemical Physics* **43**, 4023–4029 (1965) DOI:
10.1063/1.1696636.
- [27] IUPAC, *NIST Chemistry WebBook, NIST Standard Reference Database Number 69*,
2007, <http://srdata.nist.gov/solubility/>.
- [28] D. J. Aaserud and F. W. Lampe, “Vacuum-ultraviolet photodecomposition of
stannane”, *Journal of Physical Chemistry* **100**, 10215–10222 (1996) DOI:
10.1021/jp960740n.
- [29] S. Dahl, A. Logadottir, R. C. Egeberg, J. H. Larsen, I. Chorkendorff, E. Törnqvist,
and J. K. Nørskov, “Role of steps in N₂ activation on Ru(0001)”, *Physical Review
Letters* **83**, 1814–1817 (1999) DOI: 10.1103/PhysRevLett.83.1814.
- [30] C. Egawa, T. Nishida, S. Naito, and K. Tamaru, “Ammonia decomposition on (1 1
10) and (0 0 1) surfaces of ruthenium”, *Journal of the Chemical Society, Faraday
Transactions 1: Physical Chemistry in Condensed Phases* **80**, 1595–1604 (1984)
DOI: 10.1039/F19848001595.
- [31] M. Mittermüller and D. A. Volmer, “Micro- and nanostructures and their
application in gas chromatography”, *Analyst* **137**, 3195–3201 (2012) DOI:
10.1039/c2an35184f.
- [32] S. Bhattacharjee, U. V. Waghmare, and S. C. Lee, “An improved d-band model of
the catalytic activity of magnetic transition metal surfaces”, *Scientific Reports* **6**,
35916 (2016) DOI: 10.1038/srep35916.
- [33] Á. Logadóttir and J. K. Nørskov, “Ammonia synthesis over a Ru(0001) surface
studied by density functional calculations”, *Journal of Catalysis* **220**, 273–279
(2003) DOI: 10.1016/S0021-9517(03)00156-8.

- [34] T. Singh, M. S. Valipa, T. J. Mountziaris, and D. Maroudas, “Mechanisms and energetics of hydride dissociation reactions on surfaces of plasma-deposited silicon thin films”, *Journal of Chemical Physics* **127**, DOI: 10.1063/1.2781393 (2007) DOI: 10.1063/1.2781393.
- [35] M. Volmer and Weber, “Keimbildung in übersättigten Gebilden”, *Zeitschrift für Physikalische Chemie* **119U**, 277–301 (1926) DOI: 10.1515/zpch-1926-11927.
- [36] I. N. Stranski and L. Krastanow, “Zur Theorie der orientierten Ausscheidung von Ionenkristallen aufeinander”, *Monatshefte für Chemie* **71**, 351–364 (1937) DOI: 10.1007/BF01798103.
- [37] F. C. F. van der Merwe and J. H., “Dislocations. I. Static Theory”, *Proceedings of the Royal Society of London. Series A, Mathematical and Physical Sciences* **198**, 205–216 (1949).
- [38] J. H. Van Der Merwe, “Misfitting monolayers and oriented overgrowth”, *Discussions of the Faraday Society* **5**, 201–214 (1949) DOI: 10.1039/DF9490500201.
- [39] F. C. Frank and J. H. van der Merwe, “One-dimensional dislocations - III. Influence of the second harmonic term in the potential representation, on the properties of the model”, *Proceedings of the Royal Society of London. Series A. Mathematical and Physical Sciences* **200**, 125–134 (1949) DOI: 10.1098/rspa.1949.0163.
- [40] D. Ugur, A. J. Storm, R. Verberk, J. C. Brouwer, and W. G. Sloof, “Decomposition of SnH₄ molecules on metal and metal-oxide surfaces”, *Applied Surface Science* **288**, 673–676 (2014) DOI: 10.1016/j.apsusc.2013.10.096.
- [41] S. M. Zyryanov, A. S. Kovalev, D. V. Lopaev, E. M. Malykhin, A. T. Rakhimov, T. V. Rakhimova, K. N. Koshelev, and V. M. Krivtsun, “Loss of hydrogen atoms in H₂ plasma on the surfaces of materials used in EUV lithography”, *Plasma Physics Reports* **37**, 881–889 (2011) DOI: 10.1134/S1063780X11090157.
- [42] N. Faradzhev and V. Sidorkin, “Hydrogen mediated transport of Sn to Ru film surface”, *Journal of Vacuum Science & Technology A: Vacuum, Surfaces, and Films* **27**, 306–314 (2009) DOI: 10.1116/1.3081968.
- [43] O. V. Braginsky, A. S. Kovalev, D. V. Lopaev, E. M. Malykhin, T. V. Rakhimova, A. T. Rakhimov, A. N. Vasilieva, S. M. Zyryanov, K. N. Koshelev, V. M. Krivtsun, M. van Kaampen, and D. Glushkov, “Removal of amorphous C and Sn on Mo:Si multilayer mirror surface in Hydrogen plasma and afterglow”, *Journal of Applied Physics* **111**, 093304 (2012) DOI: 10.1063/1.4709408.

References

- [44] D. Ugur, A. J. Storm, R. Verberk, J. C. Brouwer, and W. G. Sloof, “Generation and decomposition of volatile tin hydrides monitored by in situ quartz crystal microbalances”, *Chemical Physics Letters* **552**, 122–125 (2012) DOI: 10.1016/j.cplett.2012.09.054.
- [45] D. T. Elg, G. A. Panici, J. A. Peck, S. N. Srivastava, and D. N. Ruzic, “ Modeling and measurement of hydrogen radical densities of in situ plasma-based Sn cleaning source ”, *Journal of Micro/Nanolithography, MEMS, and MOEMS* **16**, 023501 (2017) DOI: 10.1117/1.jmm.16.2.023501.
- [46] D. T. Elg, G. A. Panici, S. Liu, G. Girolami, S. N. Srivastava, and D. N. Ruzic, “Removal of Tin from Extreme Ultraviolet Collector Optics by In-Situ Hydrogen Plasma Etching”, *Plasma Chemistry and Plasma Processing* **38**, 223–245 (2018) DOI: 10.1007/s11090-017-9852-4.
- [47] D. T. Elg, “Removal of tin from extreme ultraviolet collector optics by an in-situ hydrogen plasma”, PhD thesis (University of Illinois, 2016).
- [48] K. Jacobi, “Nitrogen on ruthenium single-crystal surfaces”, *Physica Status Solidi (A) Applied Research* **177**, 37–51 (2000) DOI: 10.1002/(SICI)1521-396X(200001)177:1<37::AID-PSSA37>3.0.CO;2-Y.
- [49] B. Siegel, “Hydride formation by atomic hydrogen reactions”, *Journal of Chemical Education* **38**, 496–501 (1961) DOI: 10.1021/ed038p496.
- [50] C. Egawa, S. Naito, and K. Tamaru, “Adsorption and decomposition of NO and NH₃ on Ru(001) and Ru(1,1,10) surfaces”, *Surface Science* **138**, 279–291 (1984) DOI: 10.1016/0039-6028(84)90248-6.
- [51] H. Umemoto, K. Ohara, D. Morita, T. Morimoto, M. Yamawaki, A. Masuda, and H. Matsumura, “Radical Species Formed by the Catalytic Decomposition of NH₃ on Heated W Surfaces”, *Japanese Journal of Applied Physics, Part 1: Regular Papers and Short Notes and Review Papers* **42**, 5315–5321 (2003) DOI: 10.1143/jjap.42.5315.
- [52] S. Grantham, C. Tarrío, S. B. Hill, L. J. Richter, T. B. Lucatorto, J. van Dijk, C. Kaya, N. Harned, R. Hoefnagels, M. Silova, and J. Steinhoff, “The NIST EUV facility for advanced photoresist qualification using the witness-sample test”, in *Extreme ultraviolet (euv) lithography ii*, Vol. 7969, edited by B. M. La Fontaine and P. P. Naulleau (2011), 79690K, ISBN: 9780819485281, DOI: 10.1117/12.879519.

- [53] H. S. Tao, U. Diebold, N. D. Shinn, and T. E. Madey, “Surface chemistry of PH₃, PF₃ and PCl₃ on Ru(0001)”, *Surface Science* **312**, 323–344 (1994) DOI: 10.1016/0039-6028(94)90725-0.
- [54] E. Pietsch and H. Lehl, “Bildung von Metallhydriden durch atomaren Wasserstoff”, *Kolloid-Zeitschrift* **68**, 226–230 (1934) DOI: 10.1007/bf01451388.
- [55] D. Heskett, A. Baddorf, and E. W. Plummer, “Nitrogen-induced reconstruction of Cu(110): Formation of a surface nitride”, *Surface Science* **195**, 94–102 (1988) DOI: 10.1016/0039-6028(88)90782-0.
- [56] E. Wiberg, H. Goeltzer, and R. Bauer, “Synthese von Magnesiumhydrid aus den Elementen”, *Zeitschrift fur Naturforschung - Section B Journal of Chemical Sciences* **6**, 394–395 (1951) DOI: 10.1515/znb-1951-0714.
- [57] T. E. Madey, N. S. Faradzhev, B. V. Yakshinskiy, and N. V. Edwards, “Surface phenomena related to mirror degradation in extreme ultraviolet (EUV) lithography”, *Applied Surface Science* **253**, 1691–1708 (2006) DOI: 10.1016/j.apsusc.2006.04.065.
- [58] M. A. Henderson, C. L. Perkins, M. H. Engelhard, S. Thevuthasan, and C. H. Peden, “Redox properties of water on the oxidized and reduced surfaces of CeO₂(1 1 1)”, *Surface Science* **526**, 1–18 (2003) DOI: 10.1016/S0039-6028(02)02657-2.
- [59] P. A. Thiel and T. E. Madey, “The interaction of water with solid surfaces: Fundamental aspects”, *Surface Science Reports* **7**, 211–385 (1987) DOI: 10.1016/0167-5729(87)90001-X.
- [60] M. A. Henderson, “The interaction of water with solid surfaces: Fundamental aspects revisited”, *Surface Science Reports* **46**, 1–308 (2002) DOI: 10.1016/s0167-5729(01)00020-6.
- [61] M. M. Thiam, T. Kondo, N. Horimoto, H. S. Kato, and M. Kawai, “Initial growth of the water layer on (1 $\bar{1}$ 1)-oxygen-covered Ru(0001) in comparison with that on bare Ru(0001)”, *Journal of Physical Chemistry B* **109**, 16024–16029 (2005) DOI: 10.1021/jp052167q.
- [62] W. Proust, “On the Relation between the Specific Gravities of Bodies in their Gaseous State and the Weights of their Atoms”, *Annals of Philosophy* **6**, 321–330 (1815), <http://biodiversitylibrary.org/item/54028%7B%5C#%7Dpage/9/mode/1up>.

References

- [63] B. Gee, “From Protyle to Proton: William Prout and the Nature of Matter 1785-1985”, *Physics Bulletin* **36**, 505–506 (1985) DOI: 10.1088/0031-9112/36/12/025.
- [64] E. Goldstein, *Canalstrahlen* (Severus-Verlag, 2010), ISBN: 9783942382083, <https://books.google.de/books?id=oH4-va522yEC>.
- [65] J. J. Thomson, “Cathode rays”, *Philosophical Magazine* **90**, 25–29 (2010) DOI: 10.1080/14786431003659214.
- [66] A. J. Dempster, “Positive ray analysis of lithium and magnesium”, *Physical Review* **18**, 415–422 (1921) DOI: 10.1103/PhysRev.18.415.
- [67] F. Aston, “LXXIV. A positive ray spectrograph”, *The London, Edinburgh, and Dublin Philosophical Magazine and Journal of Science* **38**, 707–714 (1919) DOI: 10.1080/14786441208636004.
- [68] P. Lenard, “Ueber die lichtelektrische Wirkung”, *Annalen der Physik* **313**, 149–198, ISSN: 15213889 (1902) DOI: 10.1002/andp.19023130510.
- [69] T. D. Mark, “Fundamental aspects of electron impact ionization”, *International Journal of Mass Spectrometry and Ion Physics* **45**, 125–145 (1982) DOI: 10.1016/0020-7381(82)80103-4.
- [70] F. Guthrie, “XXXI. On a relation between heat and static electricity”, *The London, Edinburgh, and Dublin Philosophical Magazine and Journal of Science* **46**, 257–266 (1873) DOI: 10.1080/14786447308640935.
- [71] J. H. Gross, *Massenspektrometrie* (Springer Berlin Heidelberg, Berlin, Heidelberg, 2013), ISBN: 978-3-8274-2980-3, DOI: 10.1007/978-3-8274-2981-0.
- [72] C. Brooks, “Some aspects of mass spectrometry in research on steroids”, *Philosophical Transactions of the Royal Society of London. Series A, Mathematical and Physical Sciences* **293**, 53–67 (1979) DOI: 10.1098/rsta.1979.0079.
- [73] V. L. Tal’roze and A. K. Ljubimova, “Secondary processes in the ion source of a mass spectrometer (presented by academician N. N. Semenov 27 VIII 1952) - Reprinted from report of the soviet academy of sciences, Volume LXXXVI, -N5 (1952)”, *Journal of Mass Spectrometry* **33**, 502–504 (1998) DOI: 10.1002/(sici)1096-9888(199806)33:6<502::aid-jms685>3.0.co;2-%23.
- [74] M. S. Munson and F. H. Field, “Chemical Ionization Mass Spectrometry. I. General Introduction”, *Journal of the American Chemical Society* **88**, 2621–2630 (1966) DOI: 10.1021/ja00964a001.

- [75] T. W. Burgoyne and G. M. Hieftje, “An introduction to ion optics for the mass spectrograph”, *Mass Spectrometry Reviews* **15**, 241–259 (1996) DOI: 10.1002/(SICI)1098-2787(1996)15:4<241::AID-MAS2>3.0.CO;2-I.
- [76] A. Klemm, “Zur Theorie der für alle Massen doppelfokussierenden Massenspektrographen”, *Zeitschrift für Naturforschung - Section A Journal of Physical Sciences* **1**, 137–141 (1946) DOI: 10.1515/zna-1946-0306.
- [77] J. De Laeter and M. D. Kurz, “Alfred Nier and the sector field mass spectrometer”, *Journal of Mass Spectrometry* **41**, 847–854 (2006) DOI: 10.1002/jms.1057.
- [78] H. Hintenberger and L. König, “Mass Spectrometers and Mass Spectrographs Corrected for Image Defects”, in *Advances in mass spectrometry* (Elsevier, 1959), pp. 16–35, DOI: 10.1016/b978-0-08-009210-2.50008-0.
- [79] H. Matsuda, “Double-focusing mass spectrometers of short path length”, *International Journal of Mass Spectrometry and Ion Processes* **93**, 315–321 (1989) DOI: 10.1016/0168-1176(89)80120-X.
- [80] M. M. Wolff and W. E. Stephens, “A pulsed mass spectrometer with time dispersion”, *Review of Scientific Instruments* **24**, 616–617 (1953) DOI: 10.1063/1.1770801.
- [81] G. Sauerbrey, “Verwendung von Schwingquarzen zur Wägung dünner Schichten und zur Mikrowägung”, *Zeitschrift für Physik* **155**, 206–222 (1959) DOI: 10.1007/BF01337937.
- [82] A. K. Srivastava and P. Sakthivel, “Quartz-crystal microbalance study for characterizing atomic oxygen in plasma ash tools”, *Journal of Vacuum Science & Technology A: Vacuum, Surfaces, and Films* **19**, 97–100 (2001) DOI: 10.1116/1.1335681.
- [83] F. E. Saalfeld and H. J. Svec, “The mass spectrum of stannane”, *Journal of Inorganic and Nuclear Chemistry* **18**, 98–102 (1961) DOI: 10.1016/0022-1902(61)80374-6.
- [84] J. R. De Laeter, J. K. Böhlke, P. De Bièvre, H. Hidaka, H. S. Peiser, K. J. Rosman, and P. D. Taylor, “Atomic weights of the elements: Review 2000 (IUPAC Technical Report)”, *Pure and Applied Chemistry* **75**, 683–800 (2003) DOI: 10.1351/pac200375060683.

References

- [85] A. D. Norman, J. R. Webster, and W. L. Jolly, “Silane, Stannane, Silane-d₄, Germane-d₄, and Stannane-d₄”, *Inorganic Synthesis*, University of California **XI**, 170–181 (1968), <https://escholarship.org/content/qt4wt7m4gm/qt4wt7m4gm.pdf>.
- [86] D. T. Elg, G. A. Panici, S. Liu, G. Girolami, S. N. Srivastava, and D. N. Ruzic, “Correction to: Removal of Tin from Extreme Ultraviolet Collector Optics by In-Situ Hydrogen Plasma Etching (Plasma Chemistry and Plasma Processing, (2018), 38, 1, (223-245), 10.1007/s11090-017-9852-4)”, *Plasma Chemistry and Plasma Processing* **38**, 917–918 (2018) DOI: 10.1007/s11090-018-9882-6.
- [87] H. Meissner, “Ein neuer Naehweis für Zinn”, *Zeitschrift für Analytische Chemie* **80**, 247–252 (1930) DOI: 10.1007/BF01358047.
- [88] N. Yamazoe, J. Fuchigami, M. Kishikawa, and T. Seiyama, “Interactions of tin oxide surface with O₂, H₂O AND H₂”, *Surface Science* **86**, 335–344 (1979) DOI: 10.1016/0039-6028(79)90411-4.
- [89] G. Van Rossum and F. L. Drake, *Python 3 Reference Manual*, Scotts Valley (CreateSpace, Scotts Valley, CA, 2009), ISBN: 1441412697.
- [90] C. R. Harris, K. J. Millman, S. J. van der Walt, R. Gommers, P. Virtanen, D. Cournapeau, E. Wieser, J. Taylor, S. Berg, N. J. Smith, R. Kern, M. Picus, S. Hoyer, M. H. van Kerkwijk, M. Brett, A. Haldane, J. F. del Río, M. Wiebe, P. Peterson, P. Gérard-Marchant, K. Sheppard, T. Reddy, W. Weckesser, H. Abbasi, C. Gohlke, and T. E. Oliphant, “Array programming with NumPy”, *Nature* **585**, 357–362 (2020) DOI: 10.1038/s41586-020-2649-2.
- [91] J. Reback, jbrockmendel, W. McKinney, J. V. den Bossche, T. Augspurger, M. Roeschke, S. Hawkins, P. Cloud, gyoung, Sinhrks, P. Hoefler, A. Klein, T. Petersen, J. Tratner, C. She, W. Ayd, S. Naveh, J. Darbyshire, M. Garcia, R. Shadrach, J. Schendel, A. Hayden, D. Saxton, M. E. Gorelli, F. Li, M. Zeitlin, V. Jancauskas, A. McMaster, T. Wörtwein, and P. Battiston, *Pandas-dev/pandas: pandas 1.4.2*, version v1.4.2, 2022, DOI: 10.5281/zenodo.6408044.
- [92] P. Virtanen, R. Gommers, T. E. Oliphant, M. Haberland, T. Reddy, D. Cournapeau, E. Burovski, P. Peterson, W. Weckesser, J. Bright, S. J. van der Walt, M. Brett, J. Wilson, K. J. Millman, N. Mayorov, A. R. Nelson, E. Jones, R. Kern, E. Larson, C. J. Carey, Polat, Y. Feng, E. W. Moore, J. VanderPlas, D. Laxalde, J. Perktold, R. Cimrman, I. Henriksen, E. A. Quintero, C. R. Harris, A. M. Archibald, A. H. Ribeiro, F. Pedregosa, P. van Mulbregt, A. Vijaykumar, A. P. Bardelli, A. Rothberg, A. Hilboll, A. Kloeckner, A. Scopatz,

- A. Lee, A. Rokem, C. N. Woods, C. Fulton, C. Masson, C. Häggström, C. Fitzgerald, D. A. Nicholson, D. R. Hagen, D. V. Pasechnik, E. Olivetti, E. Martin, E. Wieser, F. Silva, F. Lenders, F. Wilhelm, G. Young, G. A. Price, G. L. Ingold, G. E. Allen, G. R. Lee, H. Audren, I. Probst, J. P. Dietrich, J. Silterra, J. T. Webber, J. Slavi, J. Nothman, J. Buchner, J. Kulick, J. L. Schönberger, J. V. de Miranda Cardoso, J. Reimer, J. Harrington, J. L. C. Rodríguez, J. Nunez-Iglesias, J. Kuczynski, K. Tritz, M. Thoma, M. Newville, M. Kümmerer, M. Bolingbroke, M. Tartre, M. Pak, N. J. Smith, N. Nowaczyk, N. Shebanov, O. Pavlyk, P. A. Brodtkorb, P. Lee, R. T. McGibbon, R. Feldbauer, S. Lewis, S. Tygier, S. Sievert, S. Vigna, S. Peterson, S. More, T. Pudlik, T. Oshima, T. J. Pingel, T. P. Robitaille, T. Spura, T. R. Jones, T. Cera, T. Leslie, T. Zito, T. Krauss, U. Upadhyay, Y. O. Halchenko, and Y. Vázquez-Baeza, “SciPy 1.0: fundamental algorithms for scientific computing in Python”, *Nature Methods* **17**, 261–272 (2020) DOI: 10.1038/s41592-019-0686-2.
- [93] J. D. Hunter, “Matplotlib: A 2D graphics environment”, *Computing in Science and Engineering* **9**, 90–95 (2007) DOI: 10.1109/MCSE.2007.55.
- [94] C. Gohlke, “Molmass”, GitHub repository; <https://github.com/cgohlke/molmass> (2021), <https://github.com/cgohlke/molmass>.
- [95] J. A. Nelder and R. Mead, “Errata”, *The Computer Journal* **8**, 27–27 (1965) DOI: 10.1093/comjnl/8.1.27.
- [96] A. S. Moorthy and A. J. Kearsley, “Pattern Similarity Measures Applied to Mass Spectra”, in *Sema simai springer series*, Vol. 5 (Springer, Cham, 2021), pp. 43–53, ISBN: 978-3-030-61844-5, DOI: 10.1007/978-3-030-61844-5_4.
- [97] M. J. Frisch, G. W. Trucks, H. B. Schlegel, G. E. Scuseria, M. A. Robb, J. R. Cheeseman, G. Scalmani, V. Barone, G. A. Petersson, H. Nakatsuji, X. Li, M. Caricato, A. V. Marenich, J. Bloino, B. G. Janesko, R. Gomperts, B. Mennucci, H. P. Hratchian, J. V. Ortiz, A. F. Izmaylov, J. L. Sonnenberg, D. Williams-Young, F. Ding, F. Lipparini, F. Egidi, J. Goings, B. Peng, A. Petrone, T. Henderson, D. Ranasinghe, V. G. Zakrzewski, J. Gao, N. Rega, G. Zheng, W. Liang, M. Hada, M. Ehara, K. Toyota, R. Fukuda, J. Hasegawa, M. Ishida, T. Nakajima, Y. Honda, O. Kitao, H. Nakai, T. Vreven, K. Throssell, J. A. Montgomery Jr., J. E. Peralta, F. Ogliaro, M. J. Bearpark, J. J. Heyd, E. N. Brothers, K. N. Kudin, V. N. Staroverov, T. A. Keith, R. Kobayashi, J. Normand, K. Raghavachari, A. P. Rendell, J. C. Burant, S. S. Iyengar, J. Tomasi, M. Cossi, J. M. Millam,

References

- M. Klene, C. Adamo, R. Cammi, J. W. Ochterski, R. L. Martin, K. Morokuma, O. Farkas, J. B. Foresman, and D. J. Fox, *Gaussian 16*, Gaussian Inc. Wallingford (CT), 2019.
- [98] D. Roy, K. Todd A., and M. John M., “GaussView, Version 6.1”, Semichem Inc. **1** (2016).
- [99] A. D. Becke, “Density functional thermochemistry. I. The effect of the exchange only gradient correction”, *Journal of Chemical Physics* **96**, 2155–2160 (1992) DOI: 10.1063/1.462066.
- [100] C. Lee, W. Yang, and R. G. Parr, “Development of the Colle-Salvetti correlation-energy formula into a functional of the electron density”, *Physical Review B* **37**, DOI: 10.1103/PhysRevB.37.785 (1988) DOI: 10.1103/PhysRevB.37.785.
- [101] C. J. Cramer and D. G. Truhlar, “Density functional theory for transition metals and transition metal chemistry”, *Physical Chemistry Chemical Physics* **11**, 10757–10816 (2009) DOI: 10.1039/b907148b.
- [102] J. S. Binkley, J. A. Pople, and W. J. Hehre, “Self-consistent molecular orbital methods. 21. Small split-valence basis sets for first-row elements”, *Journal of the American Chemical Society* **102**, 939–947 (1980) DOI: 10.1021/ja00523a008.
- [103] F. Weigend and R. Ahlrichs, “Balanced basis sets of split valence, triple zeta valence and quadruple zeta valence quality for H to Rn: Design and assessment of accuracy”, *Physical Chemistry Chemical Physics* **7**, 3297–3305 (2005) DOI: 10.1039/b508541a.
- [104] F. E. Saalfeld, “The mass spectra of some volatile hydrides”, PhD thesis (Iowa State University, Digital Repository, Ames, 1984), DOI: 10.31274/rtd-180813-3776.
- [105] F. E. Saalfeld and H. J. Svec, “Correction. The Mass Spectra of Volatile Hydrides. II. Some Higher Hydrides of the Group IVB and VB Elements”, *Inorganic Chemistry* **3**, 1807 (1964) DOI: 10.1021/ic50022a601.
- [106] F. Wu, G. Levitin, and D. W. Hess, “Temperature Effects and Optical Emission Spectroscopy Studies of Hydrogen-Based Plasma Etching of Copper”, *Journal of The Electrochemical Society* **159**, H121–H124 (2011) DOI: 10.1149/2.015202jes.

- [107] M. E. Ruiz, J. García-Prieto, E. Poulain, G. A. Ozin, R. A. Poirier, S. M. Matta, I. G. Czismadia, C. Gracie, and O. Novaro, “Theoretical study on the CuH + H Cu + H₂ reaction pathway”, *Journal of Physical Chemistry* **90**, 279–282 (1986) DOI: 10.1021/j100274a015.
- [108] R. Burtovyy, E. Utzig, and M. Tkacz, “Studies of the thermal decomposition of copper hydride”, *Thermochimica Acta* **363**, 157–163 (2000) DOI: 10.1016/S0040-6031(00)00594-3.
- [109] N. P. Fitzsimons, W. Jones, and P. J. Herley, “Studies of copper hydride. Part 1. - Synthesis and solid-state stability”, *Journal of the Chemical Society, Faraday Transactions* **91**, 713–718 (1995) DOI: 10.1039/FT9959100713.
- [110] R. P. Eischens, W. A. Pliskin, and M. J. Low, “The infrared spectrum of hydrogen chemisorbed on zinc oxide”, *Journal of Catalysis* **1**, 180–191 (1962) DOI: 10.1016/0021-9517(62)90022-2.
- [111] R. Kirchheim and A. Pundt, *Hydrogen in Metals*, Fifth Edit, Vol. 1 (Elsevier B.V., 2014), ISBN: 9780444537713, DOI: 10.1016/B978-0-444-53770-6.00025-3.
- [112] D. Depla, S. Mahieu, and J. Greene, “Chapter 5 - sputter deposition processes”, in *Handbook of deposition technologies for films and coatings (third edition)*, edited by P. M. Martin, Third Edition (William Andrew Publishing, Boston, 2010), pp. 253–296, ISBN: 978-0-8155-2031-3, DOI: 10.1016/B978-0-8155-2031-3.00005-3.
- [113] G. Dearnaley, “Ion implantation”, *Nature* **256**, 701–705 (1975) DOI: 10.1038/256701a0.
- [114] S. Aisenberg and R. W. Chabot, “Physics of Ion Plating and Ion Beam Deposition”, *Journal of Vacuum Science and Technology* **10**, 104–107 (1973) DOI: 10.1116/1.1317915.